공학박사학위논문

도시열효율 최대화를 위한 불꽃점화엔진의 사이클내 속도형상 최적화 및 사이클 정량적 해석

Spark–Ignition Engine Speed Profile Optimization for Maximizing the Net Indicated Efficiency and Quantitative Analysis of the Optimal Speed Profile

2020 년 2 월

서울대학교 대학원

기계항공공학부

송 정 우

도시열효율 최대화를 위한 불꽃점화엔진의 사이클 내 속도형상 최적화 및 사이클 정량적 해석

Spark-Ignition Engine Speed Profile Optimization for Maximizing the Net Indicated Efficiency and Quantitative Analysis of the Optimal Speed Profile

지도교수 송 한 호

이 논문을 공학박사 학위논문으로 제출함

2019 년 10 월

서울대학교 대학원
기계항공공학부
송 정 우

송정우의 공학박사 학위논문을 인준함

2019 년 12 월

위 원 장 : 민 경 덕

부위원장 : 송 한 호

위 원 : 도 형 록

위 원 : 하 경 표

위 원 : 김 남 욱

Abstract

Spark–Ignition Engine Speed Profile Optimization for Maximizing the Net Indicated Efficiency and Quantitative Analysis of the Optimal Speed Profile

Jeongwoo Song

Department of Mechanical Engineering

The Graduate School

Seoul National University

Many studies are being conducted to satisfy the vehicle fuel economy and greenhouse gas standards, which are strengthened to reduce carbon dioxide emissions. Hydrocarbon–based fuels are expected to be used in the transport sector in the future. It is essential to increase the internal combustion engine–based powertrain efficiency to meet the standards. Among the various internal combustion engine–based powertrains, the series hybrid electric vehicle has an advantage in fuel economy. In this study, the possibility of increasing the thermodynamic efficiency by modulating the speed profile in a single cycle in a series hybrid electric vehicle powertrain structure is discussed using simulation.

Since the optimization was performed numerically, a quasi–dimensional spark–ignition engine model was used that has advantages in computation time. The burning rate was calculated using the turbulent flame model, and the flow–based heat transfer model in the cylinder was used to reflect the effect of the speed change. The in–cylinder flow characteristics were calculated using the quasi–dimensional turbulence model. The optimization problem was solved using the developed model. The discretization of the trajectory optimization problem into a parameter optimization problem can be used to obtain an optimal speed profile that maximizes efficiency.

Three performance parameters were used for quantitatively analyzing the cycle. The effective expansion ratio was defined to compare the combustion phases. The burning rate weighted average volume was calculated during the combustion duration. The effective expansion ratio was defined as the ratio between the cylinder volume at the exhaust valve opening and average cylinder volume during the combustion process. The larger the effective expansion ratio means that the combustion occurs near the top dead center, and the higher the chemical energy fuel converted to the pressure–volume work potential. In order to compare heat transfer, the amount of heat transfer from the intake valve opening to the exhaust valve closing was compared. Heat transfer in the gas exchange process is not included because it does not affect pressure–volume work that can be obtained from the engine. Finally, pressure–volume work that can be obtained from the gas exchange process was and compared.

The optimal speed profile shows that the efficiency of the spark–ignition engine can be improved by 5% p compared to the same average speed operation and 1% p compared to the best efficiency of conventional operating. As a result of the quantitative analysis of the cycle, the efficiency can be increased by improving the combustion phase compared with the conventional operation. When operating at an optimal speed profile, combustion

phasing is improved to a level of combustion phasing at the knock–free operating condition.

The effect of speed profile modulation on the recent technologies adopted spark–ignition engine was examined. Speed profile optimization was performed when the compression ratio was increased, the air–fuel ratio was increased, and under boosting conditions to increase the engine load. In the conventional operation, the efficiency is decreased by knocking even if the compression ratio is increased, but the efficiency is increased by effectively reducing the knocking by modulating the intracycle speed profile. The model used in this study confirmed that the compression ratio could increase the efficiency from 10.5 to 13.5 without efficiency deterioration. In the engine operating conditions with increased air–fuel ratio, the laminar flame speed was reduced, resulting in insufficient efficiency improvement in conventional engine operation. By enhancing the turbulence intensity through the speed profile modulation, an additional efficiency increase of about 1.5% p can be obtained at the equivalent ratio of 0.7. In boosting operating conditions, the decreased ignition delayed increases knocking due to elevated pressure, thereby reducing efficiency. It was also shown in optimal speed profile operation, but the efficiency of the boosting condition at 1.6 atm shows the efficiency of conventional operation at 1.0 atm.

The optimal speed profile that maximizes the efficiency of the spark–ignition engine is obtained. How the speed profile of each interval affects performance parameters was analyzed. Based on this, when it is impossible to modulate the speed profile of all the intervals, the result can be used to predict which speed profile should be changed to improve the desired performance parameter.

Keywords: Spark–ignition engine, Quasi–dimensional model, Speed profile modulation, Trajectory optimization, Efficiency analysis

Student Number: 2014–30343

Table of Content

List of Figures

List of Tables

Nomenclature

a	Crankshaft radius (m)
A_c	Curtain area (m^2)
A_e	Flame front area (m^2)
B	Cylinder bore (m)
C_D	Discharge coefficient (–)
c_p	Specific heat capacity at constant pressure ($J\ kg^{-1}\ K^{-1}$)
c_v	Specific heat capacity at constant volume ($J\ kg^{-1}\ K^{-1}$)
C_{RDT}	RDT coefficient (–)
C_{shear}	Shear rate coefficient (–)
C_ϵ	Dissipation rate coefficient (–)
C_k	Turbulent kinetic energy coefficient (–)
C_K	Mean kinetic energy coefficient (–)
D	Dissipation rate (W)
ER_{EFF}	Effective expansion ratio (–)
HL	Heat loss (–)
h	Mass specific enthalpy ($J\ kg^{-1}$)
h_{conv}	Convective heat transfer coefficient ($W\ m^{-2}\ K^{-1}$)
I	Incoming (W)
K	Mean kinetic energy ($J\ kg^{-1}$)
k	Turbulent kinetic energy ($J\ kg^{-1}$)

l	Connecting rod length (m)
LHV_{IVC}	Gas lower heating value at intake valve closing timing (J)
LW	Livengood–Wu integral value (–)
L_{mean}	Mean length scale (m)
V_{valve}	Gas speed through the valve (m s^{-1})
L_v	Valve lift (m)
m	Mass (kg)
N	Engine speed (rad/s)
N_u	The number of moles of unburned mixture (kmol)
N_b	The number of moles of burned mixture (kmol)
Ma	Mach number (–)
O	Outgoing (W)
P	Production (W)
p	Pressure (Pa)
$\dot{Q}$	Heat transfer rates (W)
R	Gas constant (J kg^{-1} K^{-1})
R_f	Flame radius (m)
Re	Reynolds number (–)
S_l	Laminar flame speed (m s^{-1})
T	Temperature (K)
u	Mass specific internal energy (J kg^{-1})

U	Mean gas speed (m s^{-1})
u'	Turbulent intensity (m s^{-1})
V	Volume (m^3)
V_p	Piston speed (m s^{-1})
$\dot{W}$	Pressure–volume work transfer rates (W)
X_b	Burned mass fraction (–)

Greek letters

γ	Specific heat ratio (–)
ϵ	Turbulent kinetic energy dissipation rate (W kg^{-1})
λ	Taylor microscale (m)
η	Efficiency (–)
η_p	Pumping work efficiency (–)
θ	Crank position (rad)
ν_t	Turbulent kinematic viscosity (m^2 s^{-1})
ρ	Density (kg m^3)
τ	Characteristic time scale (s)
τ_{ig}	Ignition delay (s)

Subscripts

b	Burned
$back$	Back flow
cyl	In-cylinder

in	Inflow
j	Species j
k	The number of simulation cycle
lb	Lower bound
o	Reservoir
out	Outflow
sp	Spark timing
u	Unburned
ub	Upper bound

Abbreviations

BDC	Bottom dead center
CAD	Crank angle degree
EVC/EVO	Exhaust valve closing/opening
IVC/IVO	Intake valve closing/opening
MKE	Mean kinetic energy
TDC	Top dead center
TKE	Turbulent kinetic energy

Chapter 1. Introduction

1.1. Background and motivation

1.1.1. Carbon dioxide emission of the vehicle

Efforts are being made to reduce energy use in response to climate change due to carbon dioxide emissions. Energy consumption in the transportation sector accounts for approximately 20 % of total energy usage and is expected to increase by 1% per year by 2040 [1].

In many countries, regulations on vehicle fuel economy and greenhouse gas emissions have been made and strengthened to reduce carbon dioxide emissions in the transportation sector. Especially, fuel economy or greenhouse gas standards of light–duty vehicles are summarized in this section.

In the U.S., both fuel economy and greenhouse gas emission are regulated according to the footprint of a vehicle [2]. Automakers satisfied the corporate average fuel economy and greenhouse gas emission, and the target of a standard is strengthened. In the EU, '95 g CO2/km by 2021 regulation' is enforced [3]. In Japan, the regulation limits the carbon dioxide emission of the corporate average according to the standard curb weight of a vehicle [4]. The target of this regulation will be strengthened by 2020. In China, cooperate average fuel consumption is regulated, and its target value will be decreased until 2020 [5]. In India, carbon dioxide emission of a vehicle is regulated [6], and in South Korea, fuel economy or carbon dioxide emission is regulated [7].

To satisfy those strengthened standards, automakers have begun developing and selling vehicles with new powertrains such as hybrid electric vehicles (HEV), electric vehicles (EV), and fuel cell electric vehicles (FCEV). EV uses an electric battery, and

FCEV uses electric battery and hydrogen as an energy carrier instead of conventional fossil fuels.

While automakers are trying to reduce carbon dioxide emissions using new energy carriers, according to the EIA report, the use of hydrocarbon–based fuels for the internal combustion engine (ICE) is still expected to increase in the transportation sector by 2040 [1]. Thus, it is difficult to meet future regulations on vehicle fuel economy without improving the ICE efficiency.

Well–to–wheel carbon dioxide emission of a vehicle is being studied for various powertrains [8, 9]. The results show that even in the same powertrain, well to wheel carbon dioxide emission varies depending on the region in which vehicle operates. The optimal powertrain from a well–to–wheel point of view varies from region to region [10].

Therefore, many studies are being conducted to improve the efficiency of ICE. The most representative method for improving the fuel economy of an ICE–based vehicle is a hybridization. Hybrid electric vehicles use an ICE and a motor at the same time. Because hydrocarbon–based fuels are the primary energy source of the transportation sector in the future, HEV is expected to be a suitable vehicle to reduce carbon dioxide emission of ICE–based vehicles. Therefore, in this study, the method to increase the efficiency of the ICE in an ICE–motor hybrid powertrain was discussed.

1.1.2. Energy analysis of SI engine

Since hydrocarbon–based fuels are expected to account for a significant portion of energy use in the transportation sector, the portion of ICE–based vehicles will be large in the future. Therefore, many studies to improve the efficiency of ICE will be conducted

continuously, and energy analysis is performed to analyze factors that decrease the efficiency of the ICE.

According to these studies, when converting energy using an ICE, heat loss from the hot gas to the cold engine body, exhaust loss caused by not converting all the gas energy to work during the expansion process after combustion, and friction loss. Due to these losses, the efficiency of the ICE is reduced.

First, when performing energy analysis, the lower heating value of the fuel injected into the ICE is used for system input. Since the ICE converts the chemical bond energy difference between reactants and products into sensible energy through the combustion process, the lower heating value of the fuel is used for system input. The lower heating value of the fuel entering the system is converted into pressure–volume work, heat loss from the gas to the cylinder wall, and sensible energy of the exhaust gas. Only pressure–volume work transfer is available in conventional ICE. Pressure–volume work is calculated from pressure and volume profiles. Convective heat transfer mainly occurs in an ICE. Total heat loss can be calculated from the energy balance equation, and the heat transfer rate can be calculated by modeling the convective heat transfer coefficient. Finally, the exhaust loss is calculated using the exhaust gas temperature or enthalpy. In the next section, we looked at the energy analysis results of the general SI engine to find out the inefficiency of the SI engine.

1.1.3. Loss in SI engine

As a result of energy analysis on the ICE, the chemical energy of the fuel is converted into various types of energy in addition to the mechanical work. If it is a loss that is transferred to other forms of energy besides being converted into mechanical work, losses are divided into heat loss, exhaust loss, and pumping loss.

Heat loss occurs due to the heat transfer from the hot gas to the cold engine body. Exhaust loss occurs due to all high burned gas energy that could not be converted into mechanical work. A fixed expansion ratio or limited work extraction method is a reason for the conversion limit. The pumping loss occurs in the low load or high engine speed operating condition in the SI engine [11]. Also, friction losses in pistons and bearings occur during the work transfer to vehicle driveshaft [12, 13].

These losses are influenced by the design and operating parameters of the ICE. Looking at how these losses are affected, first, the factors that affect heat loss are the in–cylinder flow dynamics, load or ambient temperature of an ICE, cylinder and piston geometry, and the in–cylinder gas composition, and wall temperature of the cylinder. Exhaust losses are related to the pre– and post–combustion state of the in–cylinder gas and expansion ratio of the ICE. Therefore, engine geometry, valve timing, in–cylinder gas composition, and combustion phasing affect the exhaust loss. Friction losses are affected by the engine speed, the viscosity, temperature of the lubricating oil, the engine load, and engine geometry

Each of the losses described above is affected by engine design or engine operating conditions. Engine designs that affect engine losses are a bore, stroke, combustion chamber geometry, and compression ratio. Engine operating conditions that affect engine losses are engine load, valve timing, exhaust gas recirculation ratio, and engine speed. For these parameters, each loss has a trade–off relationship, so ICE are designed and operate to optimize each loss.

In this study, the engine speed is focused on improving engine efficiency. As mentioned earlier, the shaft of the ICE is not directly connected to the driveshaft of the vehicle in a series hybrid electric vehicle. In this situation, the speed of the ICE in a single cycle can be controlled by an electric motor. Therefore, inefficiency factors that have a

trade–off relation by engine speed could be reduced using speed profile modulation in a single cycle.

1.1.4. New control variable

In order to satisfy the strengthened fuel economy or greenhouse gas emission standards, vehicles with new powertrains, such as hybrid electric vehicles and battery electric vehicles, have been developed and sold. As the new powertrain architecture becomes widespread, control variables that may not be available in the traditional ICE powertrain architecture emerge.

Among those control variables, it is possible to modulate the intracycle speed profile of the ICE by using the electric motor–generator connected to the ICE used for power generation in the powertrain architecture of the series HEV. Typical ICE use high inertia devices such as flywheels to minimize speed variation in a single cycle because the speed of an ICE directly affects the vehicle driveshaft speed. In a series hybrid vehicle, however, the vehicle driveshaft is powered by a battery–motor, and the ICE is used only for battery charging.

For this reason, additional acceleration or deceleration of the engine crankshaft could be achieved through the charging and discharging through the motor–generator connected to the ICE. Reducing the loss of the ICE and increasing the indicated efficiency can be achieved through the intracycle speed profile modulation of an ICE.

1.2. Previous studies

There have been studies to increase the efficiency of ICE by intracycle piston speed modulation. There are many simulation studies to optimize the intracycle speed profile, and engine speed variation effect on engine operation was investigated by experimental study. Since this study focuses on optimizing the intracycle speed profile based on the simulation using the SI engine model, it also includes a description of previous studies on SI engine modeling.

1.2.1. SI engine modeling

SI engine modeling method can be divided into using the three–dimensional model and quasi–dimensional model. A three–dimensional model is based on computational fluid dynamics (CFD). In–cylinder volume is divided into many cells, and in–cylinder thermodynamic or fluid dynamic states are calculated in three–dimensional model. The Reynolds averaged Navier–Stokes equation is mainly used to calculate the flow dynamic state of in–cylinder gas. Recently, the computational performance has been rapidly improved, and studies for modeling SI engines using three–dimensional models have been actively conducted [14-17].

However, despite advances in computational performance, it is difficult to use a three–dimensional model to solve the optimization problem in this study. The reason is that even if the simulation is performed using the RANS model, which requires the least computational cost among CFD models, it takes several hours to one day [18]. When performing optimization for one operating point, several thousand simulations are required. Therefore, it is difficult to solve the optimization problem of this study using a three–dimensional SI engine model.

As a result, SI engine modeling was performed using a quasi–dimensional model with an advantage in computational cost. There have been several previous studies on quasi–dimensional SI engine modeling.

Tabatabaie conducted a study of the heat transfer rate of an SI engine using hydrogen as a quasi–dimensional, multi–zone model [19]. The heat transfer rate was predicted using the in–cylinder thermodynamic state calculated by using the quasi–dimensional model and various heat transfer models. The heat flux and the pressure profile calculated from the developed model were compared with the experimental results, and a heat transfer model suitable for the engine using hydrogen was proposed.

Rakopoulos and Michos predicted the performance and emissions of biogas fueled SI engine using quasi–dimensional, multi–zone models [20]. NO emission was more accurately predicted by considering the chemical kinetics of in–cylinder mixture. The detailed chemical kinetics mechanism used in this previous study was suitable for a quasi–dimensional model because the mechanism consists of many species and reactions. The quasi–dimensional model can be confirmed to have significant accuracy when compared with the experimental results.

Bozza studied a downsized turbocharged SI engine using a quasi–dimensional, two–zone model [21]. The quasi–dimensional model was used to predict the burned mass fraction and the pressure profile of in–cylinder gas under various engine speed conditions. It was also shown that the engine performances such as air flow, mean effective pressure (MEP), shaft power, and brake specific fuel consumption (BSFC) can be accurately predicted by using the developed quasi–dimensional model among the various boosting pressure level.

When developing a quasi–dimensional model, several models are used to simulate the combustion process and heat transfer of the SI engine. When modeling the combustion process of the SI engine, the commonly used method is to use the Wiebe function. The Wiebe function is suitable for use in quasi–dimensional models because it can simulate combustion rates using several parameters. These parameters can be obtained through experiments or the correlations presented in many previous studies [22].

The turbulent flame model is used for calculating the burning rate under the engine operating conditions where the Wiebe function is difficult to apply or considering the in–cylinder flow characteristics. Under typical SI engine operating conditions, flame propagation is in the reaction sheet flame region. Burning rate can be modeled using the in–cylinder turbulence intensity to model the flame in the region. In order to use the turbulent flame model, the in–cylinder flow dynamics must be modeled [23, 24].

Woschni model is mainly used to predict heat transfer. The Woschni model calculates the heat transfer rate by calculating the convective heat transfer coefficient using the mean piston speed of the engine, in–cylinder temperature, and pressure. Many studies use the Woschni model to calculate the total heat transfer rate and the instantaneous heat flux [25, 26].

The Woschni model is a model fitted to the existing engine experimental data, so it is difficult to accurately predict the heat transfer rate as the engine design changes. Some studies have developed a flow–based heat transfer model. The in–cylinder flow dynamics model is needed to use the flow–based heat transfer model [27]. If the flow dynamics model is included in the SI engine model, the number of parameters required by the heat transfer model is smaller than that of the Woschni model, and the heat transfer rate considering the flow characteristics can be predicted.

The quasi–dimensional model can be used for predicting the thermodynamic state and performance of the SI engine under various fuels and operating conditions. Based on this, quasi–dimensional model was used in this study. Besides, since there are sub–models that can reflect the in–cylinder flow characteristics, a quasi–dimensional model could be developed to consider the effect of intracycle speed profile modulation considered in this study.

1.2.2. Engine speed profile optimization

Previous studies related to engine speed profile optimization have been investigated. Since considering the time in analyzing cycles, time, or speed related studies have been actively conducted [28]. Basic thermodynamic cycles, such as the Otto cycle or the Carnot cycle, do not consider the concept of time spent in the analysis. There was a study discussing the power output and efficiency of Carnot cycle considering the heat transfer time and finite temperature difference. Through this, studies related to finite–time thermodynamics began to be actively conducted, and not only the Carnot cycle but also other thermodynamic cycles began to be analyzed with considering the time effect.

Mozurkewich and Berry conducted a study to optimize the piston speed profile for the Otto cycle [29]. The difference from the basic Otto cycle is the replacement of the cycle's heat transfer process with the combustion process. Instead of using the actual combustion model, the cycle analysis was performed by arbitrarily changing the gas temperature and heat capacity. The effect of the gas temperature or compositions on the heat capacity of the gas is not taken into consideration. The sped profile optimization result of the modified Otto cycle that is only considered the heat capacity change by the combustion showed that the efficiency was improved by about 5 ~ 10% p over the

conventional cycle. The possibility of increasing the basic thermodynamic cycle efficiency by modulating the speed profile in the cycle was confirmed.

Based on the analysis of the basic thermodynamic cycle, the possibility of efficiency improvement through speed profile modulation of the ICE was also studied. Many studies have been conducted to improve the IC engine efficiency of various ignition types through the speed profile modulation.

Teh and Edwards studied the possibility of improving efficiency through speed profile modulation of homogeneous charge compression ignition (HCCI) engine [30]. The combustion process was simply modeled by a single–step reaction, and the heat transfer process was modified by the Hohenberg model. The mean piston speed term of the original Hohenberg model was changed to the instantaneous piston speed to reflect the effect of intracycle speed profile modulation on the heat transfer coefficient. To reduce computational costs, it is assumed that specific heat capacity of the in–cylinder gas does not change with temperature. When the optimization was performed, the efficiency was increased by 3% compared with the conventional HCCI engine. This suggests that the effect of speed profile modulation is lower than that of other studies, and no analysis has been performed for that reason.

Hoffman simulated a diesel engine using a finite combustion rate [31]. The burning rate was modeled using the correlation of time like the Wiebe function. The in–cylinder gas was assumed to be the same as the study of the heat engine instead of the real gas properties. Total burn duration was also used as a specific value. In other words, only the finite burn duration was additionally considered, and the rest was modeled in the same way as the previous study on the heat engine. In addition, the speed profile was optimized only after the start of combustion in the TDC, not full cycle optimization. This previous study was shown that the improvement of the efficiency is about 3% p.

Previous studies on the SI engine have been focused on reducing the time–loss of the SI engine rather than optimizing the speed profile. Chen conducted an experimental study to control the speed profile by combining a modified SI engine and AC motor / generator [32]. The speed profile was controlled by sinusoidal shape between the 400 and 800 RPM, and the average speed was 600 RPM. Compared to rotating at a constant speed, the maximum current required by the motor was about 60% higher, and the maximum current during power generation was similar. According to this study, the current difference between firing and motoring conditions increased by about 15% when the speed profile was modified.

Doric and Kilnar studied the effect of the longer duration around the firing TDC on the SI engine efficiency through the simulation [33]. The burning rate and heat transfer rate were calculated using the Wiebe function and Woschni model. According to this previous study, the new linkage structure that increases the duration around the firing TDC can improve the efficiency of the SI engine by about 3% and improve the efficiency for various speeds.

Lin conducted a study to obtain the optimal motion trajectory for a four–stroke free–piston engine [34]. The ICE was modeled using the Wiebe function and the Woschni heat transfer model. As with the previous studies on the optimization of heat engines, the gas properties and burn durations were assumed fixed constant values, and the ignition timing was also fixed. When the study was conducted in a simplified engine model, the efficiency of about 3% p can be increased compared to conventional engine operation. Previous studies related to the speed profile optimization were summarized in Table 1.1.

Table 1.1 Previous studies

Engine type		Method	Reference
Heat engine		Simulation	[29], [35], [36], [37]
Combustion engine	HCCI	Simulation	[30]
	CI	Simulation	[31], [38]
	SI	Simulation	[33], [39], [40], [34]
		Experiment	[32]

In previous studies of speed profile modulation through simulation, the in–cylinder gas property was assumed to be a constant that cannot reflect the temperature or composition effect. In addition, studies using the Woschni model, which are difficult to reflect the speed change in the cycle, were mainly conducted. Efforts have been made to reflect the effect of speed profile modulation using instantaneous piston speed, but this may not be enough to reflect the effect of speed profile on in–cylinder flow. When performing SI engine modeling, the burning rate is modeled using the Wiebe function. Several parameters used for the Wiebe function have been sufficiently verified for conventional SI engine operation, but not for conditions where the intracycle speed profile is modulated. Furthermore, some studies did not reflect the change in cad–based burn duration when the speed profile was changed using the cad–based Wiebe function. In order to overcome this problem, some studies have been performed by modifying the time–based Wiebe function, but this also does not reflect the effect of in–cylinder flow characteristics due to speed profile modulation. Moreover, the burning rate is difficult to account for the flame geometry. Under the speed profile modulation condition, the residence time in each cad varies, so the flame geometry differs from a conventional operation. Therefore, it may be difficult to discuss the effects of speed profile modulation in the SI engine model using the Wiebe function and the Woschni model. Previous studies

on SI engines lacked consideration of knocking. In the high load operation of the SI engine, knocking is one of the major factors that reduce efficiency. Increasing the time to stay near the TDC through speed profile modulation may be a condition that is favorable to cause knocking. Lastly, previous studies lacked a quantitative analysis of the cause of the increase in efficiency compared to conventional operation, or the analysis of which parameter affects the efficiency due to speed profile modulation.

In order to overcome these limitations, this study developed the SI engine model using the model considering the in–cylinder flow characteristics. Also included in the model is knocking, one of the factors that limit the efficiency of the SI engine. The reasons for the increase in efficiency is quantitatively analyzed, and the effect of speed profile on SI engine performance is discussed. This study mainly discussed the possibility and reason for improving the thermodynamic efficiency of SI engines through speed profile modulation. It does not include losses due to friction of the SI engine or the electrical energy charge/discharge efficiency between the battery and the motor to control the engine speed. This discussion was presented as future work.

1.3. Research objective

Based on the above sections, the necessities of study on improving the SI engine efficiency through the intracycle speed modulation are examined. In addition, previous studies about the intracycle speed modulation of the SI engine were not sufficiently studied. Therefore, the fundamental study on speed modulation was conducted through simulation in this study. Also, a study on intracycle speed modulation using a conventional slider–crank engine system in limited operating conditions by experiment was shown the possibility of speed modulating operation. The engine geometry architecture different from conventional slider–crank mechanism such as free–piston engines have been studied, so the fundamental study on the effect of piston motion is required. Therefore, effects of intracycle speed profile modulation on the SI engine thermodynamic efficiency are investigated in this study. Indicated efficiency of the engine is focused, and work transfer losses such as the friction loss are not included in this study. Under this situation, this study attempted to answer the following four questions.

1. Can the SI engine net indicated efficiency be increased through the intracycle speed profile modulation?
2. Under what operating conditions can the SI engine efficiency be increased?
3. What inefficiencies have been overcome in SI engine operation if efficiency can be increased?
4. Are there operating conditions that can additionally increase efficiency?

In order to answer the above four questions, this paper describes how the research was conducted, a description of the results, and a discussion. Thus, the methodology for doing this research is described in Chapter 2. The SI engine modeling method and trajectory optimization are explained. In Chapter 3, the results of the optimization are examined. Many of the answers to the above four questions are intended to be answered in Chapter 3 and Chapter 4. Finally, the conclusion of this study is discussed in Chapter 5.

Chapter 2. System description

2.1. SI engine modeling

In this chapter, the SI engine modeling method is summarized. It is assumed that the SI engine to be optimized in this study has the same architecture as the conventional SI engine. There is no additional device such as a heat recovery system, and the SI engine is based on the non–offset slider–crank mechanism. Pancake–shaped combustion chamber geometry was assumed to simplify combustion modeling.

However, the intracycle speed profile of the SI engine can be modulated in contrast with the conventional SI engine. Therefore, the SI engine model must include intracycle speed modulation effect. Firstly, SI engine model structure is introduced. Next, the governing equation and detailed modeling method of each process and sub–model are described.

2.1.1. System modeling and major assumption

There are two methods of SI engine modeling. The first is a three–dimensional model, and the other is zero–dimensional model. The three–dimensional model could more accurately estimate in–cylinder flow characteristics and thermodynamic state distribution than zero–dimensional model. However, since the numerical method is used for optimization, it is difficult to use three–dimensional model that requires high computational cost. Therefore, the SI engine modeling was conducted using the zero–dimensional model, which has an advantage in numerical optimization.

SI engine process is divided into compression, combustion, expansion, and gas exchange process. Compression, expansion, and gas exchange processes were modeled

using a single–zone model. It can be assumed that in–cylinder thermodynamic states such as temperature are uniformly distributed during those processes. However, the two–zone model was used for modeling the combustion process for the following two reasons. First, two–zone model can predict heat transfer more accurately. Previous studies have shown that the reduction of heat loss is significant in increasing efficiency through speed profile modulation. Second, two–zone model was used for predicting the knocking. Knocking is the limiting factor in achieving higher efficiency in SI engine operation. Thermodynamic states of unburned gas during the combustion process were needed to predict the knocking. Thermodynamic states of intake and exhaust manifold were assumed to be constant except for intake backflow gas. The detailed modeling method of backflow gas is described in chapter 2.1.3. The entire process schematic of the SI engine was shown in Figure 2.1.

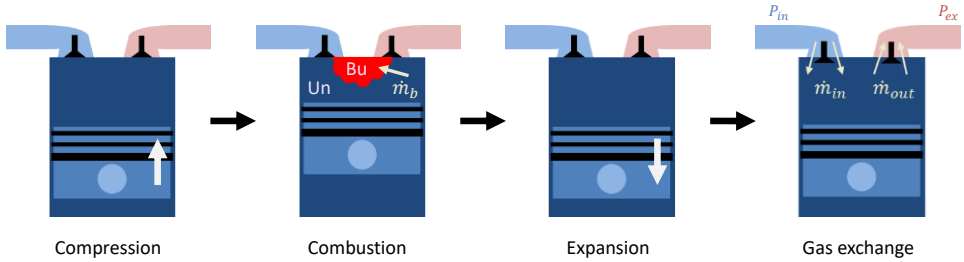

Figure 2.1 SI engine modeling

The following additional assumptions were used for modeling the in–cylinder gas states of each process.

- Frozen chemistry assumption except for the combustion process
- Hemispheric flame propagation assumption during the combustion process
- Complete combustion product is assumed to define burned zone composition
- Assume a burned mass fraction of 0.99 at the end of the combustion

Because it is not possible to accurately predict the initial state of in–cylinder thermodynamic and flow dynamic states for a specific speed profile, the simulation was iterated until steady–state conditions were satisfied. In this study, it was essential to obtain the net indicated efficiency according to the speed profile through simulation. Therefore, we used the net indicated efficiency as a steady–state criterion, as in equation (2.1). In equation (2.1), η is the efficiency, and k is the number of simulation cycles.

$$\left|1 - \frac{\eta_{k+1}}{\eta_k}\right| \leq 5 \cdot 10^{-5} \tag{2.1}$$

The governing equations to estimate in–cylinder states are introduced in section 2.1.2. Modeling methods of each process are shown in section 2.1.3, and sub–models that can reflect the intracycle speed modulation effect are summarized in section 2.1.4 to 2.1.6.

2.1.2. Governing equation

The thermodynamic state of in–cylinder gas is determined using its temperature and density. The temperature was calculated by expressing the temperature change of each zone as the ODE using the first law of thermodynamics. Heat, work, and mass transfer change the in–cylinder gas internal energy. Figure 2.2 showed the mass, heat, and work transfer in an SI engine.

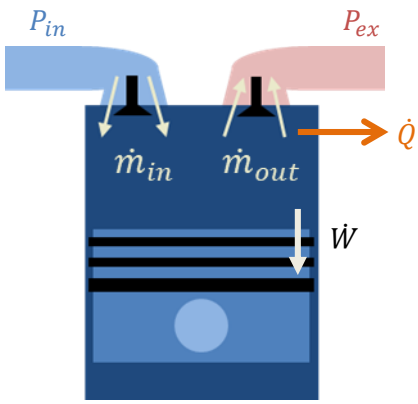

Figure 2.2 Heat, work, and mass transfer in an SI engine

Based on the first law of thermodynamics, in–cylinder gas internal energy change rates could be written as equation (2.2).

$$\dot{U}_{cyl} = -\dot{Q} - \dot{W} + h_{in} \cdot \dot{m}_{in} - h_{cyl} \cdot \dot{m}_{out} \tag{2.2}$$

Here, $\dot{U}_{cyl}$ is the in–cylinder internal energy change rates, $\dot{Q}$ is the heat transfer rates, $\dot{W}$ is the work transfer rates, h is the mass specific enthalpy, and $\dot{m}$ is the mass transfer rates. The temperature change rate is obtained using the above equation.

$$\begin{aligned} m\bar{c}_v(T) \cdot \dot{T} = -\dot{Q} - \dot{W} - \sum_j \dot{m}_j u_j(T) \\ + \sum_j \left(\dot{m}_{in,j} h_{in,j}(T_{in}) - \dot{m}_{out,j} h_{out,j}(T_{out}) \right) \end{aligned} \tag{2.3}$$

In equation (2.3), subscript j is a species index, and c_v is the specific heat capacity at constant volume. To calculate the temperature change rate, we needed to know the mass transfer rate, the concentration change rate, and the heat transfer rate. The aforementioned sub–models were used for evaluating those change rates.

The density was calculated by using the gas mass and the cylinder volume of each moment. In–cylinder gas density is obtained using in–cylinder gas mass and cylinder volume. In–cylinder gas mass changing rate could be written as equation (2.4).

$$\dot{m}_{cyl} = \dot{m}_{in} - \dot{m}_{out} \tag{2.4}$$

The cylinder volume is calculated using the engine geometry and slider–crank mechanism. The cylinder volume changing rate is written as equation (2.5).

$$\dot{V} = 0.25\pi B^2 \cdot S_p(\theta) \tag{2.5}$$

$$S_p(\theta) = 2Na \cdot \left(sin\,\theta + a \cdot \frac{sin\,\theta \cdot cos\,\theta}{\sqrt{l^2 - (a \cdot sin\,\theta)^2}} \right) \tag{2.6}$$

In equation (2.5) and (2.6), A is a piston area, S_p is an instantaneous piston speed, θ is a crank position, N is a crankshaft rotation speed, a is a crankshaft radius, and l is a connecting rod length.

Using equation (2.2) and (2.5), the temperature and density of in–cylinder gas were calculated to define the in–cylinder gas state. However, the gas composition could change during the gas exchange and combustion process. Thus, in–cylinder gas state could not be defined without considering in–cylinder gas composition. In–cylinder gas composition is calculated using the ratio of the fresh mixture and burned gas, and detailed modeling method is summarized in section 2.1.3. In–cylinder mixture properties were calculated using CANTERA, and thermodynamic data were based on the LLNL mechanism.

2.1.3. Process modeling

Typical SI engine processes are divided into compression, combustion, expansion, and gas exchange process. There is no mass transfer during the compression and

expansion process. The in–cylinder gas composition can be determined using the aforementioned assumptions. Gas composition during the compression process is the same as IVC timing composition by frozen chemistry assumption. Gas composition during the expansion process can be obtained by a complete combustion assumption. Since there is no composition change during those processes, equation (2.3) is written as below.

$$m\bar{c}_v(T)\cdot\dot{T} = -\dot{Q} - \dot{W} \tag{2.7}$$

The heat transfer rate model is described in section 2.1.5, and simple compressible work transfer is only permitted in the SI engine. In–cylinder gas temperature and density can be calculated using equation (2.5) and (2.7).

There are mass transfer and composition changes during the combustion and gas exchange process. Especially, the combustion process is modeled using two–zone model. Thus, the first law of thermodynamics is applied to each zone, respectively. First, the ignition process modeling method is summarized.

The initial state of unburned and burned zone is obtained by ignition process modeling. The combustion process of the SI engine is controlled by a spark plug. At the ignition timing, a flame kernel is formed around the spark plug tip. Flame kernel size was used for calculating initial burned zone volume. The size of the flame kernel when calculating the burned zone volume was 1 mm [41].

Some assumptions were applied to model the ignition process. First was pressure equilibrium between the burned and unburned zone. In–cylinder gas pressure equilibrium speed is faster than any other process in the SI engine except for the knocking. Thus, the pressure of the unburned and burned zone is identical at the ignition timing. The second was that the ignition process is constant volume and internal energy process. Flame kernel

developed process was assumed that instantaneous process compared with other processes, so in–cylinder gas volume and internal energy was not changed. The final assumption was that burned zone gas composition is complete combustion products. There are many methods for describing burned zone composition. Since it is hard to use accurate burned zone chemical reaction mechanism, assumed that frozen chemistry assumption. The complete–combustion assumption was suitable under the frozen chemistry assumption. The states of unburned and burned zones were obtained by iterative calculation to satisfy those assumptions. The detailed procedure of calculating is shown in Figure 2.3. Initial conditions of the unburned and burned zone at the start of combustion were obtained through the ignition process model.

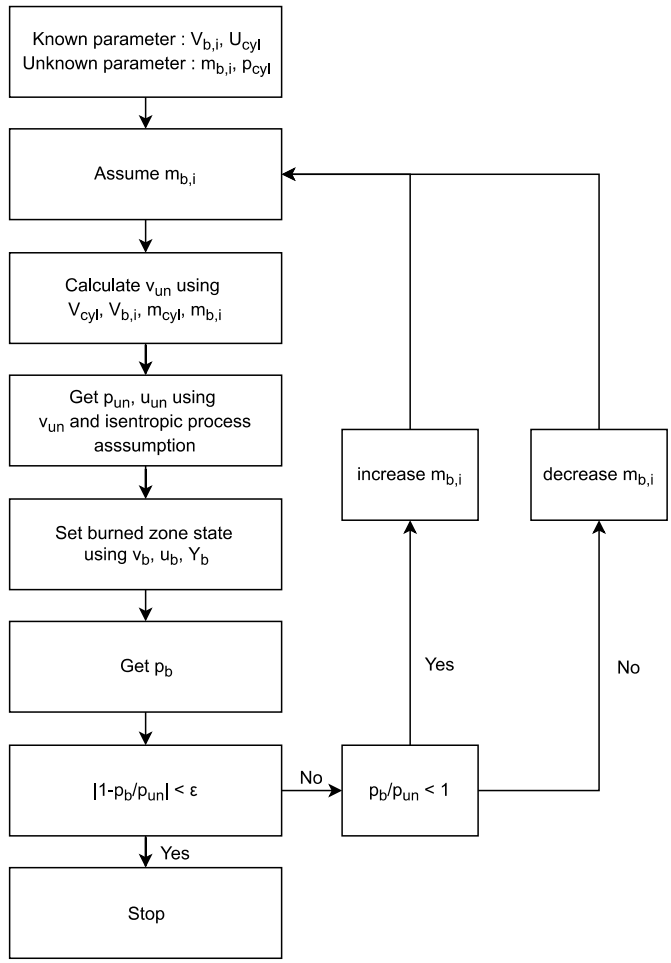

Figure 2.3 Ignition process modeling

Next is the main combustion process modeling method. By frozen chemistry assumption, there is no composition change in each zone. Equation (2.3) is re–written as below equations in each zone.

$$m_u \bar{c}_{v,u}(T_u) \cdot \dot{T}_u = -\dot{Q}_u - \dot{W}_u - \dot{m}_u u_u(T_u) + \dot{m}_u h_u(T_u) \qquad (2.8)$$

$$m_b \bar{c}_{v,b}(T_b) \cdot \dot{T}_b = -\dot{Q}_b - \dot{W}_b - \dot{m}_b u_b(T_b) + \dot{m}_b h_u(T_u) \qquad (2.9)$$

The internal energy change rate by mass transfer is considered. Since flame propagation is a source of mass transfer during the combustion process, the internal energy change rate is modeled using unburned zone enthalpy. To simplify equation (2.8) and (2.9), enthalpy of each zone can be used instead of internal energy in equation (2.10) and (2.11).

$$m_u \bar{c}_{p,u}(T_u) \cdot \dot{T}_u = -\dot{Q}_u + \dot{p}V_u \tag{2.10}$$

$$m_b \bar{c}_{p,b}(T_b) \cdot \dot{T}_b = -\dot{Q}_b + \dot{p}V_b - \dot{m}_b\big(h_b(T_b) - h_u(T_u)\big) \tag{2.11}$$

The volume change rate of the unburned and burned zone is needed to calculate the density. The ideal gas equation is used to compute the volume change rate.

$$\dot{p}V_u + p\dot{V}_u = \tilde{R}\big(\dot{N}_u T_u + N_u \dot{T}_u\big) \tag{2.12}$$

$$\dot{V}_b = \dot{V}_{cyl} - \dot{V}_u \tag{2.13}$$

For calculating above ODEs, the pressure change rate is needed, and it can be obtained using equation (2.14).

$$\dot{p}V_{cyl} + p\dot{V}_{cyl} = \tilde{R}\big(\dot{N}_u T_u + N_u \dot{T}_u + \dot{N}_b T_b + N_b \dot{T}_b\big) \tag{2.14}$$

Equation (2.10) and (2.11) are substituted into (2.14) to compute the pressure change rate.

$$\begin{aligned} \dot{p}V_{cyl} + p\dot{V}_{cyl} = \tilde{R}\Bigg(& \dot{N}_u T_u + \frac{N_u}{m_u \bar{c}_{p,u}}\big(-\dot{Q}_u + \dot{p}V_u\big) + \dot{N}_b T_b \\ & + \frac{N_b}{m_b \bar{c}_{p,b}}\Big(-\dot{Q}_b + \dot{p}V_b - \dot{m}_b\big(h_b(T_b) - h_u(T_u)\big)\Big)\Bigg) \end{aligned} \tag{2.15}$$

The above equation can be re–written as equation (2.16) based on the frozen chemistry assumption.

$$\dot{p}\left(V_{cyl}-\frac{\gamma_u-1}{\gamma_u}V_u-\frac{\gamma_b-1}{\gamma_b}V_b\right)=-p\dot{V}_{cyl}+\left(R_u\dot{m}_uT_u\right.$$
$$\left.-\frac{\gamma_u-1}{\gamma_u}\dot{Q}_u+R_b\dot{m}_bT_b-\frac{\gamma_b-1}{\gamma_b}\left(\dot{Q}_b+\dot{m}_b(h_b-h_u)\right)\right) \quad (2.16)$$

The burning rate and heat transfer rate model are introduced in section 2.1.4 and 2.1.5.

There are in–cylinder mass and composition changes during the gas exchange process. Mass transfer between the manifold and cylinder is occurred by a pressure difference or in–cylinder volume change. In–cylinder gas composition is varied during the intake process. Thus, equation (2.3) cannot be summarized in a simple form. Mass transfer rate through the intake and exhaust valve was obtained using the isentropic compressible flow relation [42].

$$\dot{m}_{valve}=C_D\frac{\sqrt{2c_p}}{R}\frac{p_o}{\sqrt{T_o}}A\left(\frac{p}{p_o}\right)^{1/\gamma}\sqrt{1-\left(\frac{p}{p_o}\right)^{(\gamma-1)/\gamma}} \quad (2.17)$$

In equation (2.17), subscript o means the reservoir gas. When the mass transfer occurs from cylinder to the manifold, in–cylinder gas is the reservoir gas. The composition change rate can be calculated using the manifold gas composition since manifold thermodynamic states are assumed to constant. However, there is backflow to intake manifold during the valve overlap process. Thus, the thermodynamic state of backflow gas modeling was needed. Some assumptions were used for modeling the backflow phenomenon. First is that the backflow process is the throttling process. Second is that backflow gas entered the cylinder earlier than fresh gas in the intake manifold. The backflow gas thermodynamic state was model as equation (2.18) ~ (2.20).

$$\dot{m}_{back}=\dot{m}_{out,intake}-\dot{m}_{in,intake}\cdot \mathrm{flag}_{back} \quad (2.18)$$

$$\dot{H}_{back} = \dot{m}_{out,intake} \cdot h_{cyl} - \dot{m}_{in,intake} h_{back} \cdot \text{flag}_{back} \tag{2.19}$$

$$p_{back} = p_{inmani} \tag{2.20}$$

In equation (2.18) and (2.19), flag_{back} variable is defined as below.

$$\text{flag}_{back} \begin{cases} = 0, & m_{back} = 0 \\ = 1, & m_{back} > 0 \end{cases} \tag{2.21}$$

In–cylinder gas thermodynamic state and composition are calculated using equation (2.3), equation (2.4), equation (2.5), and above equations.

2.1.4. Burning rate model

Wiebe function is widely used for modeling the SI engine burning rate modeling. However, both combustion duration and model coefficient is needed to use the Wiebe function. There is no correlation of burn duration in an intracycle speed profile modulating operation. Thus, the Wiebe function cannot be used for modeling the burning rate in the speed profile modulating operation case. The turbulent flame model uses in–cylinder flow characteristics to estimate the burning rate. For this reason, the turbulent flame model is used for modeling the SI engine burning rate in this study.

During the combustion process, to solve the ODEs for the unburned and burned zone needed to know the burning rate. The turbulent flame model was used for modeling the combustion process since this model reflects the in–cylinder flow dynamic characteristics. In this section, the turbulent flame model used in this study is explained.

The turbulent flame model used in this research was the entrainment and burn–p model [24]. According to the entrainment and burn–up model, unburned gas entrains to

the flame front, and then entrained unburned gas is burn–up with the specific rate. Entrainment and burning rate of unburned gas were modeled as equation (2.22) and (2.23).

$$\dot{m}_e = \rho_u A_e (u' + S_l) \tag{2.22}$$

$$\dot{m}_b = (m_e - m_b)/\tau \tag{2.23}$$

In the above equations, ρ_u is an unburned zone gas density, A_e is an area of the flame front, u' is an unburned zone turbulence speed, S_l is a laminar flame speed, and τ is a characteristic time. Characteristic time was defined as equation (2.24).

$$\tau = \lambda / S_l \tag{2.24}$$

Here, λ is the Taylor microscale, the Taylor scale is calculated using turbulent flow properties.

$$\lambda = \sqrt{15 \cdot (\nu/\epsilon)} \cdot u' \tag{2.25}$$

Here, ν is the kinematic viscosity of the gas, ϵ is the turbulent kinetic energy dissipation rate, and u' is the turbulence intensity.

Gasoline laminar flame speed was modeled using the correlation that could reflect the unburned gas temperature, pressure, and composition.

$$S_l = \left(B_m + B_\phi (\phi - \phi_m)^2\right) \left(\frac{T_u}{T_{ref}}\right)^\alpha \left(\frac{p}{p_{ref}}\right)^\beta f(\text{dilution}) \tag{2.26}$$

The dilution effect was modeled using the GT–ISE model. Parameters in equation (2.26) are summarized in Table 2.1.

Table 2.1 Coefficients of laminar flame speed correlation

B_m (m/s)	B_ϕ (m/s)	ϕ_m	α	β
0.35	–0.549	1.1	2.4–0.271ϕ	–0.357+0.14$\phi^{2.77}$

The turbulent speed of the unburned zone was calculated as equation (2.27), under the isotropic flow assumption.

$$u' = \sqrt{(2/3)k} \tag{2.27}$$

The flame front area could be calculated using flame radius, and cylinder bore size and instantaneous piston height. In pancake–shaped combustion geometry, the hemispherical flame front area could be summarized as Table 2.2.

Table 2.2 Analytic form of the flame front area

Case	Flame front area
$R_f \leq B/2$ & $R_f \leq h$	$A_e = 2\pi R_f^2$
$R_f > B/2$ & $R_f \leq h$	$A_e = 2\pi R_f^2 \, x(1-(R_f^2-(B/2)^2)^{0.5}/R_f)$
$R_f \leq B/2$ & $R_f > h$	$A_e = 2\pi R_f^2 \, x \, (h/R_f)$
$R_f > B/2$ & $R_f > h$	$A_e = 2\pi R_f^2 \, x \, (h/R_f-(R_f^2-(B/2)^2)^{0.5}/R_f)$

2.1.5. Heat transfer model

Woschni model is mainly used for modeling the SI engine heat transfer. Woschni model well estimates both the accumulative amount of heat transfer and the instantaneous heat transfer rate. Woschni proposed that the in–cylinder gas Nusselt number could be obtained using equation (2.28) [42].

$$\mathrm{Nu} = 0.035 \cdot \mathrm{Re}^{\mathrm{m}} \tag{2.28}$$

In the Woschni heat transfer model, the Reynolds number of in–cylinder gas is calculated based on the cylinder bore size and the mean piston speed. Thermal conductivity and viscosity of working fluid were converted to temperature and pressure

correlations. The in–cylinder flow speed is related to the mean piston speed. Also, in–cylinder flow fields during the combustion and expansion process are affected by flame propagation. Thus, characteristic speed during those process was modeled a sum of mean piston speed and additional terms in the Woschni model.

$$h_{conv} = 3.26B^{-0.2}p^{0.8}T^{-0.55}w^{0.8} \quad (2.29)$$

Engine flow dynamics was considered in the Woschni heat transfer model, but it is hard to reflect the intracycle speed modulation effect. When the same mean speed condition and different speed profile conditions, the instantaneous heat transfer rate is different, but the heat transfer rate is not changed in the Woschni model. To reflect this effect, Poulos model was used for modeling the heat transfer rate [43-45]. Poulos heat transfer model used the instantaneous piston speed, mean flow speed, and turbulent flow speed as a characteristic speed.

Many Nusselt number correlations used the relation between Nusselt number and Reynolds number for convective heat transfer coefficient. It is mainly used the mean flow speed for calculating Reynolds number. However, turbulent speed is additionally used. Therefore, it was necessary to confirm whether turbulent speed could affect the convective heat transfer coefficient.

There were some studies that effect of turbulent speed on the Nusselt number in the same Reynolds number condition. Those studied did not cover the in–cylinder flow, but the results were that turbulent speed could affect the Nusselt number in the flow around the cylinder case. Thus, it is assumed that turbulent speed could affect the Nusselt number in case of in–cylinder flow, and turbulent intensity was included in calculating the characteristic speed. The basic form of pipe flow heat transfer coefficient is written as equation (2.30).

$$\mathrm{Nu} = a \cdot \mathrm{Re}^{m} \cdot \mathrm{Pr}^{n} \tag{2.30}$$

Poulos assumed that the Prandtl number was 1, a was 0.07, and m was 0.8. Poulos used turbulence macroscale as a characteristic length scale. Poulos used the length scale for computing the turbulent kinetic energy dissipation rate [46]. Thus, a length scale calculated using the turbulent kinetic energy and the turbulent kinetic energy dissipation rate was used a characteristic length scale in this research. The length scale was obtained using the equation (2.31).

$$L = C_{\epsilon} u'^{3} / \epsilon \tag{2.31}$$

The geometric length scale was generally used for modeling the convective heat transfer coefficient. Thus, it is needed to confirm the turbulent length scale affect the convective heat transfer coefficient. There were some studies about the effect of the turbulent length scale on the Nusselt number. As a result, the turbulent length scale was used to the characteristic length scale for calculating the characteristic length scale. Then, the characteristic velocity for the Reynolds number was calculated as the equation (2.32).

$$w = \sqrt{U^{2} + u'^{2} + \left(S_p/2\right)^{2}} \tag{2.32}$$

Mean kinetic energy did not include the piston motion as described in section 2.1.6, so instantaneous piston speed term was included for calculating characteristic speed. Since gas speed near the piston is the same as the piston speed, but gas speed near the cylinder head is nearly zero, the in–cylinder gas speed was halved instantaneous piston speed.

2.1.6. The in–cylinder flow dynamics model

The in–cylinder turbulence model was needed to use the turbulent flame model and convective heat transfer model. In this paper, the zero–dimensional k–ε model was used for modeling the in–cylinder flow dynamics. Thermodynamic states were modeled using the zero–dimensional model, so zero–dimensional model was also used to model the in–cylinder flow dynamics.

There are many models based on the zero–dimensional turbulence model. One equation model solves only the turbulent kinetic energy, and the turbulent length scale was modeled using the geometric condition. To calculate the turbulent length scale of the unburned zone, an additional assumption was needed in the one equation model [47]. However, k–ε model does not require additional assumptions to calculate the unburned zone length scale. In k–ε model, the turbulent length scale can be obtained using the turbulent kinetic energy dissipation rate and turbulent kinetic energy. Therefore, zero–dimensional k–ε model was used in this study.

To compute terms in the k–ε model, mean velocity field information is required. There was no mean flow filed model in the thermodynamic model and turbulence model. Thus, the mean flow field was modeled based on the mean kinetic energy, and the gradient of mean velocity was modeled artificial gradient based on the cylinder geometry condition.

The in–cylinder flow dynamic energy transfer diagram is shown in Figure 2.4. There are two sources of mean motion. One is the induced motion by incoming gas through the valve, and the other is induced by the piston movement. This mean kinetic energy (K, MKE) is dissipated to turbulent kinetic energy (k, TKE). The other source of TKE is incoming flow. TKE is dissipated to the heat, but the heat is not considered in temperature

change rate because converted heat is minimal compared to the in–cylinder internal energy.

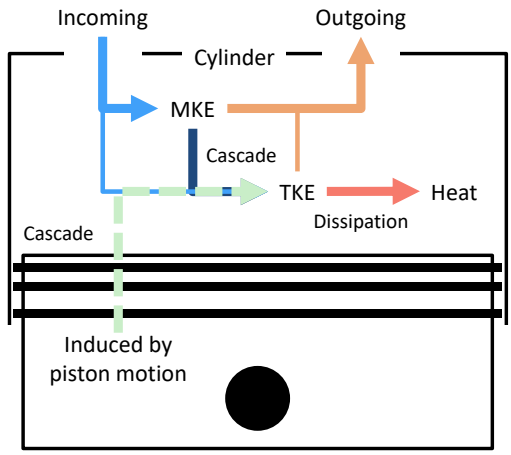

Figure 2.4 Flow dynamic energy flow diagram

Mean kinetic energy, turbulent kinetic energy, and turbulent kinetic energy dissipation rate could be modeled as equation (2.33) ~ (2.35). Each energy could be varied with mass transfer, production, and destruction. According to the energy conservation law, both MKE and TKE were not produced nor destructed, and only converted to the other energy form.

$$(m_{cyl}\dot{K}_{cyl}) = I_K - O_K - P_{MKE} \tag{2.33}$$

$$(m_{cyl}\dot{k}_{cyl}) = I_k - O_k + P_{TKE} - m \cdot \epsilon_k \tag{2.34}$$

$$(m_{cyl}\dot{\epsilon}_{cyl}) = I_\epsilon - O_\epsilon + P_\epsilon - m \cdot \epsilon_\epsilon \tag{2.35}$$

MKE can be increased through the mass transfer from the manifold to the cylinder and decreased through the outward mass transfer and converting to the TKE. In this research, the MKE term does not include gas motion induced by the piston movement. Thus, P_{MKE} term can be written as equation (2.36) [46-48].

$$P_{MKE} = \mu_t \cdot C_{shear} \cdot \left(\frac{2K_{cyl}}{L_{mean}^2} \right) \tag{2.36}$$

In equation (2.36), K_{cyl} is the in–cylinder mass specific MKE, μ_t is the turbulent viscosity, L_{mean} is the geometric length scale, and C_{shear} is the tuning parameter. Turbulent viscosity and geometric length scale could be calculated using equation (2.37) and (2.38) [48, 49].

$$\mu_t = 0.09 m_{cyl} \cdot \left(\frac{k_{cyl}^2}{\epsilon_{cyl}} \right) \tag{2.37}$$

$$L_{mean} = 0.19 \cdot \min\left(h_{cyl}, B/2\right) \tag{2.38}$$

Therefore, P_{MKE} is the converting rate from the MKE induced during the intake process to the TKE. However, there is another mean speed gradient that is induced by the piston movement. TKE change rate has modeled the sum of P_{MKE} and piston motion effect. To do this, the governing equation of TKE was examined[50].

$$\frac{\mathrm{D}k}{\mathrm{D}t} = \frac{\partial}{\partial x_i}\left[(\mu + \mu_t) \frac{\partial k}{\partial x_i} \right] + \frac{\sigma_{ij}^t}{\rho} \frac{\partial U_j}{\partial x_i} - \epsilon \tag{2.39}$$

In equation (2.39), the first term of the right–hand side is the diffusion of TKE, second term is TKE production, and the final term is dissipation rate. Since the flow model was based on the zero–dimensional model, diffusion term was not considered in this model.

For calculating the converting rate, σ_{ij}^t was needed to model. This term is the Reynolds stress. The basic method of modeling the Reynolds stress is using the analogy with the viscous stress. Under a compressible flow case, viscous stress could be written as (2.40).

$$\sigma = \zeta(\nabla \cdot U)\mathrm{I} + \mu\left(\nabla U + (\nabla U)^{\mathrm{T}} - \frac{2}{3}(\nabla \cdot U)\mathrm{I}\right) \tag{2.40}$$

In equation (2.40), ζ is the bulk viscosity, μ is the fluid viscosity, and U is the mean flow velocity. Bulk viscosity of real gas is not zero, and there are many studies on measuring the bulk viscosity [51]. However, the bulk viscosity is assumed to be zero based on the Stokes' hypothesis in this paper because it is hard to find the bulk viscosity of in–cylinder gas, and simplification of the model was needed. Many three–dimensional and zero–dimensional simulation studies have used Stokes' hypothesis. Therefore, compressible flow Reynolds stress could be written as equation (2.41).

$$\sigma^t = \mu_t\left(\nabla U + (\nabla U)^T - \frac{2}{3}(\nabla \cdot U)I\right) \tag{2.41}$$

Other Reynolds stress tensor form in Reynolds averaged Navier–Stokes (RANS) equation is written as equation (2.42). Thus, the trace of the Reynolds stress tensor is different between using the equation (2.41) and the equation (2.42).

$$\sigma^t = -\rho\overline{u_i' u_j'} \tag{2.42}$$

Thus, an additional term is needed to equation (2.41). Equation (2.43) is the final form of Reynolds stress tensor, considering the trace value.

$$\sigma^t = \mu_t\left(\nabla U + (\nabla U)^T - \frac{2}{3}(\nabla \cdot U)I\right) - \frac{2}{3}\rho k \tag{2.43}$$

THE production rate for compressible flow can be written as (2.44).

$$P_{TKE} = \mu_t\left[\left(\frac{\partial U_j}{\partial x_i} + \frac{\partial U_i}{\partial x_j}\right)\right]\left(\frac{\partial U_i}{\partial x_j}\right) - \frac{2}{3}\mu_t\left(\frac{\partial U_k}{\partial x_k}\right)^2 - \frac{2}{3}\rho k\left(\frac{\partial U_k}{\partial x_k}\right) \tag{2.44}$$

For applying the above equation to the zero–dimensional model, the continuity equation was used for calculating the velocity gradient. In zero–dimensional model, there

was no spatial gradient of thermodynamic and flow dynamic properties. In–cylinder gas density can be varied with respect to the time, and there is no spatial distribution. Therefore, the continuity equation (2.45) could be written as equation (2.46).

$$\dot{\rho} + \nabla \cdot (\rho u) = 0 \tag{2.45}$$

$$\nabla \cdot u = \left(\frac{\partial U_k}{\partial x_k}\right) = -\left(\frac{\dot{\rho}}{\rho}\right) = \frac{S_p(t)}{h(t)} = \frac{\partial \mathrm{U}_3}{\partial x_3} \tag{2.46}$$

According to the continuity equation, the in–cylinder gas velocity gradient is induced by the piston movement. The piston motion effect could be calculated using the continuity equation. Velocity gradient term except for piston motion could be modeled as equation (2.47).

$$\frac{\partial U_i}{\partial x_j} = \frac{\sqrt{2K}}{L_{mean}} \quad (i \neq j) \tag{2.47}$$

Equation (2.47) was used for modeling converting from the MKE to the turbulent kinetic energy. The final form of the TKE production rate could be written as equation (2.48).

$$P_{TKE} = \mu_t \frac{2K}{L_{mean}^2} + 2\mu_t \left(\frac{\dot{\rho}}{\rho}\right)^2 - \frac{2}{3}\mu_t \left(\frac{\dot{\rho}}{\rho}\right)^2 + \frac{2}{3}\rho k \left(\frac{\dot{\rho}}{\rho}\right) \tag{2.48}$$

Equation (2.49) is the governing equation of the dissipation rate based on the k–ε model.

$$\frac{\mathrm{D}\epsilon}{\mathrm{D}t} = \frac{\partial}{\partial x_i}\left[\frac{(\mu + \mu_t)}{\sigma_\epsilon}\frac{\partial \epsilon}{\partial x_i}\right] + C_{1\epsilon}\frac{\epsilon}{k}\frac{\sigma_{ij}^t}{\rho}\frac{\partial U_j}{\partial x_i} - C_{2\epsilon}\frac{\epsilon}{k}\epsilon + m\epsilon\left(-\frac{\partial U_k}{\partial x_k}\right) \tag{2.49}$$

The diffusion term was neglected due to the zero–dimensional model. $C_{1\epsilon}$ and $C_{2\epsilon}$ are 1.44 and 1.92, respectively, in many studies. However, another value was used for considering the compressible effect [50]. In–cylinder flow from the IVC timing to the EVO timing is compressible flow. Thus, additional coefficients are added to the equation (2.49). The in–cylinder gas is compressed on the z–axis direction (cylinder axis direction). The TKE production term and final term of equation (2.49) are related to the compressible factors. Factors related to the compressible flow include a velocity divergence term. Therefore, the compressible flow dissipation rate could be written as an equation (2.50).

$$P_\epsilon = \frac{\epsilon}{k}\left[2C_{11}\cdot\mu_t\left[\left(\frac{\partial U_j}{\partial x_i}+\frac{\partial U_i}{\partial x_j}\right)\right]\left(\frac{\partial U_i}{\partial x_j}\right)-\frac{2}{3}C_{12}\mu_t\left(\frac{\partial U_k}{\partial x_k}\right)^2 - \frac{2}{3}C_{13}mk\left(\frac{\partial U_k}{\partial x_k}\right)\right] \tag{2.50}$$

Each coefficient is summarized in Table 2.3 [50].

Table 2.3 Coefficient of dissipation rate production term

	Gosman and Watkins	ρL^n = constant		
		Spherical (n = 3)	Cylindrical (n = 2)	Unidirectional (n = 1)
C_{11}	1.44	1.44	1.44	1.44
C_{12}	1.44	1.44	1.41	1.32
C_{13}	1.44	3.5	3.75	4.5

Since the in–cylinder compression is the unidirectional compression, the equation (2.51) is the summarized form of the dissipation rate governing equations.

$$\frac{D\epsilon}{Dt} = \frac{\epsilon}{k}\left(2C_{11}\cdot\mu_t\frac{2K}{L_{mean}^2}-\frac{2}{3}C_{12}\mu_t\left(\frac{\dot{\rho}}{\rho}\right)^2+\frac{2}{3}C_{13}\rho k\left(\frac{\dot{\rho}}{\rho}\right) - C_{2\epsilon}\epsilon\right)-\mathrm{m}\epsilon\left(\frac{\dot{\rho}}{\rho}\right) \tag{2.51}$$

Equations (2.52) ~ (2.54) are the in–cylinder flow dynamic governing equations in this study.

$$(m_{cyl}\dot{K}_{cyl}) = I_K - O_K - \mu_t \cdot C_{shear} \cdot \left(\frac{2K_{cyl}}{L_{mean}^2}\right) \tag{2.52}$$

$$(m_{cyl}\dot{k}_{cyl}) = I_k - O_k + \mu_t \frac{2K_{cyl}}{L_{mean}^2} + 2\mu_t \left(\frac{\dot{\rho}}{\rho}\right)^2 - \frac{2}{3}\mu_t \left(\frac{\dot{\rho}}{\rho}\right)^2 + \frac{2}{3}\rho k_{cyl}\left(\frac{\dot{\rho}}{\rho}\right) - m_{cyl} \cdot \epsilon_{cyl} \tag{2.53}$$

$$\begin{aligned}(m_{cyl}\dot{\epsilon}_{cyl}) = {} & I_\epsilon - O_\epsilon \\ & + \frac{\epsilon}{k}\left[2C_{11} \cdot \mu_t \left[\frac{\dot{\rho}}{\rho} + \frac{2K_{cyl}}{L_{mean}^2}\right] - \frac{2}{3}C_{12}\mu_t \left(\frac{\dot{\rho}}{\rho}\right)^2 \right. \\ & \left. + \frac{2}{3}C_{13}mk\left(\frac{\dot{\rho}}{\rho}\right)\right] - \mathrm{m_{cyl}}\epsilon_{\mathrm{cyl}}\left(\frac{\dot{\rho}}{\rho}\right) \\ & - C_{2\epsilon}m_{cyl}\frac{\epsilon_{cyl}}{k_{cyl}}\,\epsilon_{cyl}\end{aligned} \tag{2.54}$$

The MKE, TKE, and epsilon change rates by the mass transfer are needed to calculate the above equations. Firstly, the transfer of flow dynamic properties during the combustion process are written. Unburned zone–specific MKE, TKE, and epsilon are used during the combustion process because unburned zone mass is transferred to the burned zone during the combustion process.

$$I_{X,bu} = O_{X,un} = \dot{m}_b X_{un} \tag{2.55}$$

Next, flow dynamic properties change rates due to mass transfer during the gas exchange process are introduced. Gas speed was calculated by dividing the mass transfer rate through the valve into the gas density and valve curtain area. MKE could be calculated using this gas speed and loss term due to the non–isentropic process. The loss term was modeled using the valve and cylinder geometry information [52].

In this study, the turbulence properties of inward mass flow could not be directly calculated because additional manifold modeling was not conducted. Thus, it was

assumed that some portion of the incoming MKE is converted TKE. Epsilon was considered due to the governing equation form is the same as that of TKE. In the previous study, a maximum valve lift was used as a length scale for calculating epsilon [53]. In this study, the instantaneous valve lift was used as a length scale due to the instantaneous valve lift that can more represent the geometry condition of the incoming flow. Inward MKE, TKE, and epsilon were calculated as equation (2.56) ~(2.60).

$$K_{in} = \frac{1}{2}(1 - c_{loss})v_{ps}^2 \tag{2.56}$$

$$c_{loss} = 1 - \left(A_{curtain}/A_{cyl}\right)^n, \mathrm{n} = 0.8 \tag{2.57}$$

$$v_{ps} = \dot{m}_{in}/\rho_{manifold} \,/\, A_{curtain} \tag{2.58}$$

$$k_{in} = C_k \cdot K_{in} \tag{2.59}$$

$$\epsilon_{in} = C_{\epsilon,in}\left(\frac{2}{3}\right)^{1.5} k_{in}^{1.5} \,/\, L_{valve} \tag{2.60}$$

2.1.7. Knock model

Knock onset timing was estimated using the Livengood–Wu integral method in this study. Livengood–Wu integral method used the ignition delay of the unburned mixture during the compression and combustion process [54]. Equation (2.61) is Livengood–Wu integration.

$$\mathrm{LW} = \int_{t_0}^{t_f} \frac{1}{\tau_{ig}(T,P)}\,\mathrm{d}t \tag{2.61}$$

When Livengood–Wu integral value reaches 1, the auto–ignition of an unburned mixture occurs. Ignition delay value was needed to calculate the Livengood–Wu integral value. The reduced chemical reaction mechanism was used for modeling the ignition delay of the gasoline surrogate mixture [55]. Surrogate fuel of the referred research was

RD 387. In the reference paper, representative four species were selected to modeling the RD 387. Fuel composition in the reduced chemical reaction was summarized in Table 2.4. This surrogate included primary reference fuel, toluene, and cyclohexane.

Table 2.4 Reduced composition for RD 387 surrogate fuel

Cyclohexane	26.4
Toluene	35.9
n–Heptane	10.9
Isooctane	26.8

Ignition delay of AKI 87 fuel was calculated under the various temperature, pressure, and residual mass fraction using this reduced chemical reaction mechanism. The temperature range was 500 to 1,200 K with 10 K intervals, the pressure range was 10 to 60 bar with 5 bar intervals, and the residual mass fraction was 0 to 0.5 with 0.02 interval. And then, interpolation was conducted using the MATLAB curve fitting toolbox. Interpolation function was used for Livengood–Wu integration during the compression and combustion process. Reduced chemical reaction mechanism compared with the Douaud–Eyzat ignition delay correlation that was widely used for estimating knock onset timing. Livengood–Wu integral value was calculated with specific operating conditions.

Figure 2.5 shows that Livengood–Wu integration was conducted with two different ignition delay model at intake manifold pressure is 1 atm and spark timing is bTDC 40 cad condition. According to the simulation results, knock onset timing was aTDC 6.1 cad with reduced chemical reaction mechanism and was aTDC 5.4 cad with Douaud–Eyzat correlation. Therefore, two ignition delay models are not different at typical engine operating conditions. In this research, the reduced chemical reaction mechanism was used due to future work about the high EGR or lean–burn operating conditions.

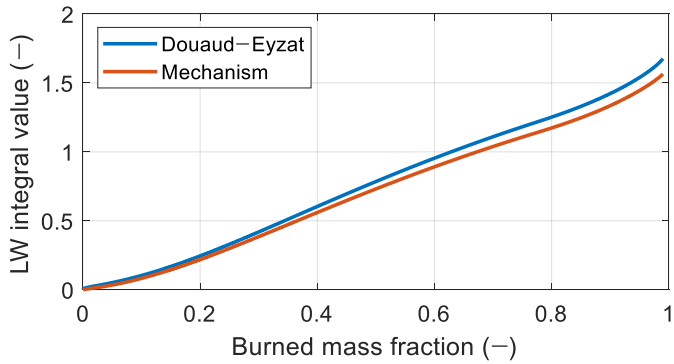

Figure 2.5 Livengood–Wu integral value comparison

Remained unburned mass fraction was used for estimating the knock intensity. There are lots of knock intensity estimation models. Using the remained unburned mass fraction method required small modeling constant. According to the previous research, knock intensity related to the remained unburned mass fraction. In this research, assumed that the SI engine could stable operate until the slight knock condition. Therefore, remained unburned mass fraction was allowed lower than 0.015 and used this value as a constraint in the optimization problem [56].

2.2. Trajectory optimization

An optimal speed profile for maximizing the net indicated efficiency of the SI engine was found using the developed SI engine model. In this optimization problem, the problem domain is not parameters but function because control input is speed profile along with the time or crank position. Therefore, the problem is a kind of trajectory optimization problem.

The direct or indirect method is used for solving the trajectory optimization problem [57]. Firstly, the indirect method is based on the necessary condition of an optimum point. The necessary condition is that a gradient vector at the optimum point is zero vector. The trajectory optimization problem is converted to the two–point boundary problem using the necessary condition and costate variable. The direct method is based on the discretization. Crank position or time interval is discretized into N intervals, and then the function value at each interval is calculated using the piecewise–continuous interpolating function. The trajectory optimization problem is converted to the parameter optimization problem with the direct method

The indirect method has advantages in accuracy and system identification. However, it is hard to obtain analytic equations of necessary conditions for the complex system. The accuracy of the direct method is lower than the indirect method, but additional equations are not needed to solve the optimization problem. Thus, the direct method is more suitable for solving the optimization problem of the complex system.

In this study, it is hard to obtain the analytic form of partial differentiation of indicated net efficiency with respect to the speed. It is difficult to predict the initial condition under the given speed profile since the SI engine model is highly non–linear. Heat transfer rate, burning rate, and turbulent properties affect each other, thus finding an

analytic form of gradient vector with respect to the speed profile is hard. As a result, the direct method was used for solving the trajectory optimization problem in this study.

SI engine with the specific speed profile simulated until the net indicated efficiency convergence. The initial condition of the SI engine model for the specific speed profile could not be accurately predicted. Thus, the simulation was iteratively conducted with a specific speed profile.

A detailed optimization procedure will be introduced from section 2.2.1 to section 2.2.4.

2.2.1. Discretization

The direct method changes the control input domain of the optimization problem from function to real–value set. This conversion was performed with N interpolating points and interpolating function. Piecewise cubic Hermite function provided by the MATLAB curve fitting toolbox was used for interpolating function. The trajectory optimization problem was converted to the parameter optimization problem, as shown in Table 2.5.

Table 2.5 Conversion from trajectory optimization problem to the parameter optimization problem

Original Problem	Modified Problem
find $N(\theta)$ and θ_{sp} such that,	find N_1, …, N_m, and θ_{sp} such that,
$\text{maximize}\ \eta_{net}$	$\text{maximize}\ \eta_{net}$
subject to,	subject to,
$N(\theta) \in \mathbb{C}^1$	$N_i \in \mathbb{R}$
$N_{lb} \leq N(\theta) \leq N_{ub}$	$N_{lb} \leq N_i \leq N_{ub}$
$UMF_{@LW=1} \leq UMF_c$	$UMF_{@LW=1} \leq UMF_c$
$\left\|1 - \eta_{net,k}/\eta_{net,k+1}\right\| \leq 5 \cdot 10^{-5}$	$\left\|1 - \eta_{net,k}/\eta_{net,k+1}\right\| \leq 5 \cdot 10^{-5}$

And then, the number of interpolating points was determined. If the number of interpolating points increases, the difference between the approximated optimum function and exact optimum decreases, but the required computational cost increases. In this study, SI engine simulation was requested to evaluate the objective function. Also, the number of function evaluations is increased much more than the number of design variables increasing. Therefore, proper the number of interpolating points is determined. In order to determine the number of interpolating points, the optimization problem was solved by changing the number of interpolating points. Optimization results are shown in Figure 2.6. The net indicated efficiency increases as increasing the number of interpolating points.

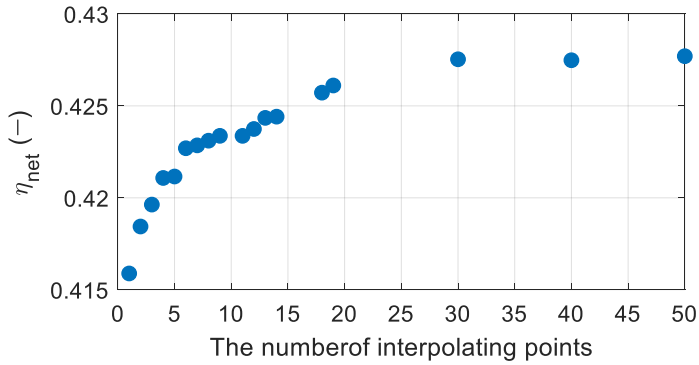

Figure 2.6 Relation between the number of interpolating points and efficiency

If the efficiency of fifty interpolating points case is assumed to the maximum value, the relative difference plot, as shown in Figure 2.7. Relative difference is defined as equation (2.62).

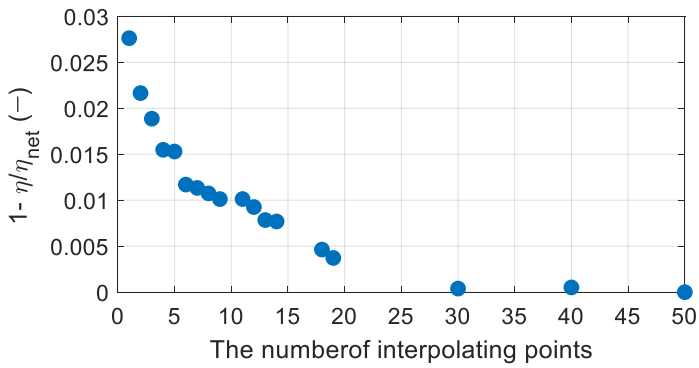

Figure 2.7 Relative efficiency difference

$$\text{Relative Difference} = 1 - \frac{\eta_{net}}{\eta_{net,N=50}} \tag{2.62}$$

As the number of interpolating points increasing, relative difference converges to zero. In this study, the number of interpolating points was determined on the minimum number when the relative difference is less than 0.005.

Therefore, the SI engine cycle was discretized with eighteen interpolating points with a piecewise cubic Hermite function. Time duration can be changed when the speed

profile varies. Thus, the SI engine cycle was discretized based on a crank position. Also, the speed profile must meet the periodic condition. In order to meet this constraint, start and end of speed profile are modified to constant speed. Figure 2.8 shows that the periodic condition of the speed profile is satisfied. The additional point is added 10 cads after IVC timing. The derivative of speed is matched by adding the interpolating point.

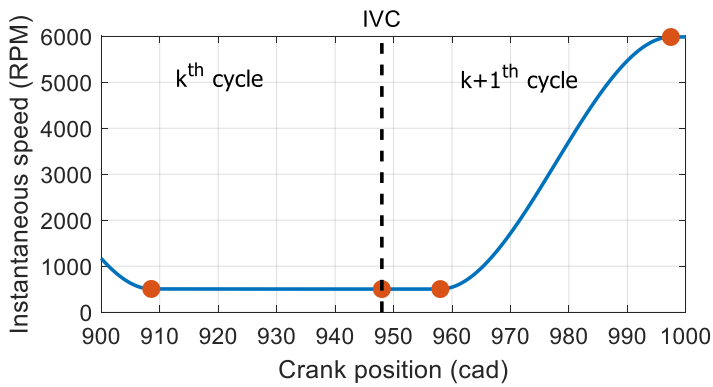

Figure 2.8 Periodic condition of the speed profile

2.2.2. Derivative free optimization

Since the spark timing controls the SI engine ignition timing, spark timing has a significant influence on the SI engine efficiency. Therefore, spark timing is included optimization parameters as eighteen interpolation points.

Gradient–based optimization uses the gradient vector calculated at the k^{th} iteration point when finding the $(k+1)^{th}$ iteration point. Many NLP solving algorithms use gradient–based methods, and MATLAB optimization toolbox provides gradient–based solvers. It is important to obtain the gradient vector correctly when using gradient–based methods.

Two methods could be used for calculating the gradient vector. First is that the gradient vector is obtained by partially differentiating the objective function with respect

to design variables. This method has an advantage in computation costs. However, it is difficult to analytically calculate the gradient vector in this study for the aforementioned reasons. The other method is to obtain the gradient using the numerical method. This method is based on objective function values. Therefore, the gradient vector could be obtained even for a complex system with a high computational cost. However, when calculating the gradient using the numerical method, the objective function must change smoothly with respect to the design variable change. It is difficult to accurately calculate a gradient vector if the objective function value non–smoothly varies. The SI engine model developed in this study showed that the indicated net efficiency did not change smoothly due to the high nonlinearity of ODE. This phenomenon became more prominent as design variables reached the optimum point.

Figure 2.9 shows the result of net indicated efficiency evaluation by varying the speed of a specific point for an arbitrary speed profile. The below graph shows the results of decreased ODE solver tolerance. The red line indicates the convergence condition of the developed model. The net indicated efficiency between two red lines is not different from the efficiency of the original speed profile. If the objective function changes smoothly according to the speed change, it depends on Δx. As shown in the left–most graph, when Δx is small, it does not change smoothly. However, when the scale of Δx is increased ten times or a hundred times, the net indicated efficiency smoothly changes with respect to the speed change. The tolerance of the ODE solver is also affected, but the trend does not change. To smoothly change the efficiency with respect to the speed change, the variation can be obtained in a smooth form by calculating Δx in the gradient calculation.

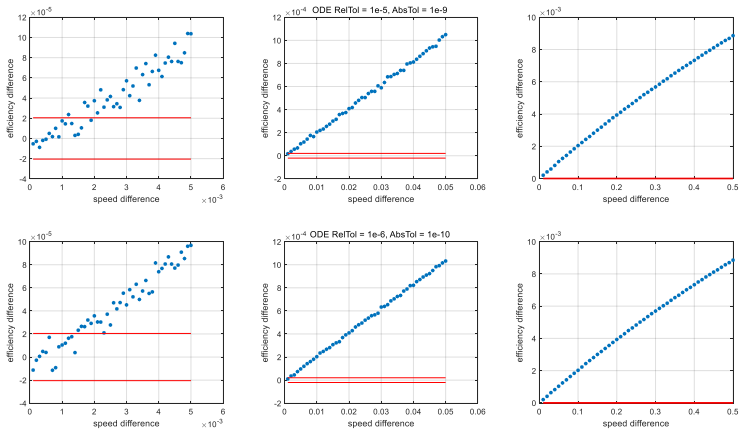

Figure 2.9 Gradient values in the arbitrary speed profile

Figure 2.10 shows the results of performing the same procedure for the optimal speed profile. Since the point is the optimal point, the gradient should be zero. However, even when the step size is small, some points are calculated to have specific gradient values. If the step size is increased to show a stable gradient value from the previous result, the gradient is not zero at the optimal point.

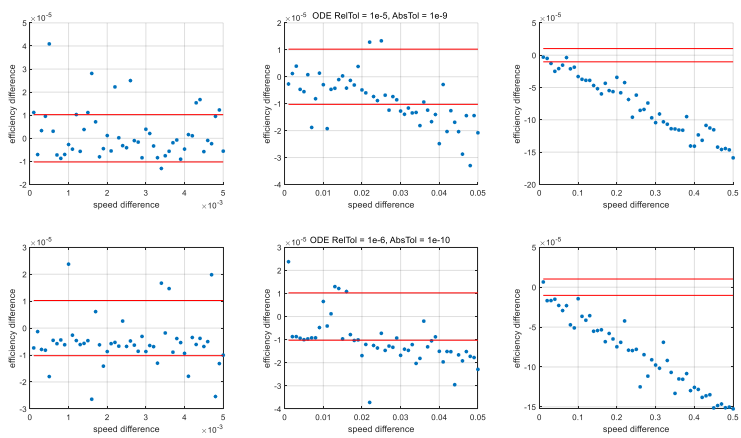

Figure 2.10 Gradient values in the optimal speed profile

To calculate the gradient in both cases, the objective function value must smoothly change with respect to varying design variables. However, the developed model does not smoothly change because it is a highly nonlinear model. Because of these problems, it is difficult to construct a gradient vector with respect to design variables using the developed SI engine model. Therefore, the gradient–based optimization method was not used in this study.

An alternative optimization method performs optimization using the objective function value directly. Step size and moving direction are based on the objective function value instead of the gradient vector. An alternative method has a disadvantage in that computational cost is higher than that of the gradient method, but it is a more stable method under using the highly nonlinear model. A typical derivative–free optimization algorithm that can be used in MATLAB is the 'patternsearch' method. The 'patternsearch' method does not use gradients and can be used even if the objective function does not change smoothly. The 'patternsearch' algorithm is shown in Figure 2.11.

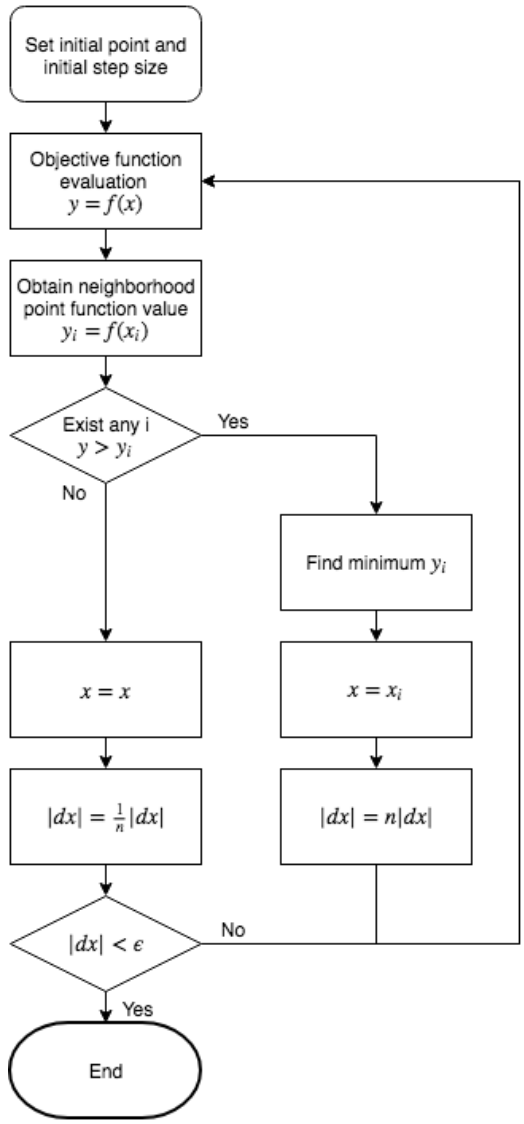

Figure 2.11 Patternsearch algorithm

The method of finding neighborhood points in the flowchart above also provides several options in MATLAB. In this study, the complete search option was used. Therefore, the objective function evaluation is made by changing ± dx for each design variable, and the iteration point is moved to the minimum of these. If the objective function value of all neighborhood points is higher than the objective function value of

the current iteration point, the iteration point does not move and repeats the above procedure by cutting the dx value in half. Through the derivative–free optimization algorithm, the disadvantage of the developed model can be overcoming.

2.2.3. Construct subproblem

When SI engine simulation is performed for a given manifold condition and engine geometry condition, the efficiency can be varied by modulating the intracycle speed profile, but the spark timing also has a significant influence on the SI engine efficiency. Spark timing should also be optimized when speed profile optimization. Therefore, when using the 'patternsearch' algorithm introduced above, the design variable should be optimized by including not only the speed of each interpolation point but also the spark timing.

The effects of speed and spark timing on SI engine efficiency are different. Therefore, the optimization result is not an efficiency maximized speed profile but an optimal speed profile for a specific spark timing. To solve this problem, changing the scale of speed and spark timing was adopted. When the same dx shifts design variables if the change of interpolation point speed is relatively significant, the effect of speed and spark timing on efficiency can be similar. The scaling factor was used in the following way.

$$\widetilde{N} = N \cdot \frac{1}{SF_{speed}}, \tilde{S}_p = Sp \cdot \frac{1}{SF_{spark}} \tag{2.63}$$

The SF_{speed} value was set to 1,000, and the results of unconstrained optimization were compared with changing the SF_{spark}. If SF_{spark} is large, spark timing is mostly affected by the same dx, so it is easy to fall into a local minimum for a given spark timing. Therefore, when SF_{spark} is large, the efficiency of the optimum point is low. However, even when

SF_{spark} is low, the convergence of the efficiency of the calculated optimum point is inferior. This means that optimization was finished at the local optimum point rather than the global optimum point.

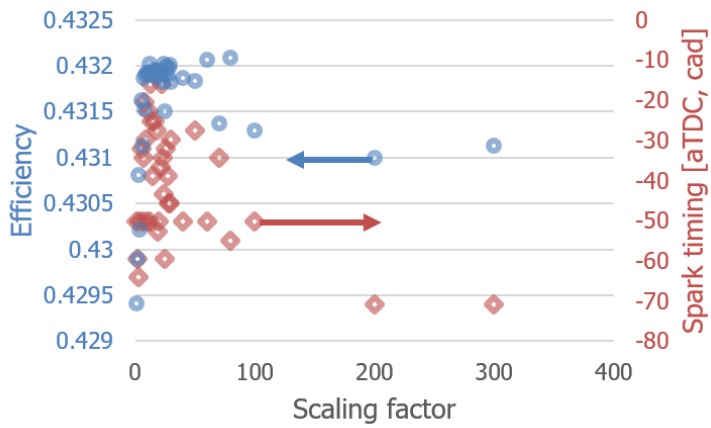

Figure 2.12 Effect of the scaling factor on the optimization results

Therefore, it was challenging to find the global optimum point avoiding the local minimum by adjusting the scaling factor. The optimization based on the numerical method is difficult to guarantee the global optimum point. Furthermore, in this optimization problem, if spark timing was included in the design variables, there may be numerous local minimums with optimum speed profiles for each spark timing. Consequently, spark timing is separately found to overcome this problem.

First, the optimum speed profile was found by using the 'patternsearch' algorithm, and the objective function value representing the efficiency of a specific speed profile was set to the efficiency at optimal spark timing. Therefore, a subproblem that finds the optimal spark timing was constructed to obtain the spark timing that maximizes the efficiency for a given speed profile. The 'fminbnd' algorithm was used for finding the spark timing that maximizes efficiency.

When the optimal speed profile was found by dividing the problem into the speed profile and the spark timing optimization problem, it was confirmed that the convergence of the efficiency and the speed profile was high for different initial conditions. When six optimizations were performed at a random initial point, the normalized standard deviation of efficiency was 9.42×10^{-5}, and the standard deviation of spark timing was 0.12 deg.

2.2.4. Constrained optimization

Even if the problem was solved using the above–described method, convergence was inferior when the constrained optimization problem was solved. This phenomenon is caused by applying the penalty to the constraint function. The penalty function is calculated by multiplying the penalty factor by the amount exceeding the constraint function.

Constraint functions in this study are average speed and the remaining unburned zone mass fraction at knock onset timing. Both were converted to nonlinear inequality form and added to the nonlinear constraint, and the optimal speed profile shows that the convergence of results was deteriorated.

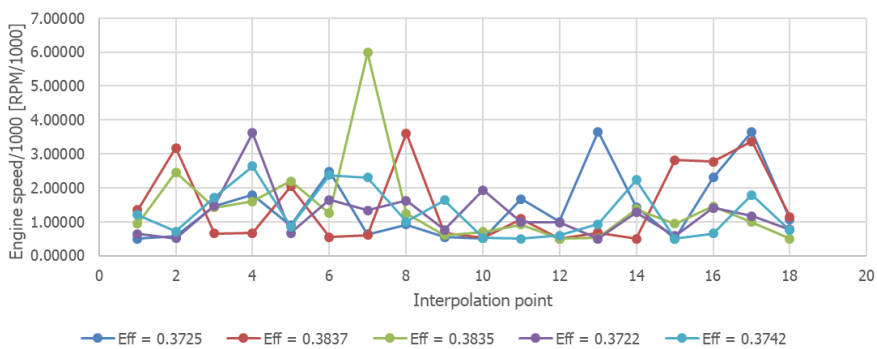

Figure 2.13 Average speed constrained the result

Not only deteriorated convergence of speed profiles, but the convergence of the efficiency calculation is also worsened. To solve this problem, instead of using the built–in constraint optimization algorithm, the modified penalty function was used for solving the problem.

In the built–in constrained optimization solver algorithm, the initial penalty factor was set to the large value to move the design variable in the feasible point. Then, the penalty factor was decreased to find the optimal point. In this average speed constrained problem, the initial significant penalty factor has a great influence on solving the optimization problem. Thus, the modified penalty factor was initially set to the small value, and it is gradually increased to move the design variables into a feasible point. In addition, the convergence could be improved by increasing the penalty factor little by little, instead of shifting the point dominated by constraints. When both average speed and unburned mass fraction at knock onset timing constraints are applied, the objective function is defined as follows.

$$\begin{aligned} f = &-\eta + pf_{knock} \cdot max(0.985 - BMF_{@LW=1}, 0) \\ &+pf_{speed} \cdot max\left(abs\left(1 - N_{avg}/N_{target}\right) - 0.01, 0\right) \end{aligned} \tag{2.64}$$

For the average speed constraint, 1 % tolerance is allowed. If tolerance is not permitted, the region of feasible points will converge to the feasible line. The performance of a numerical optimization solver is not guaranteed in an optimization problem with limited feasible points. Therefore, this slight tolerance was allowed for a stable optimization solver.

2.3. Efficiency analysis method

In order to quantitatively analyze the change of the SI engine efficiency, three parameters affecting the efficiency were used. Previous studied related to the energy analysis show that combustion phasing, heat loss, and pumping loss mainly affect the efficiency of the SI engine. In order to quantitatively express the change of each parameter due to the intracycle speed profile modulation, the index corresponding to each factor is described below.

2.3.1. Combustion phasing

The first is a combustion phasing. Under the given engine geometry condition, the efficiency of the Otto cycle is proportional to the compression ratio at the heat transfer timing. Considering this under SI engine conditions, the efficiency increases as combustion occurs near the TDC.

Combustion phasing has mainly been represented by CA 50 timing in previous studies [58, 59]. The closer the CA 50 timing is to TDC, the more chemical energy is converted to pressure–volume work potential through the combustion.

However, if there is speed profile modulation in the single cycle, it is difficult to compare combustion phasing using only CA 50 timing since the speed profile highly influences the crank angle–based burning rate during the combustion duration. Therefore, we used the burning rate weighted average cylinder volume during combustion to compare effective combustion phasing.

$$\bar{V}_b = \int_{t_i}^{t_f} V(t) \cdot \dot{X}_b(t)\, \mathrm{d}t \tag{2.65}$$

The reasons for introducing the above parameter are as follows. Instantaneous pressure rising situations in an IC engine are assumed. Pressure profile of original and pressure risen case are shown in Figure 2.14.

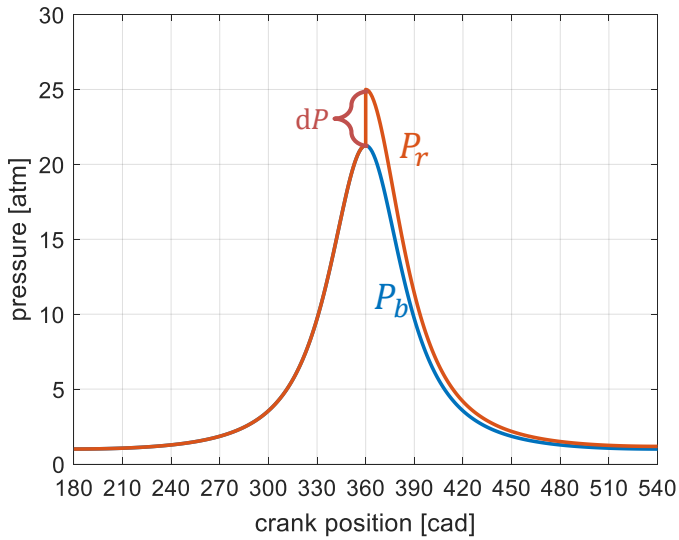

Figure 2.14 Instantaneous pressure rise

When there is an instant pressure rise, the pressure–volume work of the system is calculated as equation (2.66).

$$\delta W = \int_{V_{dp}}^{V_f} p_r dV - \int_{V_{dp}}^{V_f} p_b dV \tag{2.66}$$

p_r is the pressure profile when the pressure increases by dp, and p_b is the pressure profile when there is no instantaneous pressure change. To simplify the above equation, calorically perfect gas and isentropic process except for instant pressure rise were assumed. Under these assumptions, p_b and p_r can be written as equation (2.67) and (2.68).

$$p_b(\theta) = p_i V_i^{\gamma} \cdot V(\theta)^{-\gamma} \tag{2.67}$$

$$p_r(\theta) = \begin{cases} p_b(\theta) & , \quad \theta < \theta_{dp} \\ p_b(\theta) + dp \cdot \left(V_{dp}/V\right)^{\gamma}, & \quad \theta \geq \theta_{dp} \end{cases} \tag{2.68}$$

Substituting the above two equations into Equation (2.66) can be written as follow.

$$\begin{aligned} \delta W &= V_{dp}^{\gamma} \int_{V_{dp}}^{V_f} dp V^{-\gamma} \mathrm{d}V \\ &= V_{dp} \cdot dp \cdot \left(\frac{1 - \left(V_f/V_{dp}\right)^{-\gamma+1}}{\gamma - 1} \right) \end{aligned} \tag{2.69}$$

The instantaneous pressure rise due to combustion or heat transfer can be written as Equation (2.70).

$$dp = (\gamma - 1) \cdot dQ \; / \; V_{dp} \tag{2.70}$$

Substituting Equation (2.70) into (2.69) can be summarized as follows.

$$\frac{\delta W}{\delta Q} = 1 - \left(V_f/V_{dp}\right)^{-\gamma+1} \tag{2.71}$$

When the pressure rises due to combustion or heat transfer in a constant volume process, the simple compressible work is related to the volume at pressure change. From the first law efficiency point of view, efficiency is increased as decreasing volume at pressure change. Equation (2.68) shows that the pressure profile is a linear combination of the original pressure profile and pressure change part under the calorically perfect gas assumption. The pressure at specific timing can independently add additional terms due to the pressure rise to the original pressure profile. Therefore, for the case where the system pressure changes continuously due to combustion as in the SI engine, the above equation can be rewritten as follows.

$$\delta \mathrm{W} = \left(1 - \left(V_f/V_{dp}\right)^{-\gamma+1}\right) \delta Q \tag{2.72}$$

δQ is expressed as an expression of burn rates as follows.

$$W = Q_{LHV} \cdot \int \left(1 - \left(V_f / V_{\delta p}\right)^{-\gamma+1}\right) \mathrm{d}X_b \tag{2.73}$$

Since the typical gas mixture in the SI engine is not a calorically perfect gas, the equation cannot be summarized in this simple form, but the tendency of the relationship between efficiency and volume at pressure rise will not change. If it is not calorically perfect gas, γ changes according to the temperature and composition of the system. However, the temperature and composition of gas during the combustion process are not greatly changed in typical SI engine operation. Therefore, to make the comparison more accessible, the effect of γ is not considered. Moreover, to compare different engine conditions such as various compression ratios, the EVO timing cylinder volume is used to define the non–dimensional parameter as equation (2.74). This parameter will be referred to as an effective expansion ratio. The larger the effective expansion ratio is, the more chemical energy is converted to pressure–volume work through the combustion process.

$$ER_{EFF} = V_{EVO} \cdot \frac{1}{\int_{SOC}^{EOC} V_{cyl}(t)\dot{X}_b \mathrm{d}t} \tag{2.74}$$

2.3.2. Heat loss

The second factor is heat loss. When heat transfer occurs from a high–temperature in–cylinder gas to the cylinder wall, the in–cylinder gas pressure decreases. This effect reduces the pressure–volume work potential of the SI engine. To compare the heat loss, we used the cumulative heat transfer during the closed part of the SI engine from IVC to EVO timing divided by the lower heating value (LHV) of the in–cylinder gas at IVC timing as equation (2.76). The heat loss of the gas exchange process would have little effect on the pressure–volume work since the in–cylinder gas pressure would be adjusted through the mass transport with the manifold once heat transfer occurs in either direction

between the in–cylinder charge and the cylinder wall. It is confirmed simulation with varying heat transfer coefficient. The heat transfer coefficient during the gas exchange process is changed with the scaling factor. The heat transfer scaling factor is used for calculating the heat transfer rate as follows.

$$\dot{Q} = HTSF \cdot h \cdot A \cdot \left(T_{gas} - T_{wall}\right) \tag{2.75}$$

To investigate the effect of heat transfer during the gas exchange process on the efficiency, simulations were conducted with changing the HTSF from zero to three. Pressure profiles during the gas exchange process are shown in Figure 2.15.

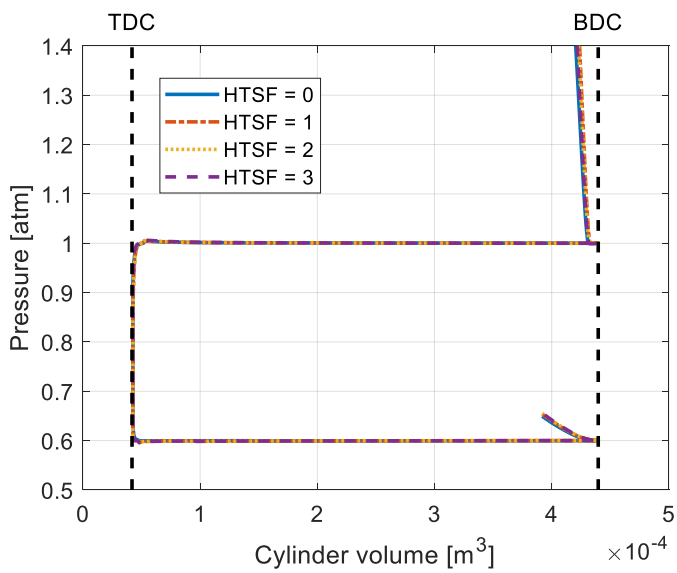

Figure 2.15 Effect of the gas exchange process heat transfer on the in–cylinder pressure

The pressure profile is not affected by the heat transfer rate during the gas exchange process. In–cylinder pressure can be changed by mass transfer between the manifold and cylinder. Thus in–cylinder pressure is in equilibrium with manifold pressure. Pressure–volume work and heat loss during the gas exchange process are compared in Figure 2.16.

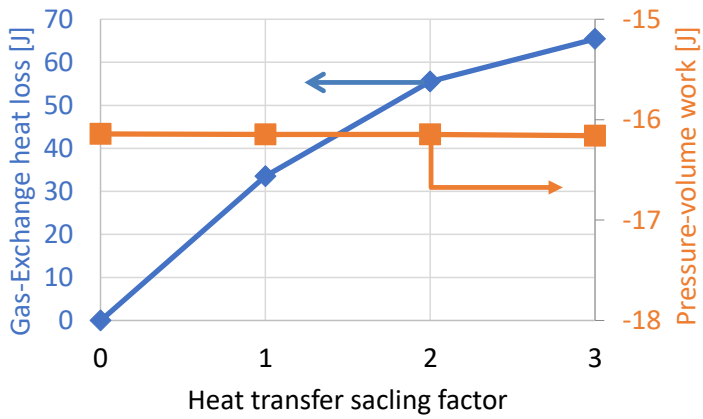

Figure 2.16 Comparing between the heat loss and pV work

Changing the heat transfer rate only affects the heat loss. Substantial heat loss during the gas exchange process cannot reduce the pressure–volume work of the SI engine. Therefore, only heat transfer during the closed part of the cycle was considered and normalized to LHV.

$$HL = \frac{\int_{IVC}^{EVO} \dot{Q}(t)dt}{LHV_{IVC}} \tag{2.76}$$

2.3.3. Pumping work

The last factor is pumping work. Pumping work is analyzed using work between the exhaust BDC timing and intake BDC timing in many studies [60, 61]. However, a typical engine EVO and IVC timing are not located at the BDC. It is appropriate to compare the pressure–volume work during the open system part of the SI engine from EVO to IVC since the in–cylinder pressure from EVO to BDC and from BDC to IVC is affected by the speed profile modulation. To confirm this effect, pressure profiles with different speed profile during the gas exchange process are compared. In Figure 2.17, four different

speed profiles are shown. The speed profile from the EVO timing to the BDC timing is changed.

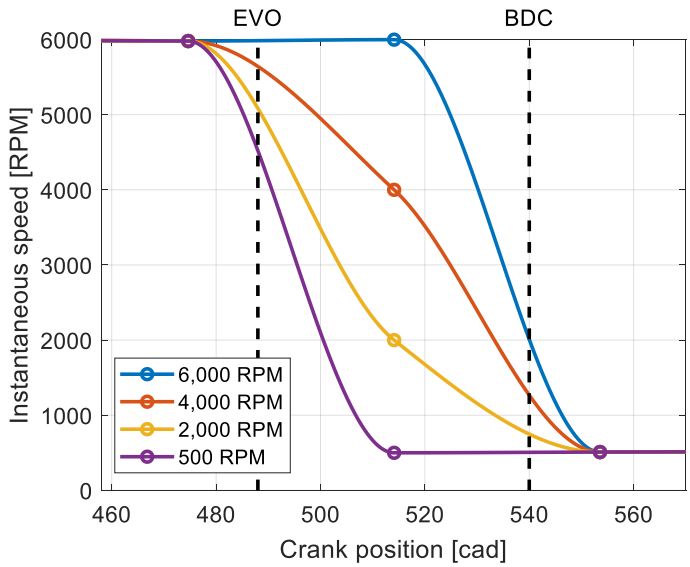

Figure 2.17 Speed profile modulation

The speed profile changing effect on the pressure profile near the valve timing is shown in Figure 2.18. If speed near the valve timing increases, in–cylinder pressure between EVO and BDC rises. Finite–time is required to reach the pressure equilibrium between cylinder and manifold.

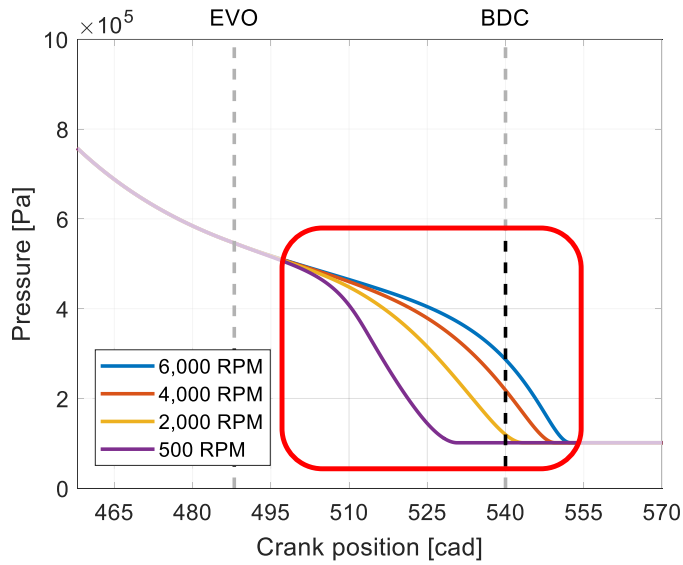

Figure 2.18 In–cylinder pressure change as modulating the speed profile

Therefore, pumping work is calculated using the total pressure during the gas exchange process. The pumping work efficiency is defined as the pumping work divided by the LHV of the in–cylinder gas at IVC timing, as shown in equation (2.77).

$$\eta_p = \frac{\int_{EVO}^{IVC} p\dot{V}\,\mathrm{d}t}{LHV_{IVC}} \tag{2.77}$$

Chapter 3. Optimization results and analysis

The specifications of the SI engine used in this study are as follows.

Table 3.1 SI engine simulation condition

Bore (mm)	77
Stroke (mm)	85.44
Compression ratio (–)	10.5
Intake Valve Open timing (cad)	bTDC 16
Intake Valve Close timing (cad)	aBDC 48
Exhaust Valve Open timing (cad)	bBDC 52
Exhaust Valve Close timing (cad)	aTDC 12
Intake Valve Diameter (mm)	29
Exhaust Valve Diameter (mm)	27
Fuel injection type	Port fuel injection

The displacement volume is about 400 cc and the fresh mixture enters the cylinder after mixing with fuel and air. The octane number of the fuel assumed 87 based on an anti–knock index.

3.1. Conventional engine operation

Simulations under the conventional operating condition were performed, and net indicated efficiency was calculated. Exhaust manifold pressure is fixed at 1 atm and then calculated net indicated efficiency with varying intake manifold pressure and average engine speed. Intake manifold pressure conditions were [0.4, 0.6, 0.8, 1.0] atm, and the mean engine speed conditions were [1,000, 2,000, 3,000, 4,000, 5,000] RPM. Figure 3.1

shows the net indicated efficiency, and the red circle marker is the point where the simulations were performed.

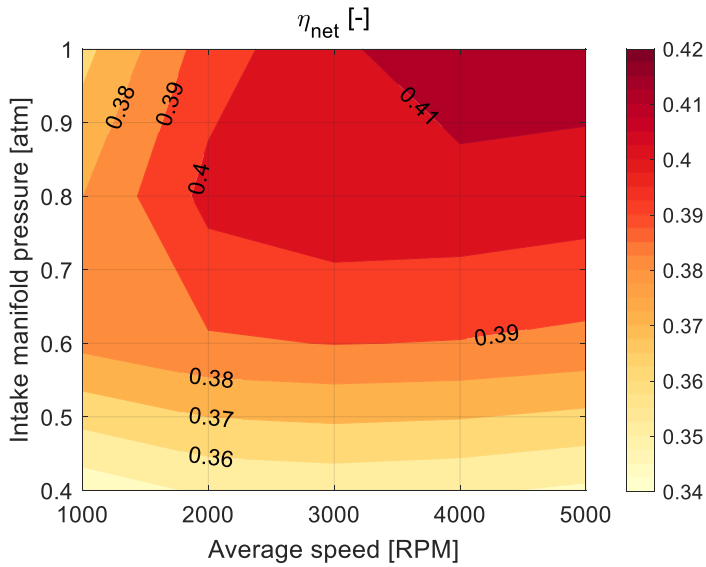

Figure 3.1 Efficiency map under the conventional operating condition

Simulation results have a trend like the typical SI engine indicated efficiency. In high intake manifold pressure and low–speed condition, efficiency is decreased by retarding the spark timing to mitigate knocking. This can be quickly confirmed by examining the CA 50 timing. CA 50 timing is retarded in the high intake manifold pressure and low–speed condition compared to other operating conditions. Retarded CA 50 timing is a result of retarding the spark timing for knock mitigation.

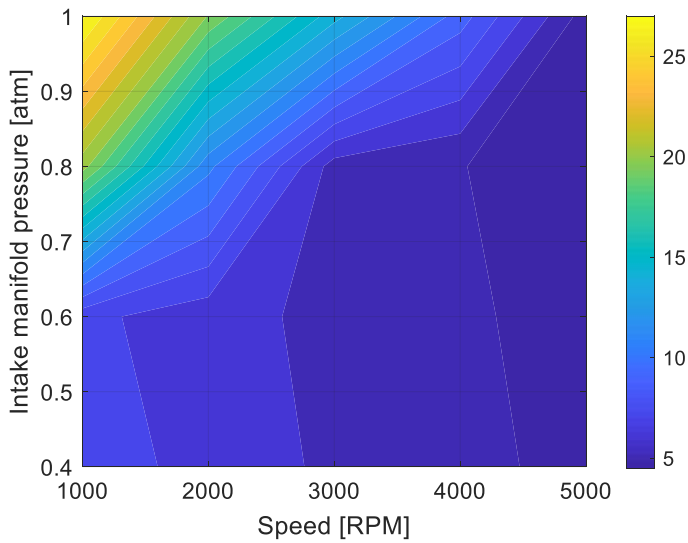

Figure 3.2 CA 50 timing map of conventional operation

Therefore, in the high intake manifold pressure conditions, the efficiency is high in the high–speed condition. In the low intake manifold pressure condition that is not affected by knocking, the efficiency is the highest at about 3,000 RPM. Heat loss increases as the engine speed decreasing, and pumping loss increases as the engine speed increases. The maximum efficiency operating condition is a result of optimizing these trade–off related losses. Based on these factors, the SI engine model used in this study can reflect the characteristics of the SI engine operation.

3.2. Unconstrained optimization

Problem
find $N(\theta)$ and θ_{sp} such that,
$$\text{maximize}\ \eta_{net}$$
subject to,
$$N(\theta) \in \mathbb{C}^1$$
$$N_{lb} \leq N(\theta) \leq N_{ub}$$
$$\left|1 - \eta_{net,k}/\eta_{net,k+1}\right| \leq 5 \cdot 10^{-5}$$

First, an unconstrained intracycle speed profile optimization problem was solved. An unconstrained optimization problem means that an unburned mixture does not auto–ignite, for example, high octane–number fuel, and there is no average speed constraint. Only the upper and lower bound of the control variable (instantaneous speed) are considered. The optimal speed profile, in this case, is shown in Figure 3.3.

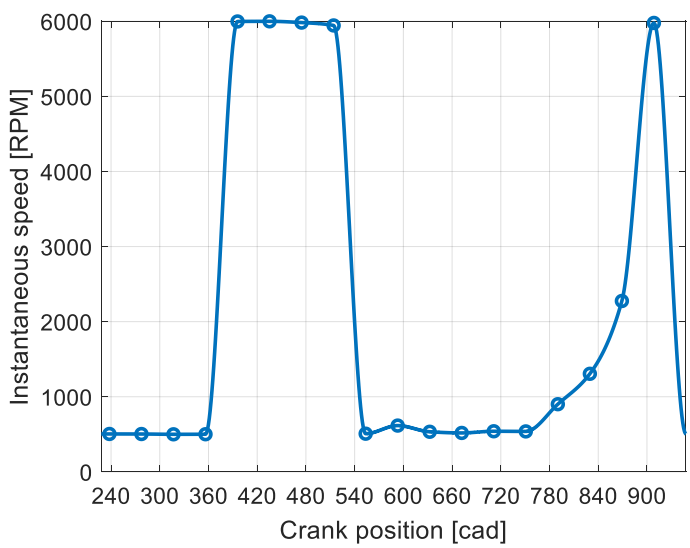

Figure 3.3 Optimal speed profile of knock unconstrained condition

We divided the optimal speed profile into compression, expansion, exhaust, and gas exchange processes to see how the speed profile of each process influences the SI engine net indicated efficiency.

3.2.1. Compression process

The optimal speed profile during the compression process is lower bound of speed. The speed of the compression process is varied, as shown in Figure 3.4, and the changes in efficiency and performance parameters were calculated using the modulated speed profile.

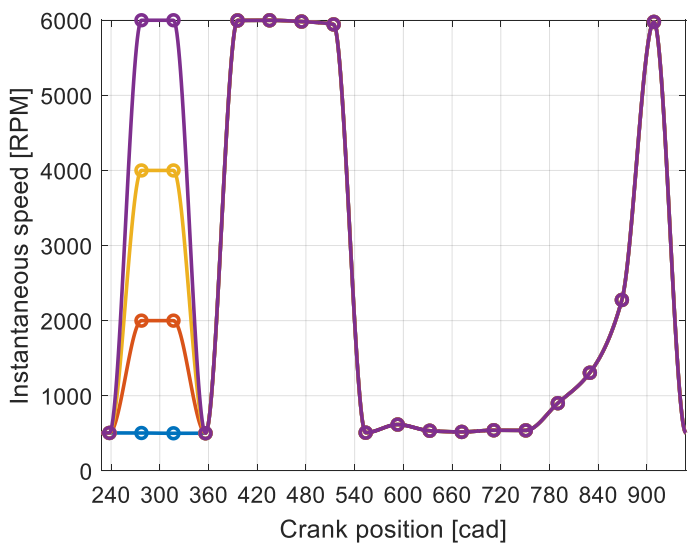

Figure 3.4 Compression process speed profile modulation

The efficiency and performance parameters changed, as shown in Figure 3.5 when the simulation was performed with varying compression process speed. The speed profile of the compression process mainly affects combustion phasing and heat loss and has a relatively small impact on pumping work.

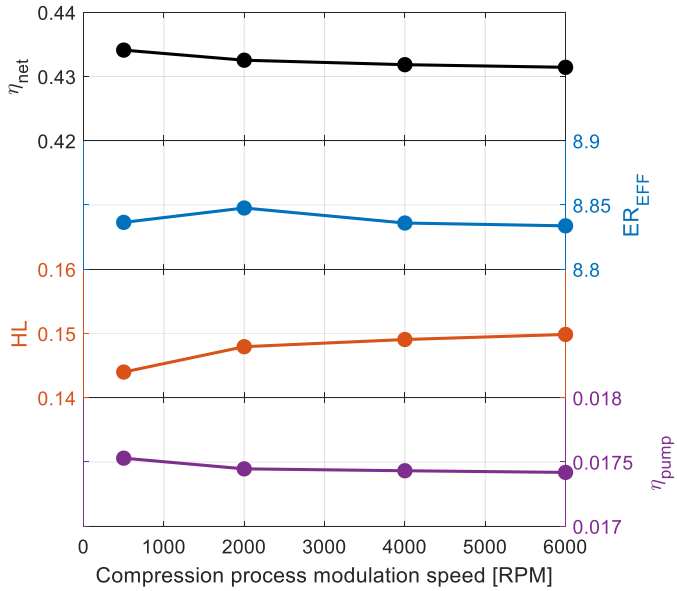

Figure 3.5 Sensitivity analysis results of the compression process

The speed profile of the compression process affects combustion phasing and heat loss because the turbulence intensity is affected by the speed profile of the compression process, as shown in Figure 3.6.

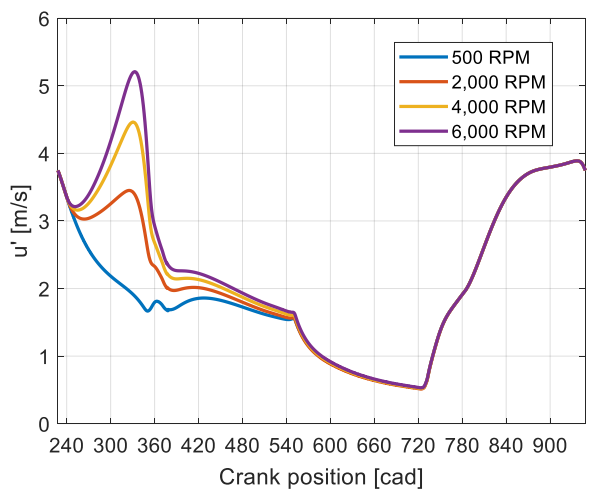

Figure 3.6 Effect of the compression speed on the turbulence intensity

According to Equation (2.22) and (2.23), the turbulent flame speed becomes faster as turbulence intensity increases. Therefore, it is possible to reduce time–based combustion duration, which has the advantage that it can be advantageous for combustion phasing.

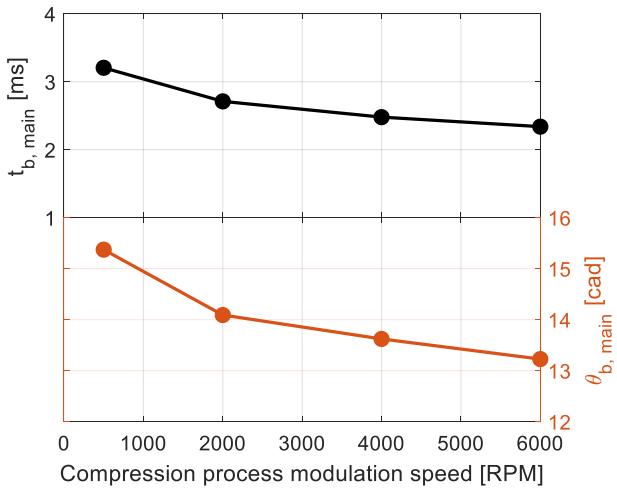

Figure 3.7 Effect on main burn duration

Also, increasing the turbulence intensity increases the characteristic speed of the in–cylinder gas. It leads to an increase in the convective heat transfer coefficient. Therefore, the heat transfer rate increases during the expansion process.

According to the literature, cad–based combustion duration is increased in high engine speed conditions. Therefore, in the knock unconstrained condition, it is possible to reduce the cad–based combustion duration by lowering the engine speed so that the speed profile in the direction of reducing heat loss during the expansion process can be considered as the optimized speed profile.

3.2.2. Expansion process

A sensitivity analysis of the speed profile of the expansion process was performed. Similar to the compression process, the simulations were performed with varying speed profiles during the expansion process, as shown in Figure 3.8. If the speed profile of the expansion process is changed, speed around the fTDC and EVO timing changes due to the interpolating function characteristics.

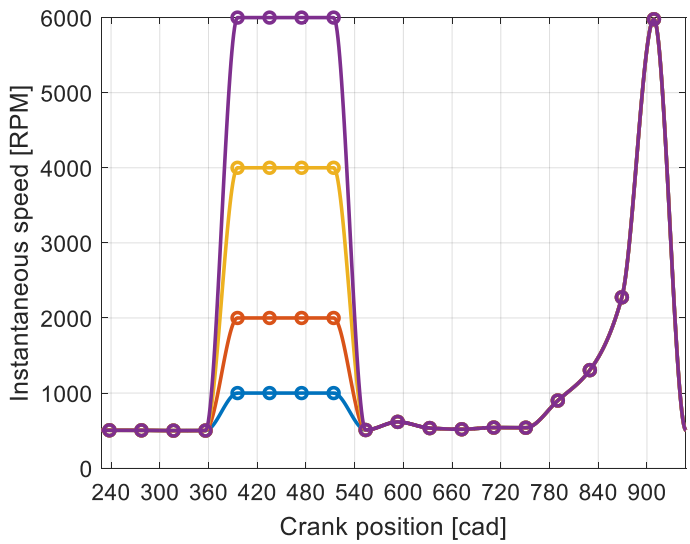

Figure 3.8 Expansion process speed profile modulation

Sensitivity analysis of efficiency and performance parameters were performed, as shown in Figure 3.9. Sensitivity analysis shows that the heat loss is a significant influence on the speed profile of the expansion process. First, the effect on combustion phasing was examined. In knock unconstrained conditions, combustion phasing is mainly affected by combustion duration. The factor influencing the duration of combustion is the turbulence intensity during the combustion process. Figure 3.10 shows how the turbulence intensity of the unburned zone changes like the expansion process speed profile changes.

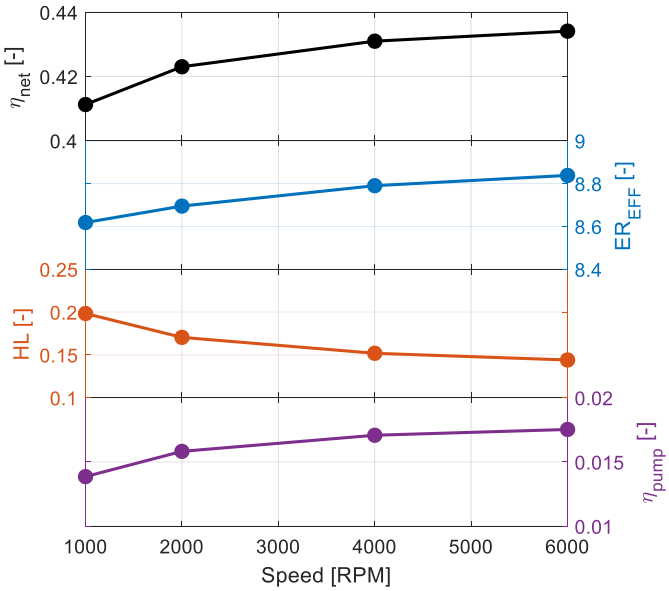

Figure 3.9 Sensitivity analysis results of the expansion process

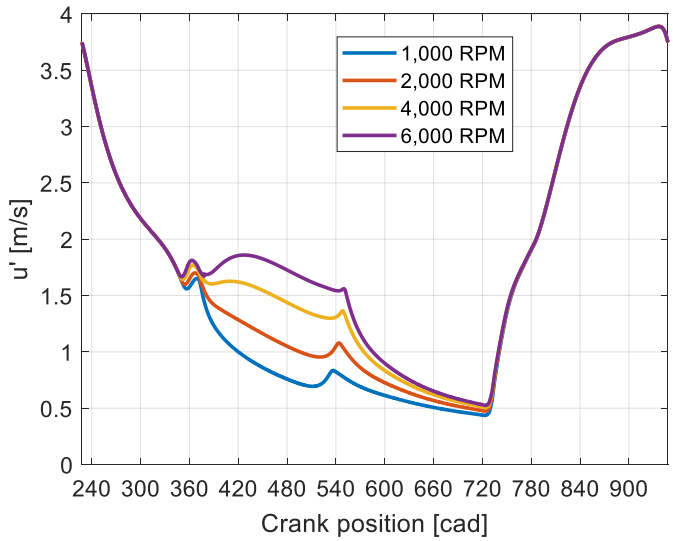

Figure 3.10 Effect of the expansion process speed on the turbulence intensity

The turbulence intensity change is small during the compression and combustion duration. As can be seen in Figure 3.11, the effect of the expansion process speed profile on the main burn duration is minimal.

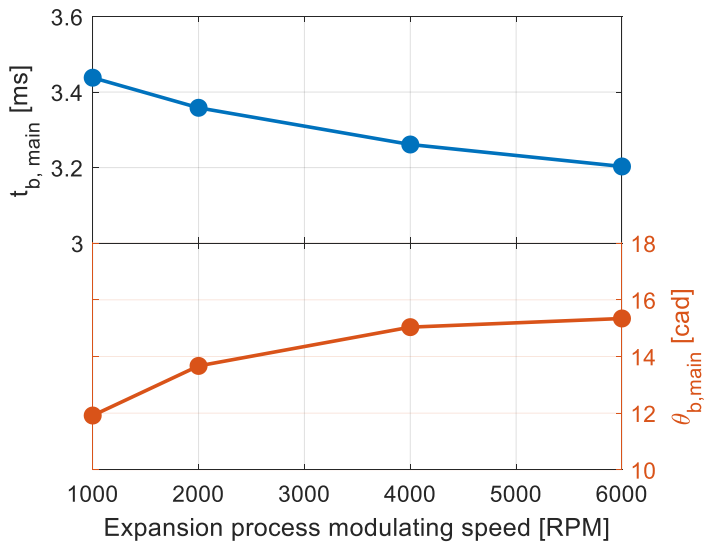

Figure 3.11 Effect of expansion process speed profile on the burn duration

The engine speed of the expansion process affects the convective heat transfer coefficient and the time duration of heat transfer. As the engine speed increases, the characteristic speed increases, and the convective heat transfer coefficient increases. However, since the heat transfer coefficient increases in proportion to speed to the power of 0.8, the time duration reducing effect is greater. The fast engine speed of the expansion process reduces engine heat loss.

The pumping efficiency is also affected by the expansion process speed profile. This is because of the in–cylinder pressure at EVO timing changes. As the heat loss decreases, the pressure drop during the expansion process is reduced. Therefore, the EVO timing

pressure increases, as shown in Figure x. The speed profile of the expansion process affects the pressure of the EVO timing, which affects the pumping efficiency.

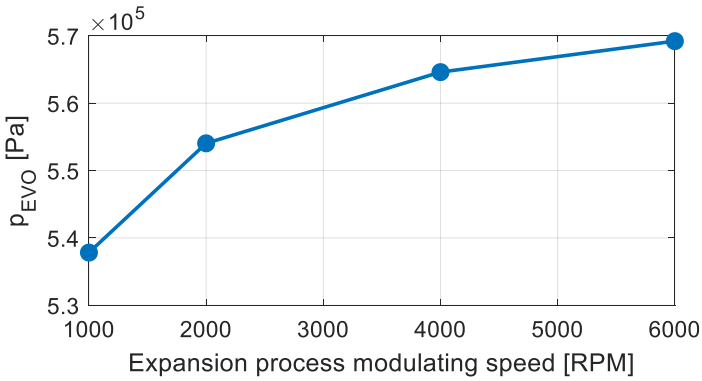

Figure 3.12 Effect of expansion process speed on the pressure at EVO timing

3.2.3. Gas exchange process

- Exhaust process

The effect of exhaust process speed profile on the in–cylinder turbulence intensity is shown in Figure 3.13. Exhaust process speed profile does not affect the turbulence intensity from the IVC timing to the EVO timing. Therefore, the speed profile of the exhaust process does not affect combustion phasing or heat loss.

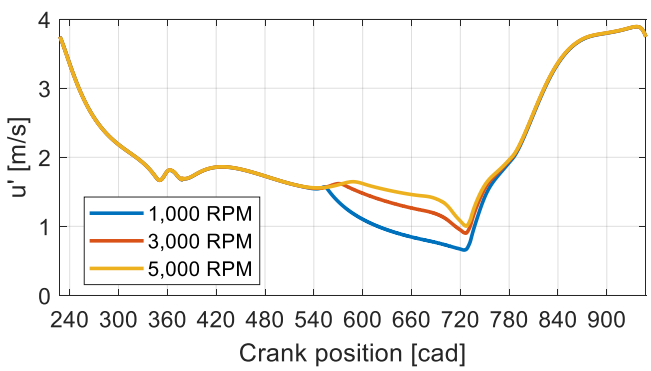

Figure 3.13 Turbulence intensity changing by modulating exhaust process speed

Thus, the speed profile of the exhaust process is optimized to maximize the pumping work. As the exhaust process speeds up, the time duration for exhausting decreases, resulting in a retarded pressure equilibrium between the cylinder and the exhaust manifold. The pumping efficiency deteriorates as the exhaust process speeds up.

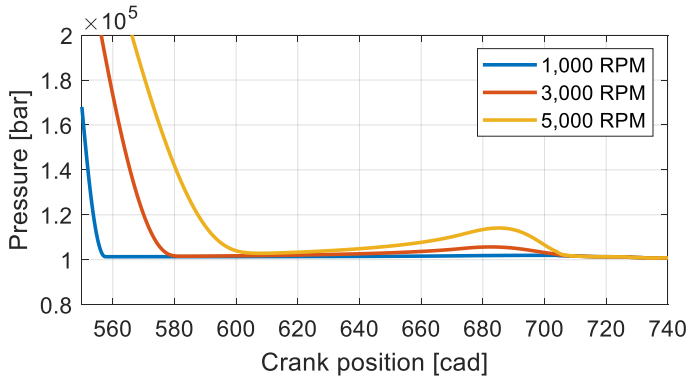

Figure 3.14 Exhaust process pressure with various speeds of the exhaust process

- Intake process

A sensitivity analysis was performed with varying the speed of the intake process. Combustion phasing, heat loss, and pumping efficiency are all affected by the intake process speed profile.

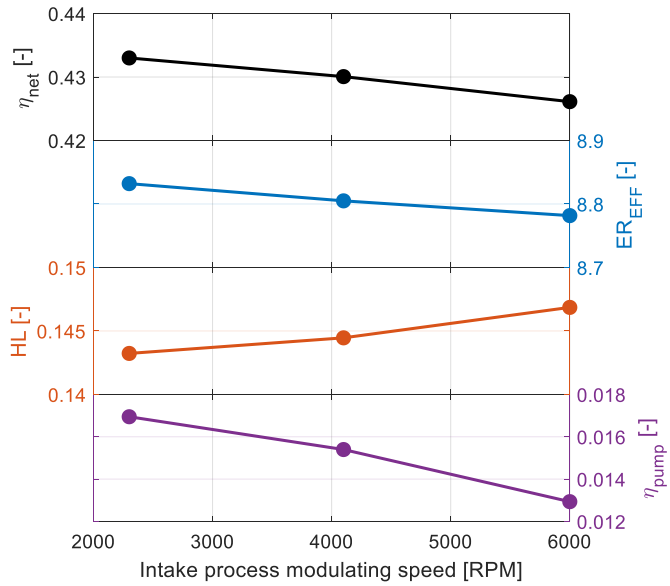

Figure 3.15 Sensitivity analysis results of the intake process

As the intake process speed increases, the in–cylinder turbulence intensity increases, it leads to reduce the burn duration, as shown in Figure 3.16. The combustion phasing can be improved by reducing the burn duration, but heat loss can increase due to increased characteristic speed. Therefore, the spark timing is retarded to optimize combustion phasing and heat loss, resulting in worse combustion phasing when the intake process is faster.

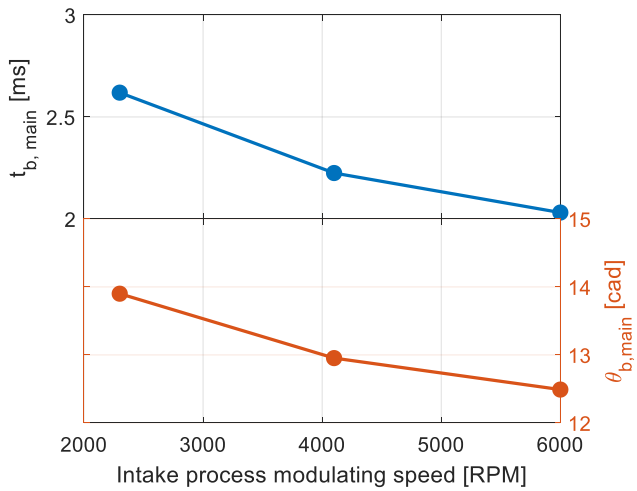

Figure 3.16 Effect of intake process speed on the burn duration

In addition to the decrease in gross efficiency, the work of the gas exchange process is also reduced. The pressure equilibrium timing between the cylinder and the intake manifold is retarded when intake process speed increases. Therefore, pumping work is deteriorated by increasing the intake process speed as the same as the exhaust process.

3.3. Knock constrained optimization

Problem

find $N(\theta)$ and θ_{sp} such that,

$$\text{maximize}\ \eta_{net}$$

subject to,

$$N(\theta) \in \mathbb{C}^1$$

$$N_{lb} \leq N(\theta) \leq N_{ub}$$

$$UMF_{@LW=1} \leq UMF_c$$

$$\left|1 - \eta_{net,k}/\eta_{net,k+1}\right| \leq 5 \cdot 10^{-5}$$

In a conventional SI engine, knocking occurs when operating in the high load condition. This is caused by the auto–ignition of the unburned mixture before the flame reaches. Knocking can damage the engine, so in conventional SI engines, spark timing is retarded to mitigate knocking. The spark timing cannot be operated at MBT timing and retarded, resulting in deterioration of combustion phasing and less efficiency in the knock–limited operating condition. Thus, the effect of intracycle speed profile modulation on the SI engine operation is investigated in the knock limited operating condition.

The fuel octane number for the knock modeling was that of regular gasoline in the gas station. Intake manifold pressure was assumed to be a wide–open throttle condition. In order to operate the engine in a high efficiency operating condition in the series HEV, the WOT condition that has small pumping loss is chosen as the operating condition for

optimization. When the engine speed profile was optimized under these conditions, the following results were obtained.

Figure 3.17 shows the optimal speed profiles of the unconstrained case and the knock constrained case at the same time. Figure 3.17 shows the significant difference in the speed profile during the compression process and the intake process. As expected in section 3.1, the speed profile of the expansion and exhaust processes does not affect the knocking, but the speed profile of the intake and compression processes can be affected. In the case of unconstrained optimization, the speed profile of the compression process is designed to minimize heat loss during the expansion process. The speed profile of the intake process also affects the turbulent intensity during the combustion process, so it can be expected to change in the direction of increasing the turbulent intensity. Therefore, in this section, how the speed profile of each interval affects the SI engine efficiency and performance parameters.

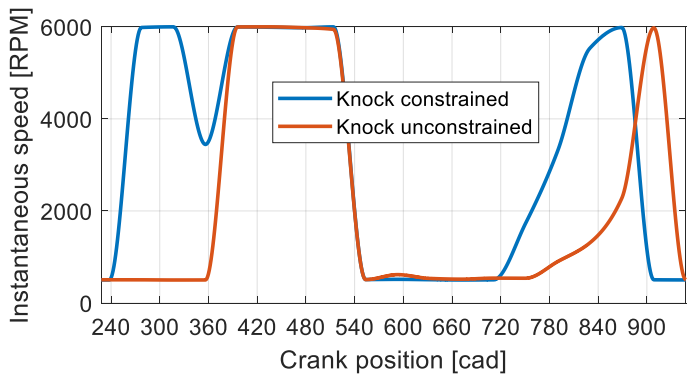

Figure 3.17 Optimal speed profile change due to knock constrained

3.3.1. Compression process (Interval–I and II)

As shown in Figure 3.18, the optimal speed profile demonstrates several characteristic intervals with changing speeds. In understanding the sensitivity and effect

of the speed modulation during the certain interval, we changed the speed of the designated interval to 500, 2,000, 4,000 and 6,000 RPM, while the speeds of the other intervals were kept constant, and the optimal spark timing was newly found to maximize the efficiency under the knock limit.

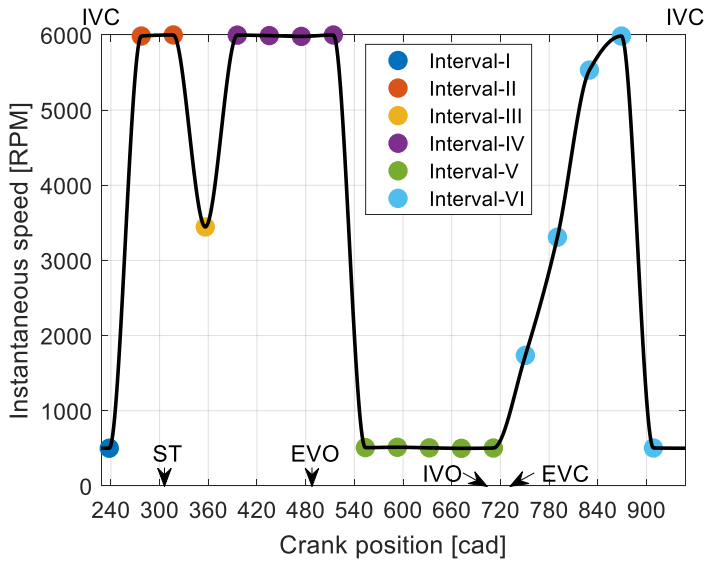

Figure 3.18 Knock constrained optimal speed profile

The compression process was divided into two intervals. First, Interval–I is around the IVC timing, or near the compression start, while Interval–II is during the major compression stroke. Figure 3.19 shows how we change the speed profile only in Interval–I as an example. In the graph, the first two points correspond to Interval–I, and the optimized speed was 500 RPM, as shown in Figure 3.18. Then, we change the speed on those two points over the range mentioned above, while the interpolating function between the intervals is changed accordingly.

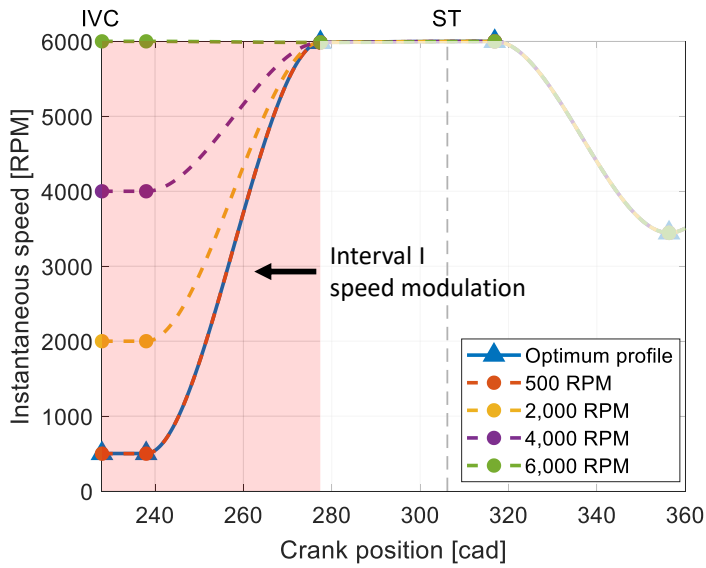

Figure 3.19 Interval–I speed profile modulation for sensitivity analysis

Simulation results are summarized in Figure 3.20. Decreasing the Interval–I speed increases the net indicated efficiency. As the Interval–I speed slows down, the effective expansion ratio increases, and the heat loss and pumping efficiency are deteriorated. It is clear that the effective expansion ratio has the greatest effect on the net indicated efficiency under the Interval–I speed modulation condition, over such counter–effects by the other factors.

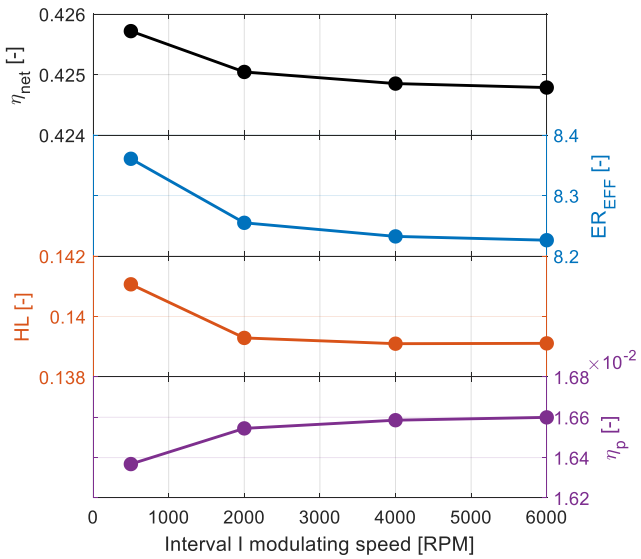

Figure 3.20 Interval–I sensitivity analysis results

The main reason that the speed profile of Interval I affects the effective expansion ratio is that the pressure at IVC timing is affected by the Interval–I speed profile, as shown in Figure 3.21. The Interval–I speed affects the in–cylinder pressure from BDC to IVC timing. As the speed increases from BDC to IVC timing, the IVC pressure increases because of the difference between the in–cylinder volume change rate due to the piston movement and the volume flow rate of the outward gas through the valve increases. In the unconstrained case without knock consideration, the effective expansion ratio is rarely affected by changing the speed during Interval 1, but the remaining UMF increases at the knock onset, leading to stronger knock intensity, which is mainly from the increased IVC pressure with higher speed operation during Interval 1. Therefore, the interval–I speed is optimized to be low–speed.

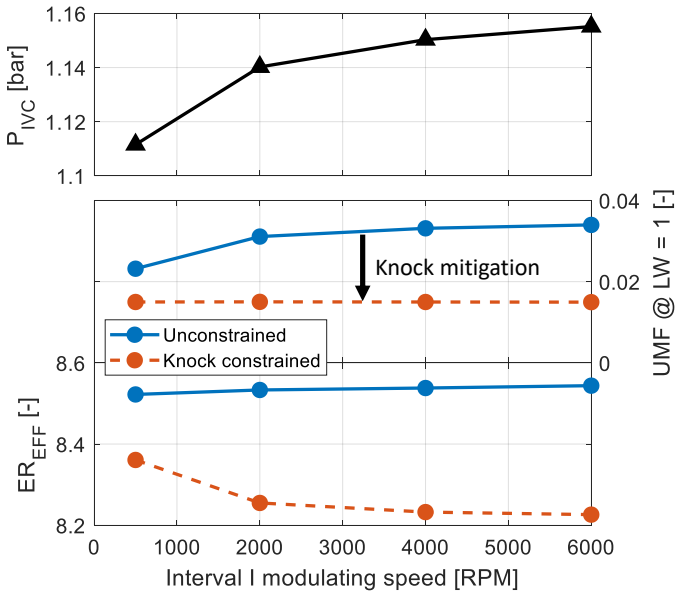

Figure 3.21 Interval–I speed effect on IVC pressure and knocking

Next, the speed profile during Interval II was investigated. Again, the simulation was performed by varying the Interval–II speed between 500 and 6,000 RPM. Figure 3.22 shows the performance parameters according to the variation. As the Interval–II speed increases, the net indicated efficiency increases. As similar as in Interval–I, the heat loss and pumping work would rather decrease the net indicated efficiency as the speed increases, and thus, the net indicated efficiency increases due to the improvement of the effective expansion ratio. The effective expansion ratio is influenced by the interval–II speed mainly because the turbulent flame speed of the combustion process changes, as discussed in the following paragraphs.

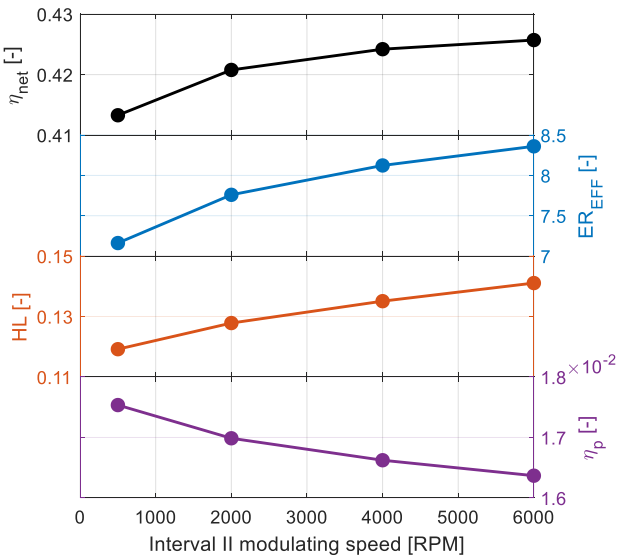

Figure 3.22 Interval–II sensitivity analysis results

The turbulent flame speed is directly correlated to the burn duration. As summarized in Figure 3.23, as the interval–II speed increases, the time–based main burn duration (10–90%) decreases due to the increased TKE during the combustion process. Equation (2.48) shows that TKE production increases as the density change rate increases. In the unconstrained case without knock consideration, the remaining UMF at the autoignition of the unburned mixture decreases with the decrease of the main burn duration at a higher interval–II speed. This decrease reflects on, for the knock–constrained case, an increase of the effective expansion ratio as the interval–II speed increases, mainly due to the two following reasons. First, the shortened burn duration leads to the nearer constant–volume combustion. Second, the faster burn enables advanced combustion timing closer to TDC due to better knock robustness.

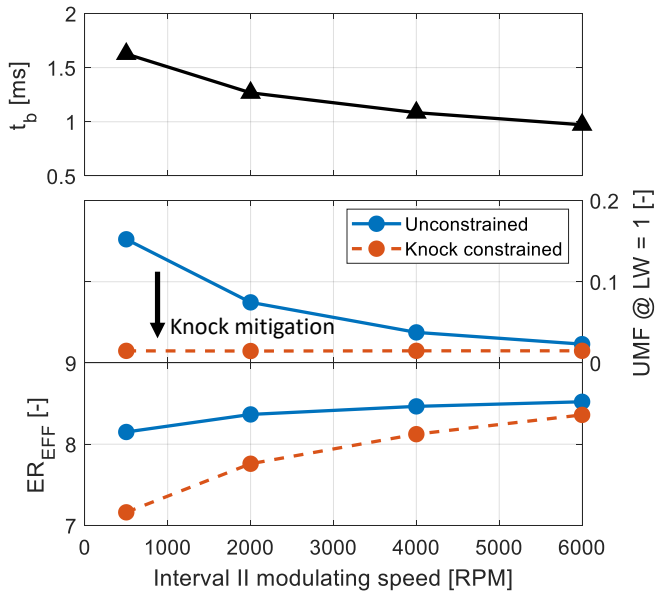

Figure 3.23 Interval–II speed effect on burn duration and knocking

3.3.2. Expansion process (Interval–III and IV)

The interval–III speed profile mainly affects the combustion phasing. In the optimized profile, interval III is operated at speed slightly slower than the upper bound speed. The sensitivity analysis results are shown in Figure 3.24. As in Interval–I and Interval–II, the efficiency is mainly affected by the effective expansion ratio. The heat loss and pumping work were improved when the interval–III speed was low.

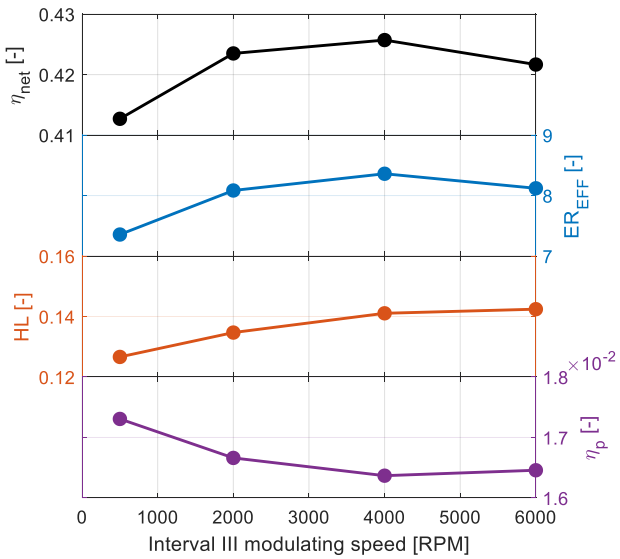

Figure 3.24 Interval–III sensitivity analysis results

If the Interval–III speed profile is varied, the turbulent intensity during the combustion duration is varied. Analysis results show that increasing the interval–III speed reduces the time–based main burn duration, as shown in Figure 3.25. The time–based main burn duration affects the knocking related to the auto–ignition of the unburned mixture, while the cad–based main burn duration affects the effective expansion ratio related to the cylinder volume during the combustion process. Expectedly, as the time–based burn duration decreases, the remaining UMF when auto–ignition occurs decreases. Reduction of the effective expansion ratio to mitigate knocking decreases under the high Interval–III speed condition. However, the cad–based main burn duration increases if the interval–III speed is higher than 2,000 RPM because speed increasing effect is higher than time–based burn duration decreasing effect. As the cad–based burn duration becomes longer, the effective expansion ratio decreases, even if the time–based burn duration decreases. Therefore, these two effects counteract each other, and thus, the

effective expansion ratio in the knock–constrained case is maximized at 4,000 RPM, as shown in Figure 3.25.

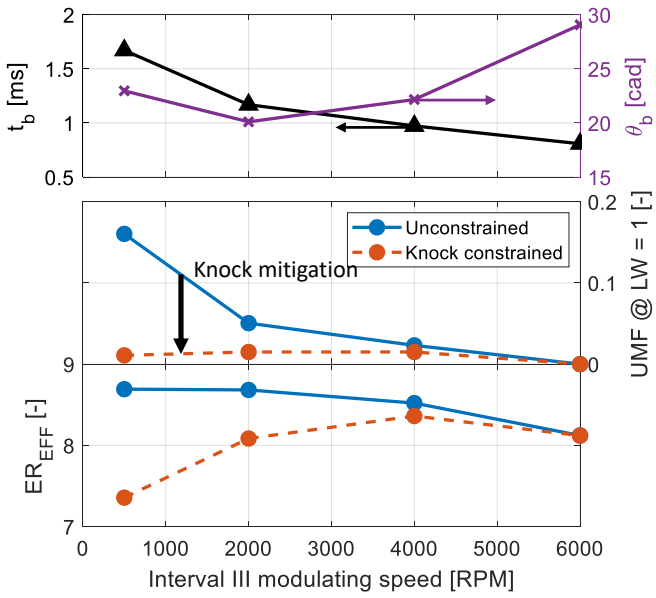

Figure 3.25 Interval–III effect on burn duration and knocking

We examined the effect of changing the Interval–IV speed on efficiency, as shown in Figure 3.26. As the speed of Interval IV increases, the effective expansion ratio, heat loss, and pumping work are all improved. In particular, the effect of the speed profile modulation on heat loss is larger than that for the other intervals.

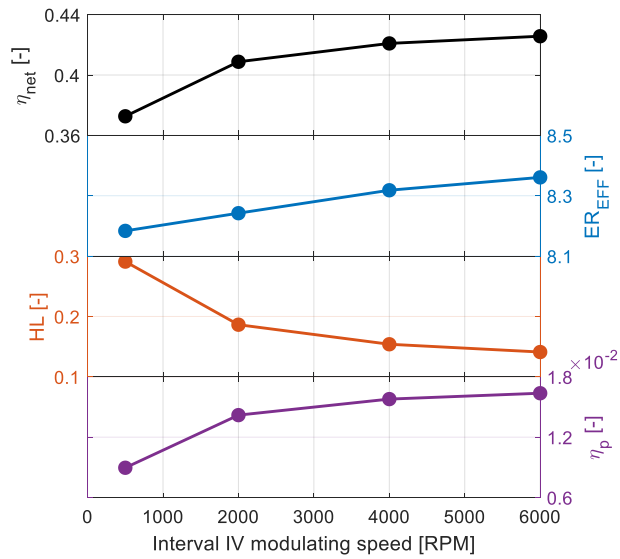

Figure 3.26 Interval–IV sensitivity analysis results

We investigate which of the three factors mainly influences efficiency. Because the difference between the maximum and minimum of the pumping work efficiency is approximately 0.01, which has the same denominator with the heat transfer, it cannot be regarded as a major factor affecting the net indicated efficiency. Therefore, we examined which one of heat loss or combustion phasing had a larger effect on efficiency in the following paragraph.

As depicted in Figure 3.27, the unconstrained–case simulation results show that the efficiency decreases even though the effective expansion ratio increases when the interval–IV speed is low, which implies that the effective expansion ratio is not a major factor that affects the efficiency trend. Rather, the net indicated efficiency for both unconstrained and knock–constrained cases is mainly affected by heat loss during the expansion process as the Interval–IV speed varies. As the Interval–IV speed increases, the heat loss clearly decreases because the decrease in the heat transfer time has a greater

effect than the possible increase of the convective heat transfer coefficient with the increased piston speed. This tendency can also be found in previous studies [30, 31].

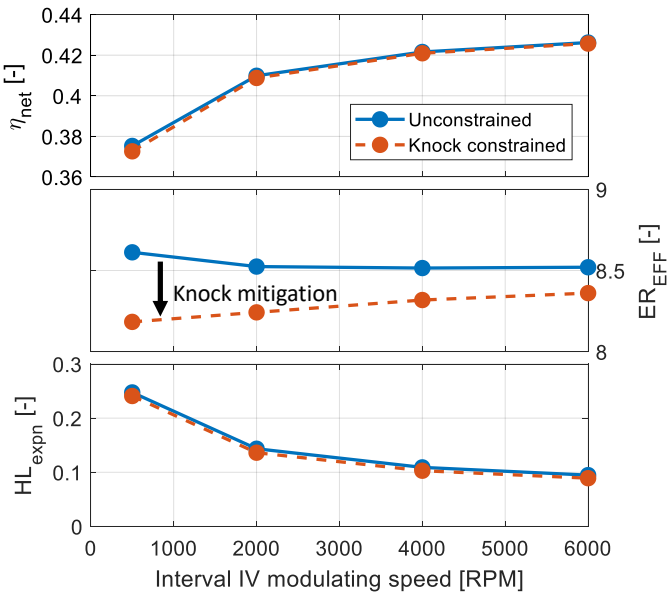

Figure 3.27 Interval–IV effect on heat loss and knocking

3.3.3. Gas exchange process (Interval–V and VI)

The gas exchange process is divided into an exhaust process (Interval V) and an intake process (Interval VI). The speed during interval V mainly affects the pumping work, as shown in Figure 3.28. If the exhaust process speed increases, the pumping loss increases because the cylinder volume change rate is faster than the volume flow rate from the cylinder to the manifold, which is more explained below. The effective expansion ratio and heat loss are barely affected by the speed change of interval V.

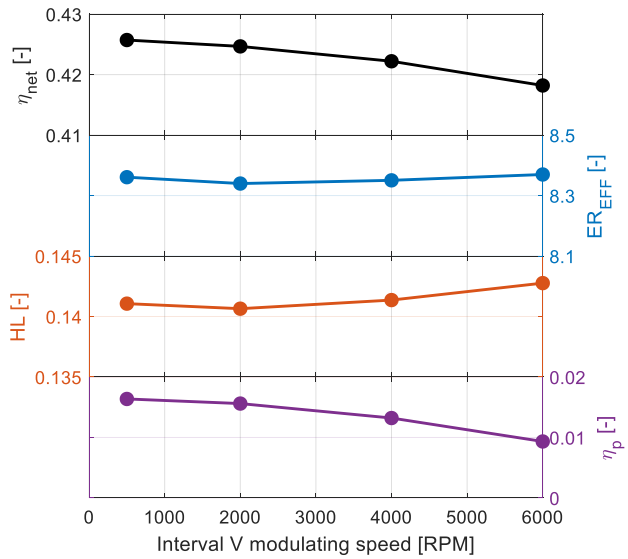

Figure 3.28 Interval–V sensitivity analysis results

The change in pumping efficiency can be explained by observing the pressure profile during the exhaust process. When the gas is exhausted from the cylinder to the manifold for pressure equilibrium, a finite time is required. Therefore, as the engine speed increases, the CAD–based duration increases until the equilibrium is reached. As shown in Figure 3.29, at the beginning of the exhaust process, the blow–down process takes longer in crank angles with higher speed, which raises overall in–cylinder pressure near BDC. Additionally, as the piston moves to the TDC, the in–cylinder pressure rises near TDC, because the in–cylinder gas does not exhaust as much as the volume change rate due to fast piston movement. Therefore, the pumping efficiency is high under slow Interval–V speed conditions.

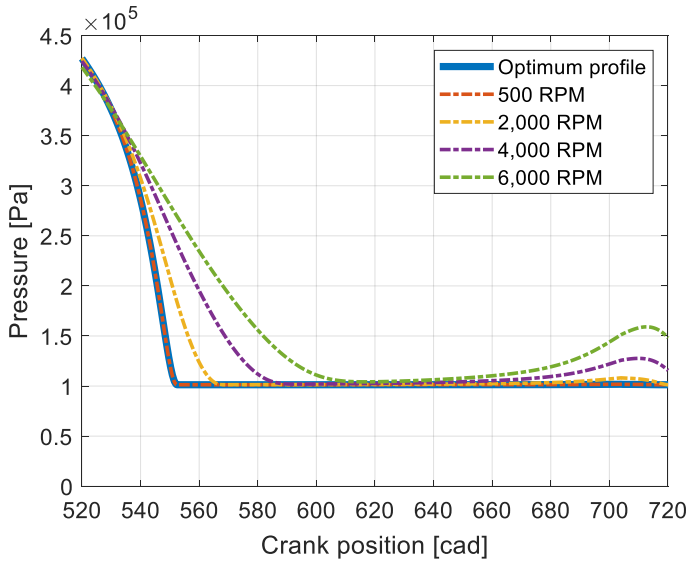

Figure 3.29 Interval–V speed profile effect on the exhaust process pressure profile

Finally, the Interval–VI speed profile is analyzed. Simulation results with changing intake process speed profiles are shown in Figure 3.30. If the Interval–VI speed is lower than 1,200 RPM, the fresh mixture cannot be burned until the EVO timing due to the decreased turbulent flame speed. Thus, only the results with 1,200 RPM or higher are compared. It is found that the speed during the intake process can significantly affect the combustion phasing, heat loss, and pumping loss altogether. As the piston speed changes during the intake process, the induced in–cylinder kinetic energy is affected. Then, this alteration in the flow characteristics affects both the turbulent flame speed and convective heat transfer coefficient. In addition, similarly to the exhaust process, if the piston moves faster than the rate at which the gas enters the cylinder from the manifold, the cylinder pressure will be lower than the manifold pressure, and the pumping loss will increase. As the Interval–VI speed increases, the effective expansion ratio improves, but both the heat loss and pumping work worsen.

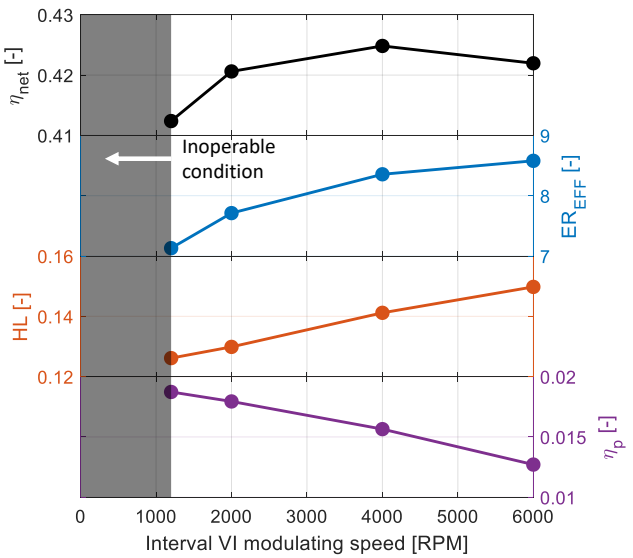

Figure 3.30 Interval–VI sensitivity analysis results

The reason for the effective expansion ratio improvement with higher speed is the reduction in the burn duration due to the increase of the turbulent flame speed. When the engine speed is high in the intake process, the MKE and TKE of the inward gas through the valve increase, such that the TKE increases during the combustion process, and the turbulent flame speed increases. In the meantime, the heat loss increases due to two effects: 1) the convective heat transfer coefficient increases with overall higher flow speed, and 2) the duration for heat transfer from high–temperature burned gas to the cylinder wall increases as the end of combustion timing is advanced. Finally, as mentioned earlier, the pumping efficiency deteriorates with faster interval speed because of the speed difference between the cylinder volume change rate by piston movement and volume flow rate of intake gas from the manifold to the cylinder. As a result, there is a trade–off among these factors, resulting in the highest efficiency of near 4,000 RPM. In Figure 3.31, it is noted that, above 4,000 RPM, the effective expansion ratio is not significantly affected by knock mitigation, which implies that even faster interval speed would not add to the efficiency

gain due to there already being a sufficiently fast combustion duration. This, in combination with the ever–increasing pumping loss and heat loss with the interval speed, leads to the maximum net indicated efficiency of approximately 4,000 RPM.

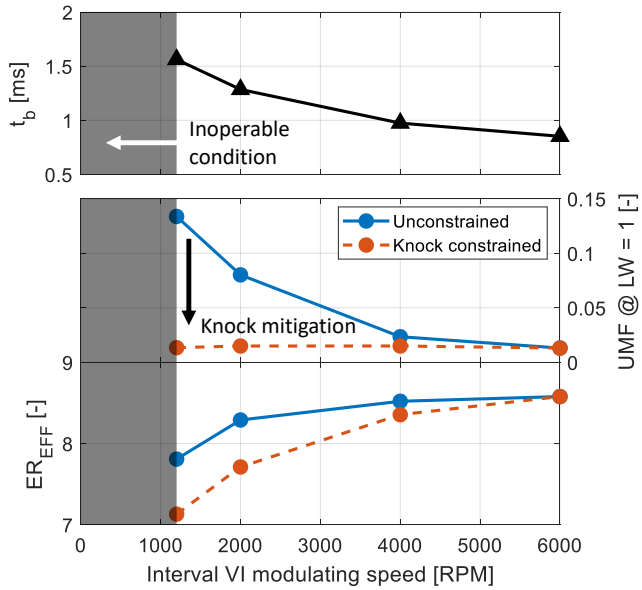

Figure 3.31 Interval–VI effect on burn duration and knocking

3.4. Average speed constrained optimization

Problem

find $N(\theta)$ and θ_{sp} such that,

$$\text{maximize } \eta_{net}$$

subject to,

$$N(\theta) \in \mathbb{C}^1$$

$$N_{lb} \leq N(\theta) \leq N_{ub}$$

$$UMF_{@LW=1} \leq UMF_c$$

$$0.99 \cdot N_{target} \leq N_{avg} \leq 1.01 \cdot N_{target}$$

$$\left|1 - \eta_{net,k}/\eta_{net,k+1}\right| \leq 5 \cdot 10^{-5}$$

Optimization was performed by adding a constraint on average speed to the previous optimization problem. Also, the optimization was performed by changing the intake manifold pressure to optimize the throttled operating condition.

3.4.1. Optimal speed profile

Setting the average cycle speed to 1,000 RPM, the optimal speed profile was found by changing the intake manifold pressure. Intake manifold pressure was varied from 0.4 atm to 1.0 atm in 0.2 atm increments. Figure 3.32 shows the optimal speed profiles in this simulation condition.

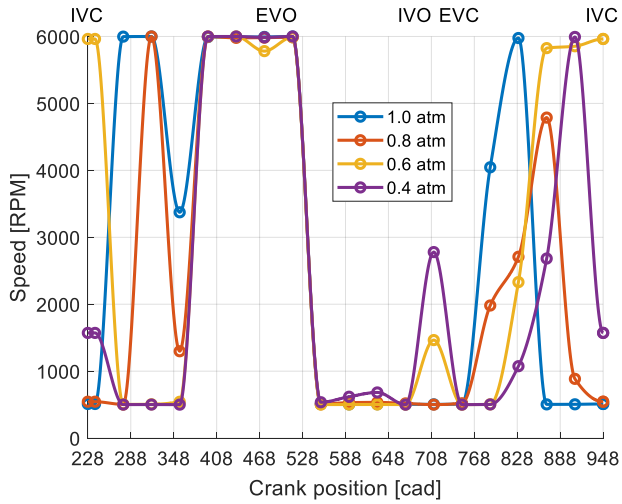

Figure 3.32 Optimal speed profile at various intake manifold pressure

The speed profile of the compression, exhaust, and intake process varied with the intake manifold pressure. As the intake manifold pressure increased, the speed of compression and intake process increased. Under high intake manifold pressure conditions, combustion duration is important for knock mitigation. High speed during the compression and intake process could enhance burn rates and assist knock mitigation. Under low intake manifold pressure conditions, burned gas could be transferred from the exhaust manifold to the intake manifold during the valve overlap interval. The high residual mass fraction at IVC timing could reduce LHV of in–cylinder gas, leading to a relative increase in pumping loss. High speed of valve overlap interval could reduce backflow to the intake manifold.

Next, optimization in the WOT condition was performed by varying the average speed from 1,000 RPM to 5,000 RPM at 1,000 RPM intervals. Figure 3.33 shows the optimal speed profiles at various average speeds.

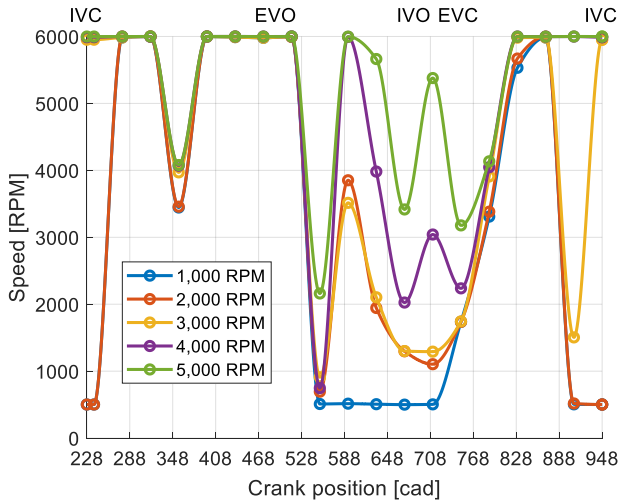

Figure 3.33 Optimal speed profile at various average speeds

With a variation in target speed, the speed profile change around compression, expansion, and firing TDC was not large, and the speed profile of the exhaust process mainly changed. This is because the speed near the firing TDC has a greater effect on efficiency than the speed of the exhaust process. Exhaust process speed cannot significantly change in–cylinder flow dynamics from IVC timing to EVO timing. Heat loss and combustion phasing were not significantly changed as the average speed increased with modulating exhaust process speed. Therefore, the average speed was adjusted to the target speed by controlling the exhaust process speed.

3.4.2. Variation in intake manifold pressure

Figure 3.34 shows the net indicated efficiency difference and energy analysis results when operating with the optimum speed profile obtained in section 3.4.1 and operating with the conventional profile. The average speed was fixed at 1,000 RPM, and only the intake manifold pressure was changed. The efficiency difference increased as the intake manifold pressure was increased.

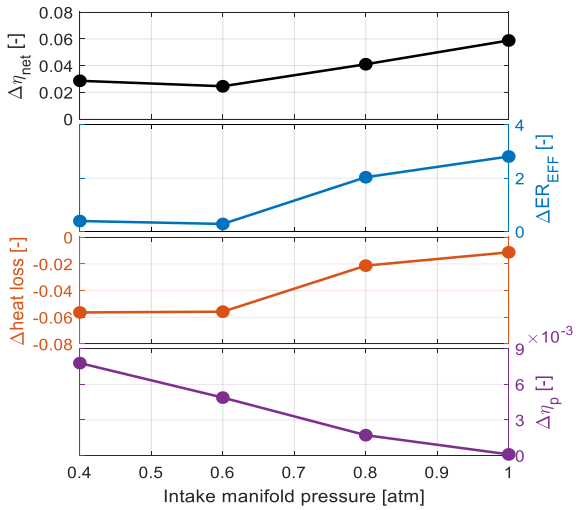

Figure 3.34 Difference between conventional operation and optimal speed profile operation at difference intake manifold pressure

To study the cause of the efficiency difference, factors affecting the efficiency were analyzed in terms of combustion phasing, heat loss, and pumping work. First, we examined the combustion phasing. Combustion phasing improved under all intake manifold pressure conditions. The operating condition in which combustion phasing was the most improved was the high intake manifold pressure condition. This condition is the retarded spark timing operating condition for knock mitigation in conventional engine operation. Speed profile modulation operation could improve combustion phasing by knock mitigation using not only spark timing but the intake, compression, and firing TDC speed profile modulation.

Second, heat loss analysis was performed. The amount of heat loss between IVC and EVO timing was normalized to the in–cylinder gas LHV at IVC timing. The improvement of heat loss increased as the intake manifold pressure decreased. The

expansion process speed in the optimum speed profile was faster than in conventional operation, so heat loss was reduced.

Finally, pumping work was compared. Pumping work showed greater improvement when the intake manifold pressure was lower. In the conventional speed profile, there was a large loss due to the difference between the exhaust manifold and intake manifold pressure when throttled conditions. Exhaust process operation at a low rotating speed reduced pumping loss. In addition, the high speed of valve overlap interval could reduce backflow to the intake manifold.

3.4.3. Variation in average speed

Figure 3.35 shows the net indicated efficiency difference and energy analysis results when operating with the optimum speed profile with variation in average speed and operating with the conventional profile. Intake manifold pressure was fixed at 1.0 atm, and cycle average speed was varied. Net indicated efficiency increased at all average speeds compared to conventional engine operation. The greatest improvement of net indicated efficiency occurred at a low average speed.

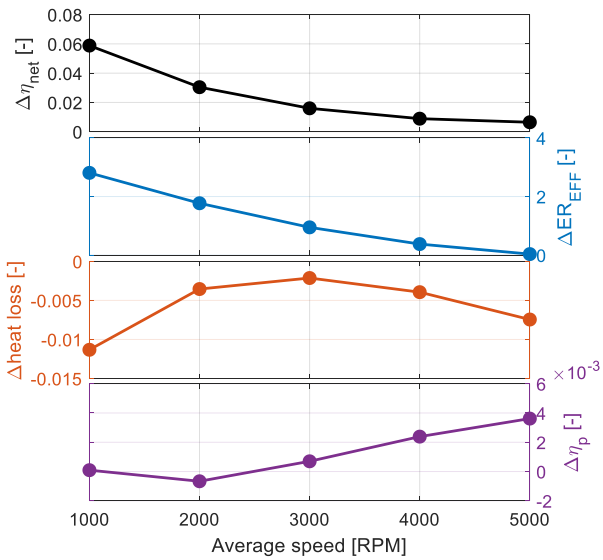

Figure 3.35 Difference between conventional operation and optimal speed profile operation at difference average speed

The reasons for efficiency improvement were analyzed as in section 3.4.2. Combustion phasing was improved under all average speed conditions. Knock occurred mainly under low engine speed operating conditions because time–based combustion duration is increased as the engine speed decreases. Speed profile modulation of the intake and compression process leads to enhanced burn rates, so combustion phasing improved with speed profile modulation at the low average speed condition.

Next, heat loss was analyzed. In WOT condition, retarded spark timing for knock mitigation led to reduced time in high temperature and pressure gas states under low–speed conditions. Under high average speed operating condition, the expansion process speed difference between the optimum speed profile and conventional operation was not large. Thus, the improvement in heat loss was modest.

Finally, pumping work was analyzed. As the average speed increased, the improvement of the pumping work became larger. This was achieved by pressure equilibrium between the manifold and in–cylinder by operating at a slower speed than the operation of the conventional engine.

3.4.4. Full operating map

Using the same method as described above sections, optimization was performed for the range of intake manifold pressure of 0.4 to 1.0 atm and an average speed of 1,000 to 5,000 RPM. Figure 3.36 shows the efficiency and efficiency improvement with modulating the intracycle speed profile.

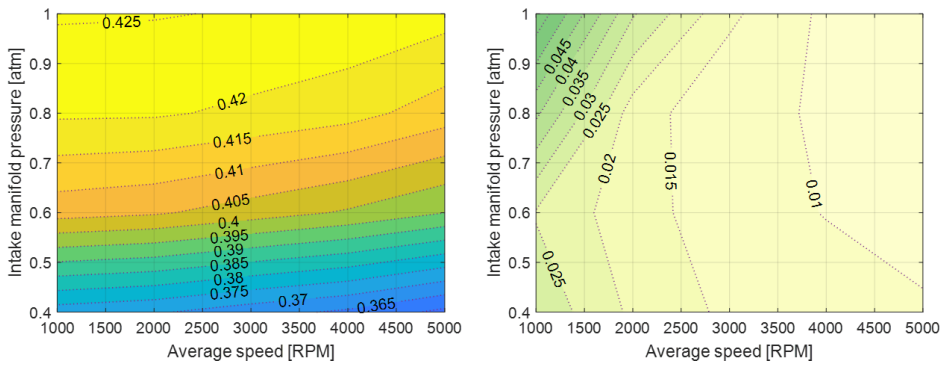

Figure 3.36 Efficiency map of optimal speed profile operation and efficiency difference

The efficiency improvement of the low speed and high load operating conditions is remarkable, and the efficiency is deteriorated due to the knocking in conventional operation. To analyze which performance parameters mainly influenced the efficiency improvement, we compared the performance parameters of conventional operation and optimal speed profile operation.

Combustion phasing is mainly improved in the operating area, where efficiency improvement is remarkable, as shown in Figure 3.37. Therefore, effective knock mitigation is possible through the intracycle speed profile modulation. In the low intake manifold pressure conditions, the improvement of heat loss and pumping work is noticeable.

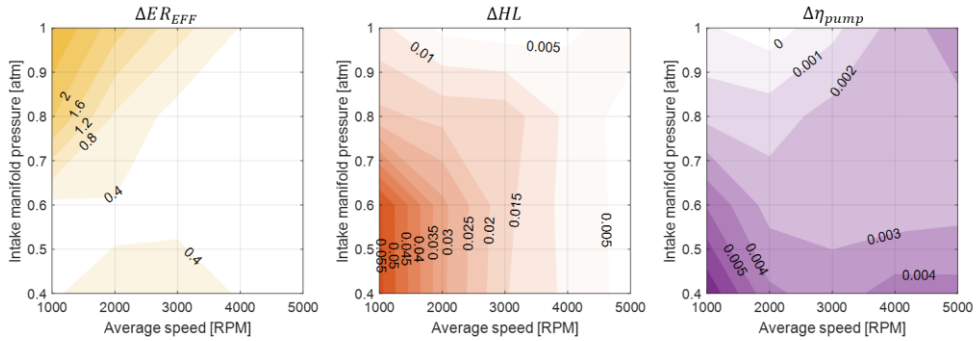

Figure 3.37 Performance parameters difference between the conventional operation and optimal speed profile modulation

3.5. Model validation

Three–dimensional computational fluid dynamics (CFD) simulation was performed to validate the quasi–dimensional SI engine model. The CFD software CONVERGE was applied to obtain the in–cylinder flow dynamic characteristics. The simulation interval was from the EVO timing to the firing TDC timing because the main object of the validation was the comparison of the turbulence intensity profile in the quasi–dimensional model and three–dimensional model. Therefore, the cold–flow simulation results of quasi–dimensional model and three–dimensional model were compared.

The generalized renormalization group (RNG) k–epsilon turbulence model was selected for modeling the in–cylinder and manifold turbulent flow in three–dimensional model. The engine intracycle speed profile could be imported as a function of the crank position in CONVERGE. The engine_speed.in file included the engine speed profile information. Wall boundary condition was applied to all boundary except for the inlet of the intake manifold and outlet of the exhaust manifold, and uniform initial condition was used.

Modeling coefficients of the quasi–dimensional model did not adjust. Modeling coefficients used in previous studies were used without modification to discuss the effect of speed profile modulation in the general SI engine. Therefore, the absolute value of the turbulence intensity could be different between the quasi–dimensional model and the three–dimensional CFD model. The tendency of turbulence intensity and the effect of the speed profile modulation on the turbulence intensity profile could be used to validate the quasi–dimensional SI engine model.

In this section, the turbulence intensity profile obtained by the QD model compares with the CFD simulation results. A comparison of the turbulence intensity profile in the optimal speed profile operation and conventional operation, the speed profile modulation during the intake and compression process, and the effect of speed profile modulation on the pumping work are summarized.

Firstly, simulation results under the optimal speed profile and conventional operation were compared. In Figure 3.38, the speed profile of optimal and conventional operation is shown.

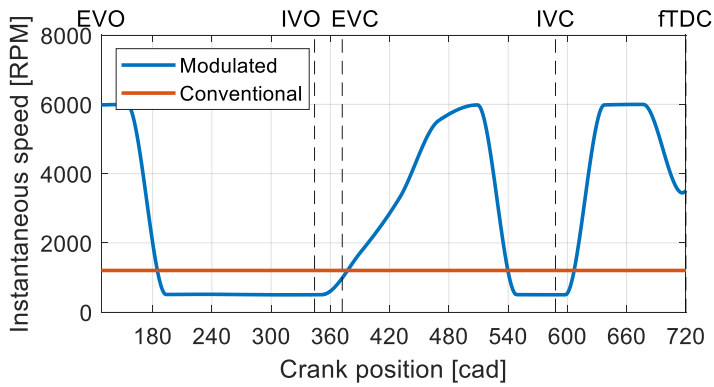

Figure 3.38 The speed profile of the optimal and conventional operation

In Figure 3.39 and Figure 3.40, turbulence intensity profiles according to the crank position obtained by quasi–dimensional model and CFD model are shown respectively. The difference of absolute turbulence intensity can be found, but the turbulence intensity profile of quasi–dimensional model and CFD model were similar in the tendency. The CFD simulation was not the result of iterative simulation until the convergence but the result of single–cycle simulation, so the initial condition of the QD model and CFD model is different. However, turbulent flow dynamic characteristics of the exhaust process do not significantly affect the turbulence intensity during the intake and compression process, as shown in

Figure 3.13. Moreover, turbulent flame speed and heat loss are only affected by the turbulence intensity from the IVC timing to the EVO timing. Therefore, the initial condition difference does not significantly affect the turbulence intensity profile and analysis of simulation results.

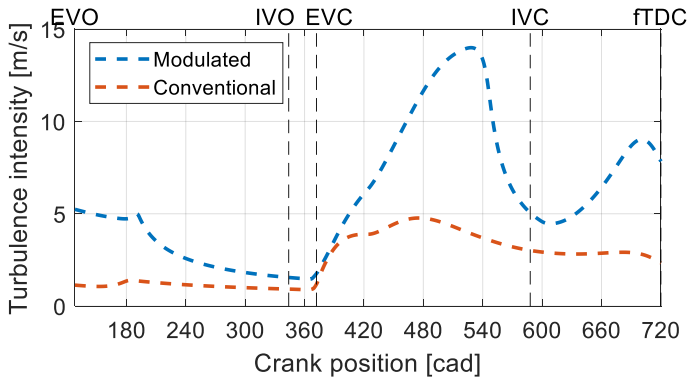

Figure 3.39 The turbulence intensity profile of optimal and conventional operation obtained by the quasi–dimensional SI engine model

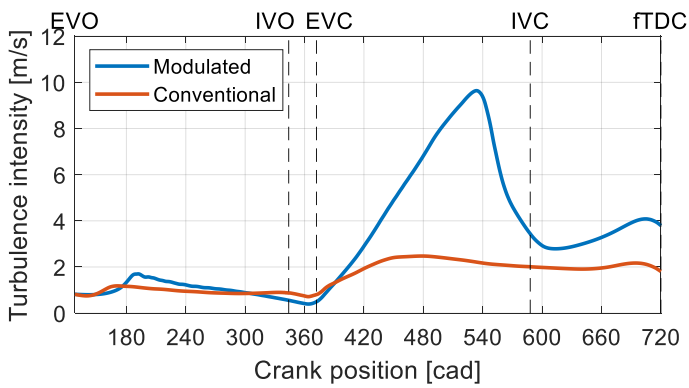

Figure 3.40 The turbulence intensity profile of optimal and conventional operation obtained by the CFD model

Figure 3.39 and Figure 3.40 show the speed profile modulation effect on the turbulence intensity profile during the intake process. The incoming turbulent kinetic energy increment due to the increase in engine speed during the intake process predicted by the quasi dimensional model can be validated by the three–

dimensional CFD simulation results. In addition, the increase in turbulence intensity near the firing TDC is validated by the CFD simulation result. The turbulence intensity enhancement during the compression process of QD simulation results is greater than that of CFD simulation results. This quantitative enhancement ratio difference can be reduced by tuning of the turbulence modeling coefficients.

Secondly, the effect of speed profile modulation during the intake process on the turbulence intensity is compared. In section 3.3.3, effects of speed profile modulation during the intake process on the performance parameters were summarized. The turbulence intensity increases due to the high incoming turbulent kinetic energy as increasing the intake process speed. In Figure 3.41, the incoming turbulent kinetic when the speed during the intake process is 4,000 RPM is higher than when the speed during the intake process is 2,000 RPM. This tendency also appeared in CFD simulation results, as shown in Figure 3.42. Additionally, the turbulence intensity reversal is also shown in CFD simulation when comparing the optimal speed profile with the intake process speed of 4,000 RPM. The tendency of the turbulence intensity profile near the firing TDC obtained by the QD model is similar to that of CFD simulation.

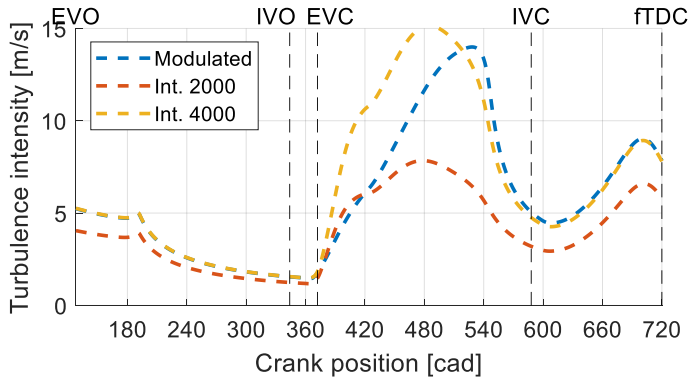

Figure 3.41 The turbulence intensity profile under various intake process speed condition obtained by the QD model

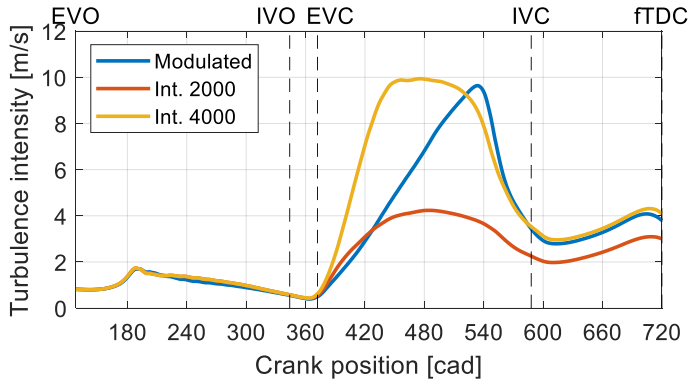

Figure 3.42 The turbulence intensity profile under various intake process speed condition obtained by CFD model

Thirdly, the effect of speed profile during the compression process on the turbulence intensity is compared. In section 3.3.1, the QD SI engine model showed that the turbulence intensity increased as increasing the speed during the compression process. High speed during the compression process enhanced the turbulent kinetic energy production, as shown in Figure 3.43. The turbulence intensity at the IVC timing is not affected by the compression process speed profile. This trend also appeared in CFD simulation results as shown in Figure

3.44. The effect of compression process speed on the turbulence intensity is overestimated in QD model. Engine combustion chamber geometry, spatial distribution, and modeling coefficients are a source of the quantitative difference in the turbulence intensity profile.

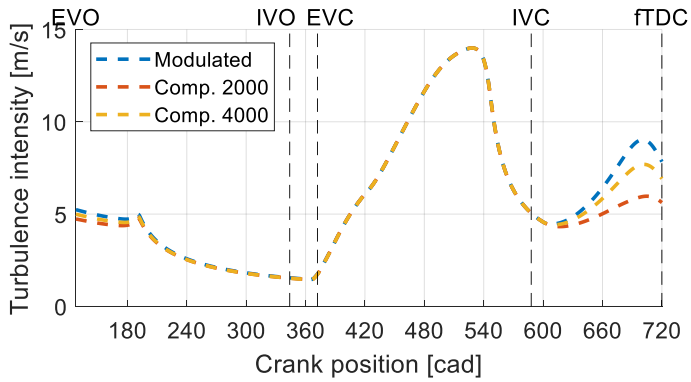

Figure 3.43 The turbulence intensity profile under various compression process speed condition obtained by the QD model

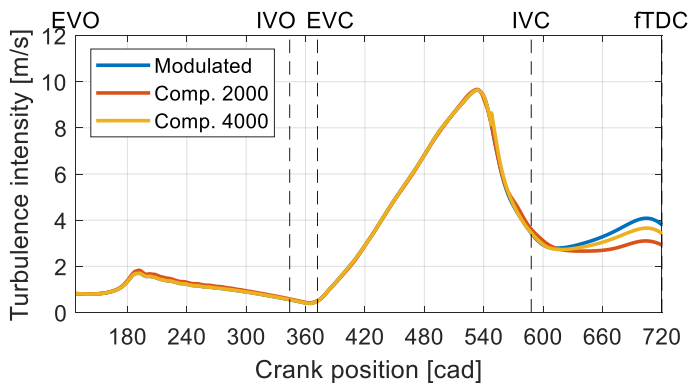

Figure 3.44 The turbulence intensity profile under various compression process speed condition obtained by CFD model

Finally, the pumping work improvement validation is performed. The pressure distribution of conventional operation and optimal speed profile operation at the same crank position are shown in Figure 3.45 and Figure 3.46.

Under the conventional operating conditions, in–cylinder pressure is higher than exhaust manifold pressure due to the volume flow rate difference. The pressure equilibrium timing between the exhaust manifold and cylinder is advanced as decreasing the speed during the exhaust process.

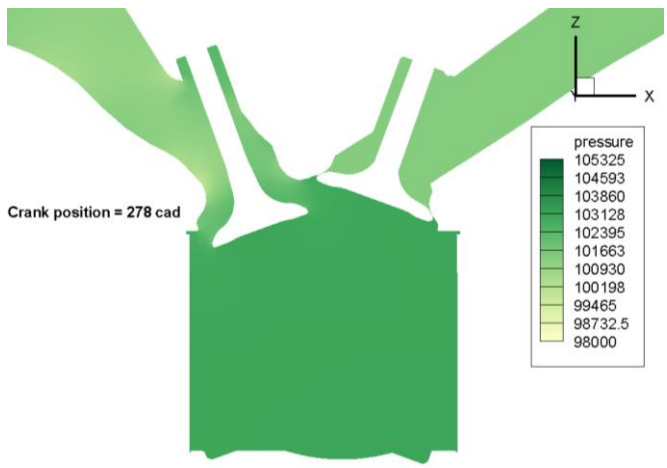

Figure 3.45 Pressure distribution of cylinder and manifold during the exhaust process under conventional operation

Figure 3.46 Pressure distribution of cylinder and manifold during the exhaust process under optimal speed profile operation

Spatial distribution is one of the sources of the quantitative turbulence intensity difference. The turbulent kinetic energy dissipation occurred around the cylinder wall, as shown in Figure 3.47. Figure 3.47 shows that turbulent kinetic energy at the cylinder center is higher than turbulent kinetic energy near the wall. The wall boundary condition for turbulent kinetic energy and dissipation rate is the gradient to zero. The gradient to zero boundary condition is used to model the transport quantities outlet condition. Therefore, in–cylinder turbulent kinetic energy and dissipation rates are transferred to out of the cylinder through the wall. The QD model does not include this wall boundary effect, so overall turbulent kinetic energy can be overestimated.

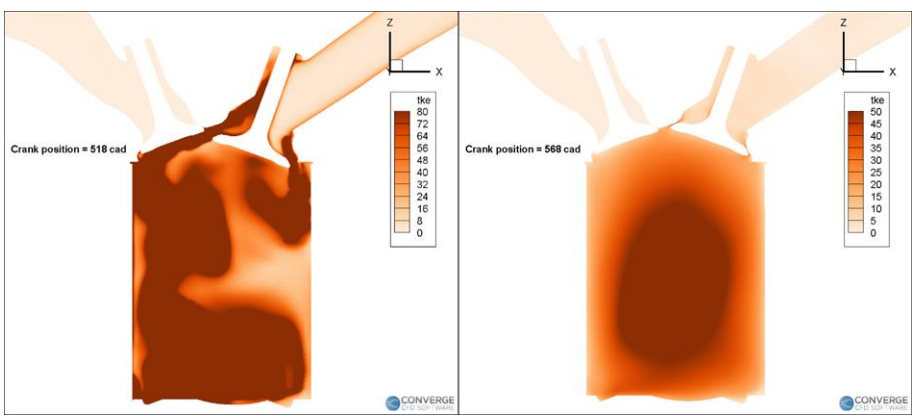

Figure 3.47 Turbulence intensity distribution at different crank position

In Figure 3.48, the turbulence intensity profile with respect to the crank position at a specific point is shown. If Figure 3.48 compared with Figure 3.40, the quantitative value of turbulence intensity near the firing TDC was different. The turbulence intensity at the specific point is higher than the cylinder average turbulent kinetic energy. Moreover, the speed profile modulation effect on enhancing the turbulence intensity was greater than cylinder average value.

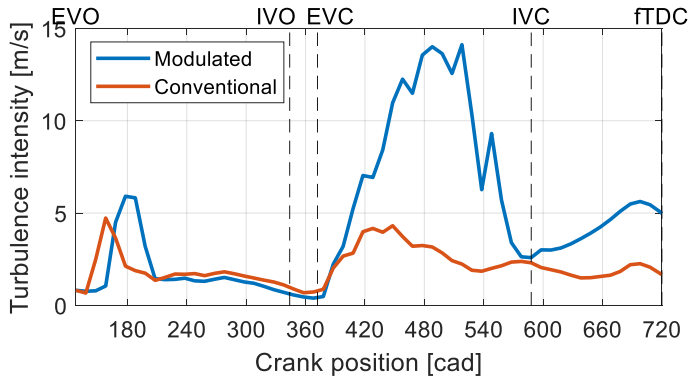

Figure 3.48 Turbulence intensity profile at a specific point of the center plane

Additionally, the effect of intracycle speed profile modulation during the intake and compression process on the heat loss was examined. The amount of heat transfer from the IVC timing to the firing TDC timing was compared. In section 3.3, simulation results showed the heat loss decreased as decreasing the interval II and VI speed. These intervals affected the turbulence intensity during the expansion process. Higher turbulence intensity increased the convective heat transfer coefficient, so the heat transfer rate could increase as increasing the interval II and VI speed.

Firstly, the effect of the intake process speed profile on the heat loss was examined. If there was no heat loss, the compression process must be an isentropic process. Therefore, the internal energy of in–cylinder gas could be calculated using the thermodynamic states at the IVC timing. Figure 3.49 showed the internal energy difference between the CFD simulation results and isentropic simulation results. Heat loss during the compression process decreased as decreasing the intake process speed. As shown in Figure 3.42, the turbulence intensity during the compression process decreased as decreasing the speed of the intake process.

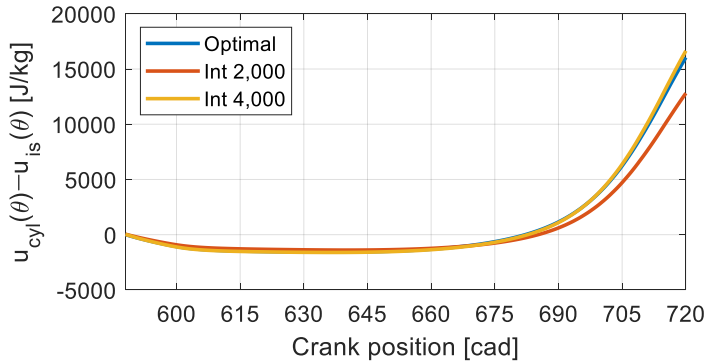

Figure 3.49 Internal energy difference between the CFD simulation results and isentropic process simulation results

Chapter 4. Speed profile modulation with SI engine efficiency improvement technologies

In order to reduce carbon dioxide emissions from automobiles, many studies are being conducted to improve the efficiency of SI engines. In order to increase the efficiency of the SI engine, various technologies such as increasing the compression ratio, downsizing the engine, and lean–burn have been studied. Among other technologies, this study attempted to investigate the possibility of additional efficiency increase or extension of the operating limits by applying the intracycle speed profile modulation to high compression ratio, boosting operation to increase diluent operation or downsized engine output, and lean–burn operation.

4.1. High geometric compression ratio

In the results of section 3.4, the operating condition that can greatly increase the efficiency through intracycle speed profile modulation is a low speed and high intake manifold pressure. The efficiency of this operating condition is greatly increased because effective knock mitigation can be achieved through speed profile modulation. Therefore, the operating condition limited by knocking could be extended. Firstly, increasing the compression ratio is investigated.

There are two ways to increase the compression ratio. One is changing the engine stroke. The other is decreasing the clearance volume. In this study, decreasing the clearance volume was chosen. The engine stroke affects the engine piston speed. The piston speed limits the maximum engine speed that can be reliably operated in an SI engine. Under the same engine speed condition, the engine piston speed increases as increasing the stroke length. This speed upper bound changing can make complexities to

compare optimization results under different compression ratios. The purpose of this study is to see the effect of the intracycle speed profile on efficiency. Therefore, the stroke was fixed, and the optimization was performed with the fixed upper bound of the engine speed.

Simulations were conducted under the various geometric compression ratio and conventional operating conditions. Figure 4.1 shows the net indicated efficiency of the WOT conditions with different compression ratios at 2,000 RPM conditions.

If the compression ratio increases, the efficiency should increase. However, the above result shows that the efficiency is deteriorated even if the compression ratio is increased. When low intake manifold pressure conditions, the efficiency increases as the compression ratio increases. That indicates the effect of the surface to volume ratio is not significant on the efficiency limit in high intake manifold conditions. Thus, the geometric compression ratio is limited by the knocking in high intake manifold pressure conditions. Even if the geometric compression ratio is increased, retarding the spark timing for knock mitigation decreases the effective expansion ratio. This can be seen in Figure 34. Increasing the geometric compression ratio cannot lead to an increase in the effective expansion ratio of conventional operation.

In section 0, results show that combustion phasing is improved with modulating intracycle speed profile under the knock–limited case. Therefore, the efficiency can be improved in high compression ratio conditions. Figure 4.1 and Figure 4.2 show the net indicated efficiency and effective expansion ratio at high compression ratio operation when operating with the optimal speed profile.

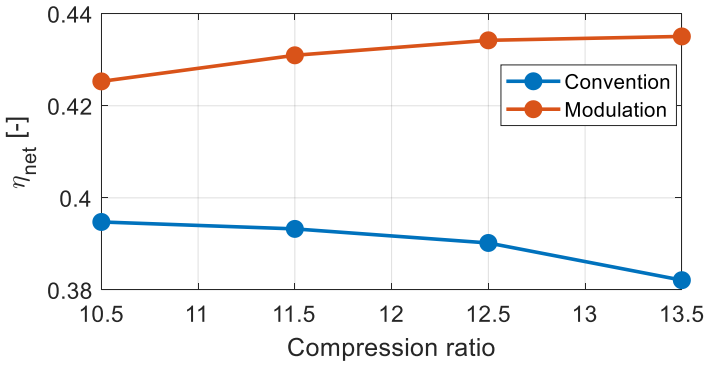

Figure 4.1 Efficiency of conventional operation and optimal speed profile operation

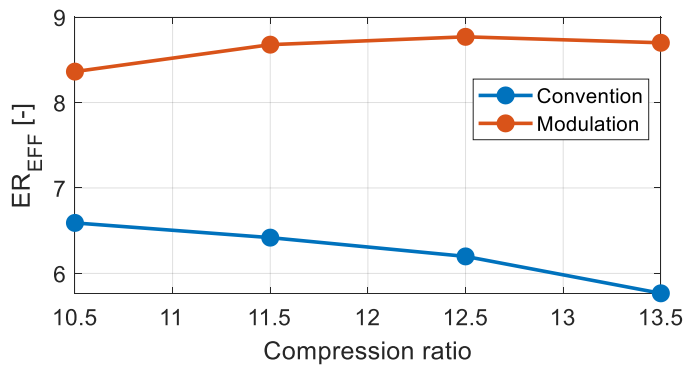

Figure 4.2 Effective expansion ratio of conventional operation and optimal speed profile operation

The intracycle speed profile was optimized compression ratio up to a compression ratio of 13.5. The effective expansion ratio is highest when the geometric compression ratio is 12.5, as shown in Figure 4.2. Even if the geometric compression ratio is greater than 12.5, the effective expansion ratio is not increased by intracycle speed modulation.

Although the effective expansion ratio does not increase, the net indicated efficiency increases due to the reduced heat loss, as shown in Figure 4.3. The shorter interval from the end of combustion to exhaust valve opening timing when the compression ratio is

13.5, heat loss decreases. Therefore, the efficiency increases even though the effective expansion ratio is lower than the compression ratio of 12.5 cases.

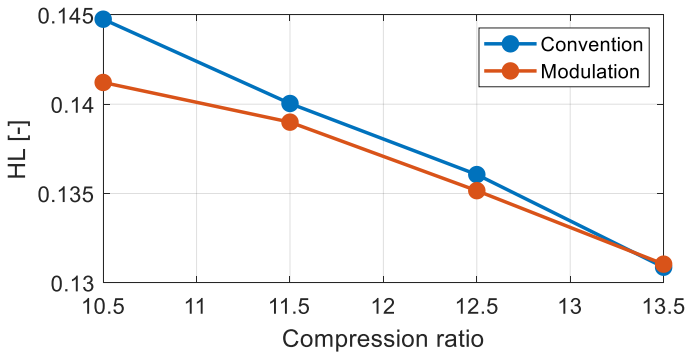

Figure 4.3 Heat loss of conventional operation and optimal speed profile operation

When speed profile modulation is performed with an increased compression ratio, the optimal speed profile is plotted, as shown in Figure 4.4. As the compression ratio is increased, the speed of the intake process and around the firing TDC is increased to the upper bound.

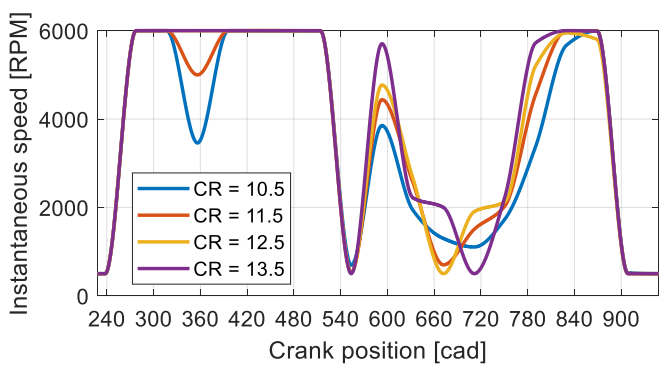

Figure 4.4 Optimal speed profile at 2,000 RPM with various compression ratios

As the geometric compression ratio rises, pressure and temperature of in–cylinder gas are increased around the firing TDC. Knocking occurs better in this state because the ignition delay of the unburned mixture is shortened. Speeds up around the firing TDC to reduce residence time at high temperatures and pressures to mitigate the knocking. In

addition, the intake process speed of the optimal speed profile is increased to increase the turbulent flame speed. This shows that the speed profile is optimized to mitigate the knocking when the compression ratio is increased.

4.2. Boosting condition

Another condition that is significantly affected by knock is the boosting condition that the intake manifold pressure is higher than atmospheric pressure. Boosting operation increases the load in the downsized engine and diluent operating engine.

However, increasing the intake manifold pressure leads to high in–cylinder pressure during the compression and combustion process. High in–cylinder pressure reduces the ignition delay of the unburned mixture, and it causes the knocking. Although the efficiency of the low–load condition is improved by applying the downsizing engine, knocking reduces the efficiency under the high load operating conditions. If this problem can be solved through intracycle speed profile modulation, more aggressive engine downsizing or higher diluent operation can be possible.

As with improving the efficiency in the high compression ratio engine through the intracycle speed profile modulation, effective knock mitigation can be achieved in intake manifold pressure boosting operation. In this study, using the turbocharger was assumed to increase the intake manifold pressure. Since the developed model does not include the manifold dynamics, the system with the turbocharger is modeled by the thermodynamic state change of the intake and exhaust manifold. Since the exhaust manifold temperature has a relatively small effect on engine efficiency, modeling the exhaust manifold temperature was not performed. The exhaust manifold pressure and intake manifold temperature were modeled as a function of intake manifold pressure and engine speed. In the intracycle speed modulating case, average engine speed was used for this correlation function because the cycle duration determines the choking of the turbine inlet in steady operation.

When calculating the intake manifold temperature variation, the engine speed has no significant effect because the temperature of compressed gas is the only function of a pressure ratio. Therefore, intake manifold temperature is expressed only as a correlation to intake manifold pressure.

$$T_{in} = 16.14 \cdot (p_{in} - p_o)/10^5 + 303.15 \quad (4.1)$$

Exhaust manifold pressure was affected by both intake manifold pressure and engine speed. Therefore, it is expressed as a correlation between engine speed and intake manifold pressure.

$$p_{ex} = p_o + (3.26 \cdot 10 \cdot (p_{in} - p_o)/1e5 + 5.12) \cdot N_{avg} \quad (4.2)$$

Using these correlations, simulations under boosting conditions were performed, and the efficiency of the conventional operation at 2,000 RPM is shown in Figure 4.5.

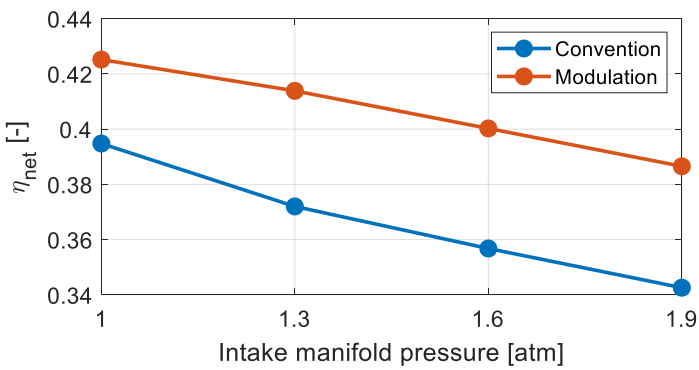

Figure 4.5 Efficiency of conventional operation and optimal speed profile operation

In the conventional engine, the efficiency decreases as the boosting pressure increases, and engine speed decreases. As can be seen in Figure 4.6, the combustion phasing deterioration caused by spark retarding for knock mitigation is greatly increased under the boosting condition. Speed profile modulation was optimized to improve the combustion phasing.

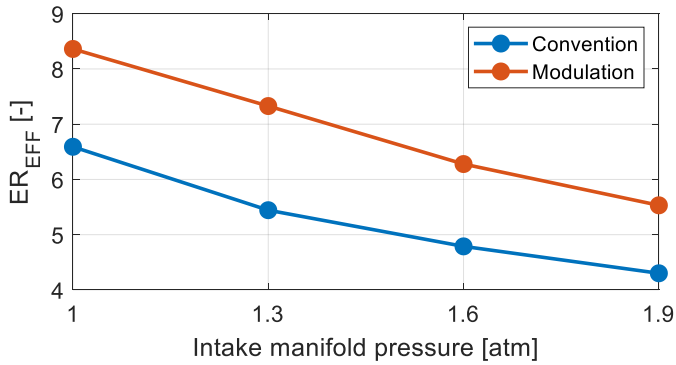

Figure 4.6 Effective expansion ratio of conventional operation and optimal speed profile operation

Like the optimizations performed in previous sections, the reason for the increased efficiency in this operating condition is the combustion phasing improvement. As shown in Figure 4.6, we can see that the effective expansion ratio has increased in all operating conditions where simulations were performed. The effective expansion ratio is improved with the optimal speed profile.

When the intake manifold pressure is 1.0 atm, the optimal speed profile that improves the combustion phasing is shown by slightly lowering the speed around the firing TDC, as shown in Figure 4.7. However, from the intake manifold pressure of 1.3 atm or more, the lowered somewhat speed profile around the firing TDC cannot be seen. It operates at a speed corresponding to the upper bound from the IVC timing to the EVO timing, and the knocking is mitigated by spark timing retarding.

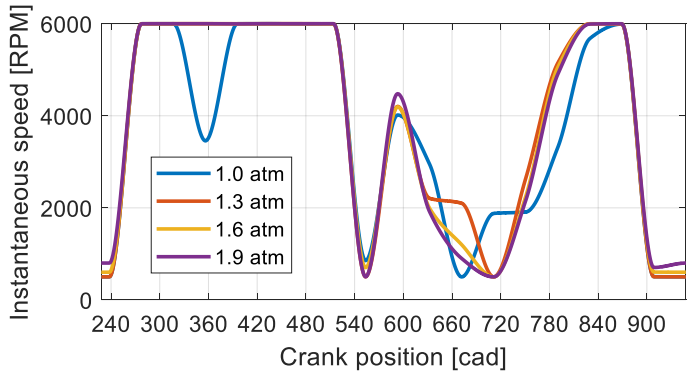

Figure 4.7 Optimal speed profile under boosting conditions

4.3. Lean burn operation

Lean–burn increases the thermodynamic efficiency by increasing the specific heat ratio of the gas and by reducing the heat loss by lowering the temperature of the gas after combustion. Besides, the ignition delay of the lean mixture is longer than that of the stoichiometric mixture at a specific temperature and pressure, which helps to knock mitigation in the SI engine. The disadvantage is the slow laminar flame speed and reduced engine load. Among these features, the application of intracycle speed profile modulation could improve the efficiency of the lean–burn SI engine by improving combustion phasing deterioration due to the reduction of laminar flame speed.

Since the output of the engine changes with different equivalence ratios, the efficiency is shown for the net indicated mean effective pressure (NMEP) change. The simulation was performed by varying the intake manifold pressure from 0.4 to 1.0 atm, and the NMEP was calculated under each simulation condition. Figure 4.8 shows the results of conventional operation when the equivalence ratio is 1 and 0.7 and optimal speed profile operation when the equivalence ratio is 0.7 at 2,000 RPM of average speed.

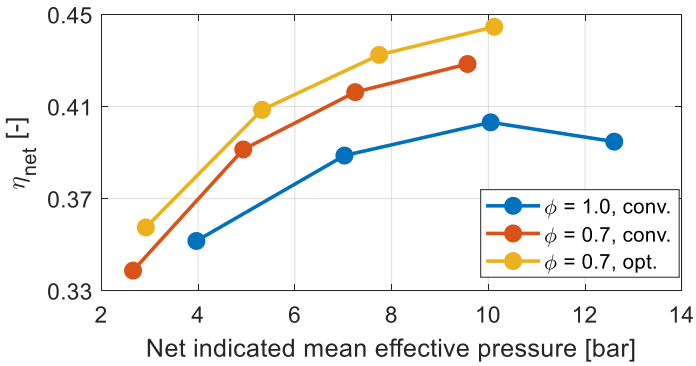

Figure 4.8 The net indicated efficiency of lean–burn operations

Lean–burn operation reduces the maximum NMEP of the engine and is more efficient than stoichiometric conditions in the low NMEP condition. Applying intracycle

speed profile modulation adds additional efficiency improvements and increases the maximum NMEP compared to conventional operation due to increased efficiency.

To analyze how intracycle speed profile modulation affects the efficiency improvement in the lean–burn SI engine, each performance parameter was calculated. First, combustion phasing is examined as shown in Figure 4.9. The lean mixture is expected to improve the combustion phasing due to robust operation to knock with increased ignition delay, but combustion phasing is worsened in conventional lean–burn operation.

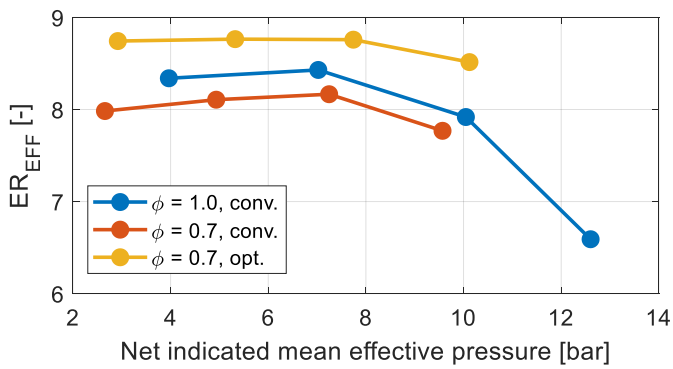

Figure 4.9 The effective expansion ratio of lean–burn operations

To find out why combustion phasing worsens in a lean–burn SI engine, turbulence intensity of IVC timing is compared. Since there is little difference in turbulence intensity of IVC timing in conventional operation, the combustion phasing is deteriorated due to the decrease in laminar flame speed in lean–burn operation.

By applying intracycle speed profile modulation in lean–burn operation, combustion phasing can be improved higher than stoichiometric operation. Therefore, the effect of using a knock–resistant mixture can be obtained more prominently in the case of speed profile modulation. This can be achieved by increasing the turbulence intensity using

intracycle speed profile modulation, overcoming the effect of reducing the laminar flame speed.

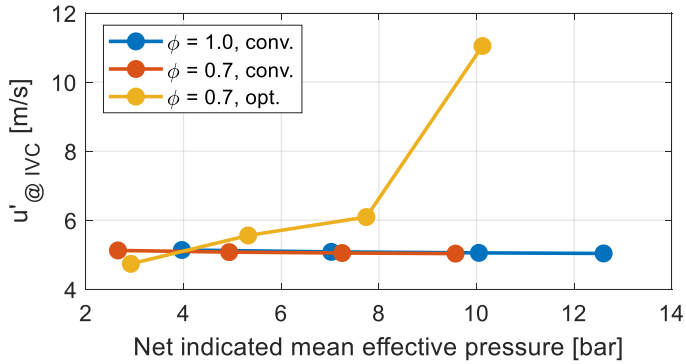

Figure 4.10 Turbulence intensity at IVC timing

Next, heat loss was compared. At the same NMEP condition, heat loss is decreased as decreasing the equivalence ratio. Since the burned gas temperature is lower in the lean mixture, heat loss is reduced. By applying intracycle speed profile modulation, heat loss can be reduced by modulating the expansion process speed profile as previously analyzed in addition to the lean–burn operation effect.

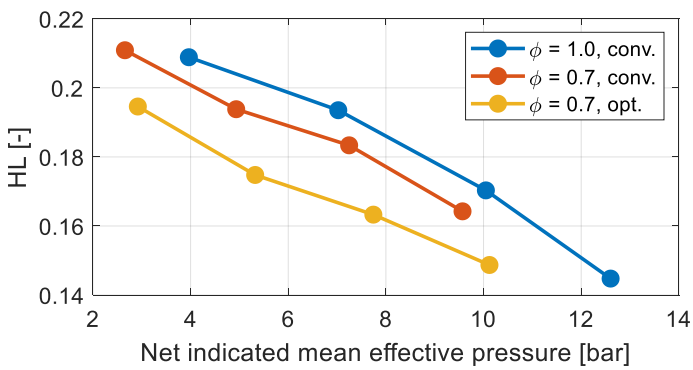

Figure 4.11 Heat loss of lean–burn operation

Finally, the pumping work was analyzed. Pumping work is improved because the intake manifold pressure is higher than the stoichiometric operation to achieve the same load in lean–burn operation. When intracycle speed profile modulation is applied,

combustion phasing is greatly improved. Therefore, the pumping work may be worsened by the reduced pressure of EVO timing compared to conventional operation, as shown in Figure 4.13.

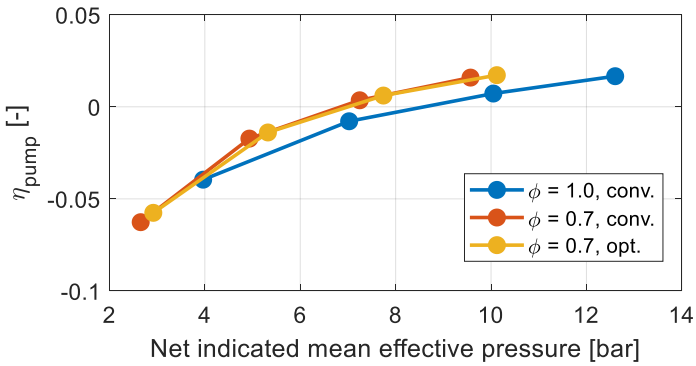

Figure 4.12 Pumping efficiency of lean–burn operation

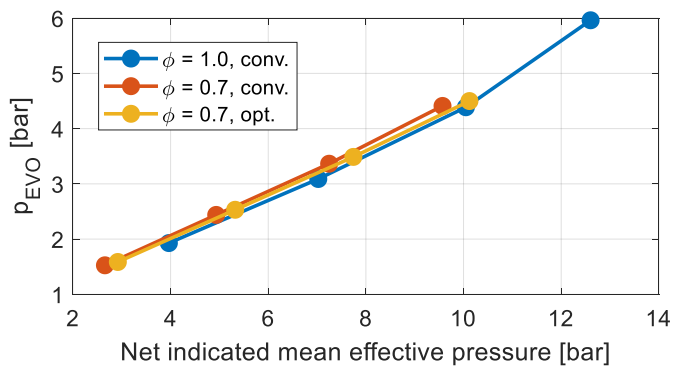

Figure 4.13 In–cylinder pressure at EVO timing

Speed profile modulation of the expansion process improves heat loss to compensate for the pressure reduction of the EVO timing, and exhaust process speed profile modulation increases the pV work of the gas exchange process to the conventional operation level.

In conventional operation, efficiency is increased by improving heat loss and pumping work under the same NMEP condition. Besides, there will be an increase in

efficiency due to the effect of increasing the specific heat ratio that is a characteristic of the lean mixture. The maximum NMEP that can be obtained by the lean–burn operation is reduced, but the above effects can increase efficiency at low to medium NMEP. Applying intracycle speed profile modulation to this results in further improvements in combustion phasing and heat loss, and the net indicated efficiency increases by about 4% p compared to the medium NMEP of conventional operation.

Chapter 5. Conclusion

5.1. Conclusion

A quasi–dimensional SI engine model was developed to reflect the intracycle speed profile modulation effect. A model including in–cylinder flow dynamics was used, and an SI engine model was developed that did not use correlations related to average speed using models. Using the developed model, the effect of speed profile modulation on calculating the burning rate or heat transfer rate was reflected that was developed in many previous studies. Besides, the quasi–dimensional model including the knocking model was used to confirm the effect of speed profile modulation in the operating conditions where the efficiency of the SI engine is limited by knocking.

Trajectory optimization was performed using the SI engine model that can reflect the speed profile modulation effect. Some assumptions that used to reduce the computational costs in previous studies were not used. Since the gas exchange process affects in–cylinder flow characteristics, full–cycle optimization including the gas–exchange process was performed. The optimization problem was solved by changing the trajectory optimization problem to the parameter optimization problem using the discretization–based method. By setting the knocking, average speed, and speed upper and lower bound as constraints, the optimal speed profile that can operate stably under various conditions was obtained.

When speed profile modulation was performed, the reasons for efficiency improvement were divided into combustion phasing, heat loss, and pumping work. Each performance parameters are improved by modulating the intracycle speed profile. Sensitivity analysis was performed on the speed profile of each interval, and the interval that had a major influence on each performance parameter was presented.

The intracycle speed profile was optimized under the typical SI engine operating conditions using theses method. When the engine is operated with the optimal speed profile under the WOT condition, the efficiency improvement of 5% p and 1% p is obtained compared to the same average speed condition and best efficiency operation, respectively. The reason for the increase in efficiency was that combustion phasing and heat loss were remarkably improved compared to conventional operation under the same speed condition, and the heat loss and pumping work were improved compared to the condition with the highest net indicated efficiency.

It was confirmed that combustion phasing worsened by knocking at the same average speed was improved up to the combustion phasing at the knock–free operation level through intracycle speed profile modulation. This could be achieved by increasing the turbulence intensity of the combustion process by increasing the speed of the intake and compression processes. Higher turbulence intensity also increases turbulent flame speed, and it reduces time–based burn duration. Therefore, the flame arrives before the unburned mixture auto–ignite during the combustion process. The improvement of heat loss was also achieved by speeding up the expansion process. By improving the speed of the expansion process, heat loss can be improved by reducing the time duration of heat transfer during the expansion process. Pumping work could be improved by improving heat loss and exhaust process speed profile modulation.

When optimization was performed with varying engine intake manifold pressure and average speed, the improvement in efficiency in the low speed and high intake manifold pressure condition was noticeable. This is because the combustion phasing deteriorated due to the knocking was improved by modulating the speed profile. In the low intake manifold pressure condition, it was confirmed that the efficiency improvement

could be achieved by improving heat loss and pumping work through speed profile modulation.

We have examined the benefits of using this speed profile modulation effect in combination with strategies to improve the efficiency of the SI engine. In this study, the speed profile optimization under the high compression ratio, lean–burn, and boosting operation to increase engine load was performed. First, in conventional operation, although the compression ratio was increased under high intake manifold pressure conditions, the efficiency decreased due to knocking, but the compression ratio limit was increased to 13.5 through speed profile modulation. The efficiency gains due to conventional operation under lean–burn operation conditions, an additional efficiency gain of about 1.5% p was obtained by improving combustion phasing through turbulence intensity enhancement. Lastly, in the boosting condition, the efficiency was decreased even though the speed profile modulation was applied due to the increased intake manifold pressure, but the reduction was smaller than the conventional operation. In addition, when boosted to 1.9 atm, the operation can be performed at the efficiency level under normal pressure conditions of conventional operation.

The results of this study show that each performance parameter is affected by modulating the speed profile of the specific interval. The general SI engine efficiency improvement limit that could be achieved by the speed profile modulation was discussed. If full–cycle optimization is a difficult situation, it can be used as a basic study of whether changing the speed profile of a particular interval can improve performance parameters that require improvement on a specific engine.

5.2. Future work

In this study, the optimal speed profile for maximizing the net indicated efficiency of the SI engine was obtained using the QD SI engine model. Reasons for the efficiency improvement were investigated from the perspective of combustion phasing, heat loss, and pumping work. However, friction and torque limitation exist in real SI engine, and these factors could affect the optimal speed profile. By obtaining the optimal speed profile that takes these effects into account, the additional efficiency improvement that can be gained from a real SI engine could be analyzed. In this section, preliminary results are discussed.

The effect of friction on the optimal speed profile is analyzed. Patton's friction model was used for friction modeling [62]. This model estimates the friction based on the engine speed and intake manifold pressure. In this study, engine speed was modulated within the single cycle. Therefore, the friction correlation was fitted according to the piston displacement. And then, total friction mean effective pressure (FMEP) was obtained by integrating the instantaneous FMEP. The optimal speed profile considered engine friction is shown in Figure 5.1. The interval with maximum speed was decreased to reduce engine friction.

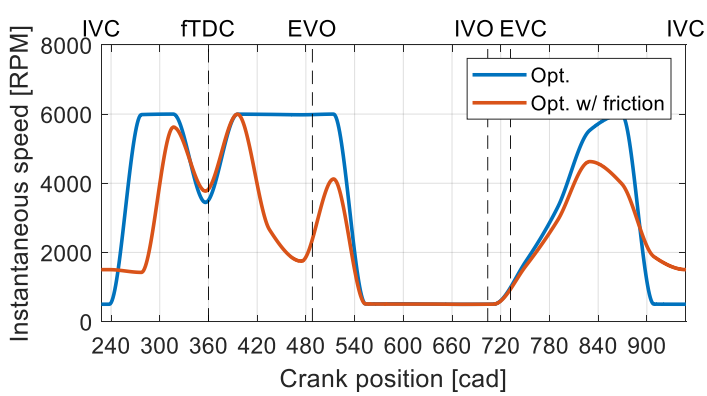

Figure 5.1 The optimal speed profile without and with friction model

The net indicated efficiency, brake thermal efficiency, and performance parameters of speed profile modulating and conventional operation were summarized in Table 5.1.

Table 5.1 Simulation results

	Opt. w/o friction	Opt. w/ friction	Conventional
η_{net} (-)	0.425	0.42	0.37
η_{brake} (-)	0.373	0.38	0.328
ER_{EFF} (-)	8.36	7.92	5.78
HL (-)	0.14	0.15	0.15
η_{pump} (-)	0.016	0.016	0.017
N_{avg} (RPM)	1,200	1,261	1,200

When SI engine operation with optimal speed profile considered engine friction, the net indicated efficiency was deteriorated by worsening the combustion phasing and increasing the heat loss. However, the friction loss was improved, so the brake thermal efficiency was increased. Moreover, when the simulation results of optimal speed profile and conventional operation were compared, the brake thermal efficiency was increased about a 5% p.

Next, the motor maximum torque effect on the optimal speed profile was preliminary analyzed. To consider the motor maximum torque, constraints related to the engine maximum torque was added to the optimization problem. To reflect the torque constraint, the kinematic SI engine model was added [63]. The previous study on the kinematic engine modeling considered the gas pressure, momentum of piston and crankshaft, and external torque. The crankshaft acceleration could be written as Equation (5.1).

$$\dot{\omega}(\theta) = \left(0.5l \cdot \left(F_p - F_{rot}\right)G(\theta) - \tau\right) \cdot \frac{1}{I + M_p\left(0.5l \cdot G(\theta)\right)^2} \quad (5.1)$$

The inertia of crankshaft greatly affected the crankshaft acceleration. As decreasing the crankshaft's moment of inertia, the speed variation in a single cycle increased. Therefore, the minimum moment of inertia was assumed to solve the optimization problem. Maximum motor torque was assumed 200 Nm that was five times the average torque that was calculated from the QD SI engine model. When the maximum torque constraint was added, the optimal speed profile and toque profile could be obtained, as shown in Figure 5.2 and Figure 5.3.

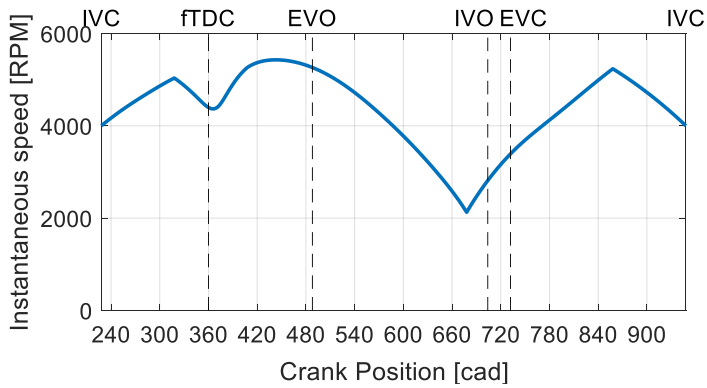

Figure 5.2 The optimal speed profile when maximum torque was limited

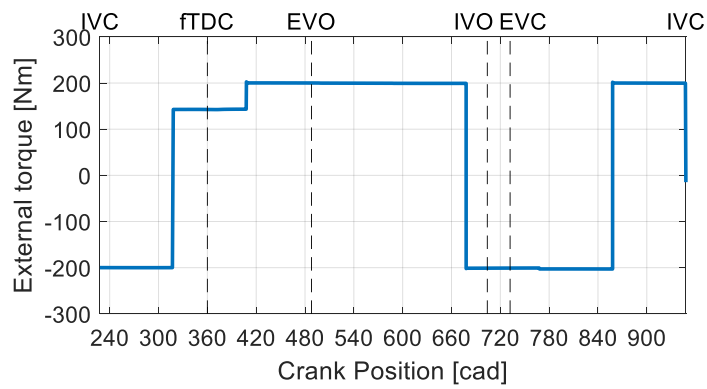

Figure 5.3 The torque profile when maximum torque was limited

Since the maximum torque was limited, speed during the exhaust process could not slow down to the lower bound of speed. When the simulation was conducted with an

optimal speed profile when maximum torque was limited, the net indicated efficiency was 42%, and average speed was 4,000 RPM.

Finally, the optimization problem was configured and solved, when both maximum torque constraint and friction were considered. The optimal speed profile and torque profile are shown in Figure 5.4 and Figure 5.5. When friction and maximum torque constraint were included the optimization problem, the overall speed of the optimal speed profile was decreased.

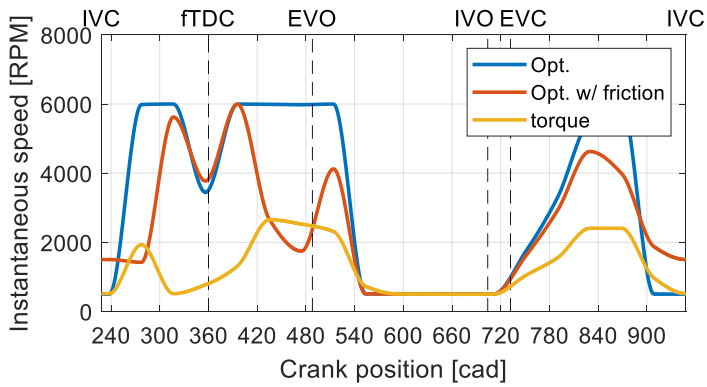

Figure 5.4 Optimal speed profiles under various constraint condition

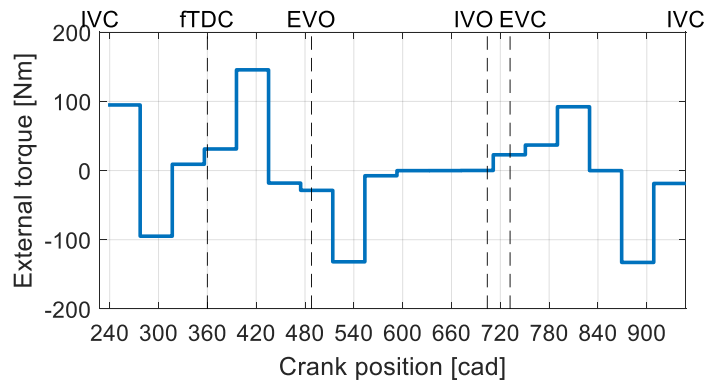

Figure 5.5 The optimal torque profile

These preliminary results show the possibility of efficiency improvement in a real SI engine through the speed profile modulation. The model that was used

in this section could not fully reflect the friction or torque limit effect because there was no model that could implement in speed profile modulating operation. If the friction or kinematic model that can be used in speed profile modulation operation are developed, the optimal speed profile and torque profile in real SI engine can be obtained.

Bibliography

1. EIA, 2017. International Energy Outlook 2017. US EIA, Washington, DC.

2. US EPA, US NHTSA, 2017 and Later Model Year Light-Duty Vehicle Greenhouse Gas Emissions and Corporate Average Fuel Economy Standards. Federal Register, 2012. 77(199): p. 62623-63200.

3. The European Parliament and the Council of the European Union, Regulation (EU) No 333/2014 of the European Parliament and of the Council of 11 March 2014 amending Regulation (EC) No 443/2009 to define the modalities for reaching the 2020 target to reduce CO 2 emissions from new passenger cars. 2014. 57: p. 15-21.

4. Ministry of Economy, Trade and Industry, Final Report of Joint Meeting between the Automobile Evaluation Standards Subcommittee, Energy Efficiency Standards Subcommittee of the Advisory Committee for Natural Resources and Energy and the Automobile Fuel Efficiency Standards Subcommittee, Automobile Section, Land Transport Division of the Council for Transport Policy. 2011.

5. Standardization Administration of China, Fuel Consumption Evaluation Methods and Targets for Passenger Cars (GB 27999–2014). 2014.

6. Bureau of Energy Efficiency, Ministry of Power, Gazette of India REGD. NO. D. L.-33004/99. 2015.

7. Ministry of the Environment, Vehicle Average Fuel Economy and GHG Emission Standards (2016-2020) Notification No. 2014-235 of the Ministry of Environment. 2014.

8. Lajunen, A. and Lipman, T., Lifecycle cost assessment and carbon dioxide emissions of diesel, natural gas, hybrid electric, fuel cell hybrid and electric transit buses. Energy, 2016. 106: p. 329-342.

9. Wolfram, P. and Lutsey, N., Electric vehicles: Literature review of technology costs and carbon emissions. The International Council on Clean Transportation: Washington, DC, USA, 2016: p. 1-23.

10. Onat, N. C., Kucukvar, M., and Tatari, O., Conventional, hybrid, plug-in hybrid or electric vehicles? State-based comparative carbon and energy footprint analysis in the United States. Applied Energy, 2015. 150: p. 36-49.

11. Wang, X., Sun, B.-g., and Luo, Q.-h., Energy and exergy analysis of a turbocharged hydrogen internal combustion engine. International Journal of Hydrogen Energy, 2019. 44(11): p. 5551-5563.

12. Zweiri, Y., Whidborne, J., and Seneviratne, L., Dynamic simulation of a single-cylinder diesel engine including dynamometer modelling and friction. Proceedings of the Institution of Mechanical Engineers, Part D: Journal of Automobile Engineering, 1999. 213(4): p. 391-402.

13. Fang, C., Meng, X., Kong, X., Zhao, B., and Huang, H., Transient tribo-dynamics analysis and friction loss evaluation of piston during cold-and warm-start of a SI engine. International Journal of Mechanical Sciences, 2017. 133: p. 767-787.

14. Jamrozik, A., Tutak, W., Kociszewski, A., and Sosnowski, M., Numerical simulation of two-stage combustion in SI engine with prechamber. Applied Mathematical Modelling, 2013. 37(5): p. 2961-2982.

15. Verma, I., Bish, E., Kuntz, M., Meeks, E., Puduppakkam, K., Naik, C., and Liang, L., CFD Modeling of Spark Ignited Gasoline Engines-Part 1: Modeling the Engine under Motored and Premixed-Charge Combustion Mode. SAE Technical Paper 2016-01-0591, 2016.

16. Zhou, D., Yang, W., An, H., and Li, J., Application of CFD-chemical kinetics approach in detecting RCCI engine knocking fuelled with biodiesel/methanol. Applied energy, 2015. 145: p. 255-264.

17. d'Adamo, A., Breda, S., Fontanesi, S., and Cantore, G., LES modelling of spark-ignition cycle-to-cycle variability on a highly downsized DISI engine. SAE International Journal of Engines, 2015. 8(5): p. 2029-2041.

18. Bohbot, J., Miche, M., Pacaud, P., and Benkenida, A., Multiscale engine simulations using a coupling of 0-d/1-dmodel with a 3-d combustion code. Oil & Gas Science and Technology-Revue de l'IFP, 2009. 64(3): p. 337-359.

19. Tabatabaie, T., Ehteram, M. A., and Hosseini, V., Investigating the effect of the heat transfer correlation on the predictability of a multi-zone combustion model of a hydrogen-fuelled spark ignition engine. Proceedings of the Institution of Mechanical Engineers, Part D: Journal of Automobile Engineering, 2016. 230(1): p. 70-81.

20. Rakopoulos, C. and Michos, C., Quasi-dimensional, multi-zone combustion modelling of turbulent entrainment and flame stretch for a spark ignition engine fuelled with hydrogen-enriched biogas. International Journal of Vehicle Design, 2009. 49(1-3): p. 3-51.

21. Bozza, F., Gimelli, A., Strazzullo, L., Torella, E., and Cascone, C., Steady-state and transient operation simulation of a "Downsized" turbocharged SI engine. SAE Technical Paper 2007-01-0381, 2007.

22. Ghojel, J., Review of the development and applications of the Wiebe function: a tribute to the contribution of Ivan Wiebe to engine research. International Journal of Engine Research, 2010. 11(4): p. 297-312.

23. Blizard, N. C. and Keck, J. C., Experimental and theoretical investigation of turbulent burning model for internal combustion engines. SAE Technical Paper 740191, 1974.

24. Tabaczynski, R. J., Trinker, F. H., and Shannon, B. A. S., Further refinement and validation of a turbulent flame propagation model for spark-ignition engines. Combustion and Flame, 1980. 39(2): p. 111-121.

25. Abu-Nada, E., Al-Hinti, I., Akash, B., and Al-Sarkhi, A., Thermodynamic analysis of spark-ignition engine using a gas mixture model for the working fluid. International journal of energy research, 2007. 31(11): p. 1031-1046.

26. Chang, J., Güralp, O., Filipi, Z., Assanis, D., Kuo, T.-W., Najt, P., and Rask, R., New heat transfer correlation for an HCCI engine derived from measurements of instantaneous surface heat flux. SAE transactions, 2004: p. 1576-1593.

27. Morel, T. and Keribar, R., A model for predicting spatially and time resolved convective heat transfer in bowl-in-piston combustion chambers. SAE Technical Paper 850204, 1985.

28. Curzon, F. and Ahlborn, B., Efficiency of a Carnot engine at maximum power output. American Journal of Physics, 1975. 43(1): p. 22-24.

29. Mozurkewich, M. and Berry, R., Finite-time thermodynamics: Engine performance improved by optimized piston motion. Proceedings of the National Academy of Sciences, 1981. 78(4): p. 1986-1988.

30. Teh, K.-Y. and Edwards, C. F. Optimizing piston velocity profile for maximum work output from an IC engine. in ASME 2006 International Mechanical Engineering Congress and Exposition. 2006. American Society of Mechanical Engineers.

31. Hoffmann, K. H., Watowich, S. J., and Berry, R. S., Optimal paths for thermodynamic systems: the ideal Diesel cycle. Journal of Applied Physics, 1985. 58(6): p. 2125-2134.

32. Chen, R., Winward, E., Stewart, P., Taylor, B., and Gladwin, D., Quasi-constant volume (QCV) spark ignition combustion. 2009, SAE Technical Paper 2009-01-0700.

33. Dorić, J. Ž. and Klinar, I. J., Efficiency characteristics of a new quasi-constant volume combustion spark ignition engine. Thermal Science, 2013. 17(1): p. 119-133.

34. Lin, J., Chang, S., and Xu, Z., Optimal motion trajectory for the four-stroke free-piston engine with irreversible Miller cycle via a Gauss pseudospectral method. Journal of Non-Equilibrium Thermodynamics, 2014. 39(3): p. 159-172.

35. Mozurkewich, M. and Berry, R. S., Optimal paths for thermodynamic systems: the ideal Otto cycle. Journal of Applied Physics, 1982. 53(1): p. 34-42.

36. Xia, S., Chen, L., and Sun, F., The optimal path of piston motion for Otto cycle with linear phenomenological heat transfer law. Science in China Series G: Physics, Mechanics and Astronomy, 2009. 52(5): p. 708-719.

37. Xia, S., Chen, L., and Sun, F., Maximum cycle work output optimization for generalized radiative law Otto cycle engines. The European Physical Journal Plus, 2016. 131(11): p. 394.

38. Chen, L., Xia, S., and Sun, F., Optimizing piston velocity profile for maximum work output from a generalized radiative law Diesel engine. Mathematical and Computer Modelling, 2011. 54(9-10): p. 2051-2063.

39. Dorić, J. Ž. and Klinar, I. J., Efficiency of a new internal combustion engine concept with variable piston motion. Thermal Science, 2014. 18(1): p. 113-127.

40. Shadloo, M. S., Poultangari, R., Abdollahzadeh Jamalabadi, M. Y., and Rashidi, M. M., A new and efficient mechanism for spark ignition engines. Energy Conversion and Management, 2015. 96: p. 418-429.

41. Verhelst, S. and Sheppard, C., Multi-zone thermodynamic modelling of spark-ignition engine combustion–an overview. Energy Conversion and management, 2009. 50(5): p. 1326-1335.

42. Heywood, J. B., Internal combustion engine fundamentals. 1988.

43. Lee, T.-K. and Filipi, Z., Improving the predictiveness of the quasi-d combustion model for spark ignition engines with flexible intake systems. International Journal of Automotive Technology, 2011. 12(1): p. 1-9.

44. Filipi, Z. S. and Assanis, D. N., The effect of the stroke-to-bore ratio on combustion, heat transfer and efficiency of a homogeneous charge spark ignition engine of given displacement. International Journal of Engine Research, 2000. 1(2): p. 191-208.

45. Assanis, D., Ekchian, J., Frank, R., and Heywood, J., A computer simulation of the turbocharged turbo compounded diesel engine system: A description of the thermodynamic and heat transfer models. 1985.

46. Poulos, S. G. and Heywood, J. B., The effect of chamber geometry on spark-ignition engine combustion. SAE transactions, 1983: p. 1106-1129.

47. Agarwal, A., Filipi, Z., Assanis, D., and Baker, D., Assessment of single-and two-zone turbulence formulations for quasi-dimensional modeling of spark-ignition engine combustion. Combustion science and technology, 1998. 136(1-6): p. 13-39.

48. Fogla, N., Bybee, M., Mirzaeian, M., Millo, F., and Wahiduzzaman, S., Development of a K-k-ϵ Phenomenological Model to Predict In-Cylinder Turbulence. SAE International Journal of Engines, 2017. 10(2): p. 562-575.

49. Han, Z. and Reitz, R. D., Turbulence modeling of internal combustion engines using RNG κ-ε models. Combustion science and technology, 1995. 106(4-6): p. 267-295.

50. Morel, T. and Mansour, N., Modeling of turbulence in internal combustion engines. 1982, SAE Technical Paper.

51. Graves, R. E. and Argrow, B. M., Bulk viscosity: past to present. Journal of Thermophysics and Heat Transfer, 1999. 13(3): p. 337-342.

52. Kim, N., Ko, I., and Min, K., Development of a zero-dimensional turbulence model for a spark ignition engine. International Journal of Engine Research, 2018: p. 1468087418760406.

53. Achuth, M. and Mehta, P. S., Predictions of tumble and turbulence in four-valve pentroof spark ignition engines. International Journal of Engine Research, 2001. 2(3): p. 209-227.

54. Livengood, J. C. and Wu, P. C., Correlation of autoignition phenomena in internal combustion engines and rapid compression machines. Symposium (International) on Combustion, 1955. 5(1): p. 347-356.

55. Ra, Y. and Reitz, R. D., A combustion model for IC engine combustion simulations with multi-component fuels. Combustion and Flame, 2011. 158(1): p. 69-90.

56. Robert, A., Richard, S., Colin, O., and Poinsot, T., LES study of deflagration to detonation mechanisms in a downsized spark ignition engine. Combustion and Flame, 2015. 162(7): p. 2788-2807.

57. Betts, J. T., Survey of numerical methods for trajectory optimization. Journal of guidance, control, and dynamics, 1998. 21(2): p. 193-207.

58. Razmara, M., Bidarvatan, M., Shahbakhti, M., and Robinett III, R., Optimal exergy-based control of internal combustion engines. Applied energy, 2016. 183: p. 1389-1403.

59. Zhu, Q., Prucka, R., Wang, S., Prucka, M., and Dourra, H., Model-based optimal combustion phasing control strategy for spark ignition engines. SAE International Journal of Engines, 2016. 9(2): p. 1170-1179.

60. Kutlar, O. A., Arslan, H., and Calik, A. T., Methods to improve efficiency of four stroke, spark ignition engines at part load. Energy Conversion and Management, 2005. 46(20): p. 3202-3220.

61. Aghaali, H. and Ångström, H.-E., A review of turbocompounding as a waste heat recovery system for internal combustion engines. Renewable and sustainable energy reviews, 2015. 49: p. 813-824.

62. Patton, K. J., Nitschke, R. G., and Heywood, J. B., Development and evaluation of a friction model for spark-ignition engines. SAE Transactions, 1989: p. 1441-1461.

63. Zweiri, Y., Whidborne, J., and Seneviratne, L., Detailed analytical model of a single-cylinder diesel engine in the crank angle domain. Proceedings of the Institution of

Mechanical Engineers, Part D: Journal of Automobile Engineering, 2001. 215(11): p. 1197-1216.

국문초록

이산화탄소 배출 감축을 위해 강화되는 차량의 연비규제나 온실가스 규제를 만족하기 위하여 많은 연구가 진행되고 있다. 미래에도 탄화수소기반 연료가 수송부분에서 많이 사용될 것으로 예측되는 상황에서, 규제를 만족하기 위해서는 내연기관 기반의 파워트레인 효율을 상승시키키는 것이 필수적이다. 여러가지 내연기관 기반 파워트레인 중에서 직렬형 하이브리드 파워트레인은 연비 측면에서 큰 장점을 가지고 있다. 이 연구에서는 직렬형 하이브리드 파워트레인 구조에서 단일 사이클내 속도 형상 조절을 통한 열역학적 효율 상승 가능성에 대해 시뮬레이션을 이용하여 논의하고자 하였다.

수치적인 방법을 통해 최적화를 수행하였기 때문에, 계산시간 측면에서 장점이 있는 준차원 스파크 점화 엔진 모델을 이용하였다. 속도형상변화 효과를 반영하기 위하여 난류 화염 모델을 이용하여 연소율을 계산하였으며, 실린더 내부 유동 기반 열전달 모델을 이용하였다. 이 때 필요한 실린더 내부 유동특성은 준차원 난류 모델을 이용하여 계산하였다. 이를 통해 속도형상변화 효과를 반영한 스파크 점화 엔진 모델을 개발하였으며, 개발한 모델을 이용하여 최적화 문제를 풀었다. 경로 최적화 문제를 이산화를 통해 파라미터 최적화 문제로 바꾸어 효율을 최대로 하는 속도 형상을 얻을 수 있었다.

사이클 해석을 수행하기 위해 3 가지 성능 지표를 이용하였다. 연소상을 비교하기 위해 유효팽창비를 정의하였다. 연소율을 가중치로 두어 연소 구간 동안 평균 부피를 구하였으며, 배기 벨브가 열리는 시점의 실린더 부피를 이용하여 무차원화 시켜 유효 팽창비를 계산하였다. 유효 팽창비가 클수록 연소가 상사점 근방에서 일어난 것을 의미하며, 연료의 화학적 에너지 전환효율이 높은 것을 의미한다. 열전달을 비교하기 위해서

흡기 벨브가 닫히는 시점부터 배기 벨브가 열리는 시점까지의 열전달량을 저위 발열량으로 무차원화 하여 비교하였다. 가스 교환 과정의 열전달은 엔진에서 얻을 수 있는 일에 영향을 주지 못하기 때문에 포함하지 않았다. 마지막으로 가스 교환 과정에서 얻을 수 있는 일은 펌핑 효율을 정의하여 비교하였다.

최적화된 속도 형상을 통해 스파크 점화 엔진의 효율을 기존 엔진에 비해 같은 평균 속도 조건에서 5% p, 최고 효율 조건에 비해 1% p 향상시킬 수 있음을 확인하였다. 사이클을 정량적으로 분석한 결과, 기존 엔진에 비해 주로 연소상 개선을 통해 효율을 향상시킬 수 있음을 확인하였다. 최적화된 속도 형상으로 운전할 때, 기존 엔진 운전 조건에서 노킹이 일어나지 않는 수준의 연소상으로 개선되었다.

속도 형상 최적화를 최근 효율을 높이기 위한 기술이 적용된 스파크 점화 엔진에 적용하였을 때, 추가적인 효율 향상을 얻을 수 있는지 살펴보았다. 기존 엔진에 비해 압축비를 높이거나, 공연비가 증가할 때, 그리고 엔진의 부하를 확장할 수 있는 가압된 조건에서 속도 형상 최적화를 수행하였다. 기존 엔진에서는 압축비를 증가시켜도 노킹으로 인해 효율이 오히려 감소하지만, 사이클내 속도 형상을 조절하면 효과적으로 노킹을 완화할 수 있어 효율이 증가하게 되었다. 이 연구에서 사용한 모델 조건에서는 압축비를 10.5 에서 13.5 까지 효율을 증가시킬 수 있음을 확인하였다. 공연비를 증가시킨 엔진 운전조건에서는 층류 화염 속도가 감소하여 기존 엔진 운전에서 충분한 효율 상승을 얻지 못하였다. 이를 속도 형상 조절을 통해 증가된 난류강도를 이용하여, 당량비가 0.7 인 조건에서 약 1.5% p 의 추가적인 효율 상승을 얻을 수 있었다. 가압된 운전 조건에서는 높아진 압력으로 인한 노킹을 완화하기 위해 점화시기를 미루어 효율이 감소하게 된다. 이는 속도 형상을 조절하여도 나타났지만, 1.6 atm

까지 가압한 조건의 효율이 기존 엔진 운전의 1.0 atm 조건의 효율 수준을 보임을 확인하였다. 따라서 가압된 조건에서도 기존 엔진의 가압되지 않은 조건의 효율 수준으로 운전할 수 있는 가능성을 확인할 수 있었다.

스파크 점화 엔진의 효율을 최대로 하는 속도 형상을 제시하였으며, 효율이 상승하는 원인 및 각 성능지표에 어느 구간의 속도 형상이 주로 영향을 주는지 분석하였다. 이를 바탕으로 모든 구간의 속도 형상을 조절할 수 없을 때, 원하는 성능 지표를 개선하기 위해서 어느 구간의 속도 형상을 변화시켜야 하는지 예측하는데 이용할 수 있을 것으로 생각된다.

주요어: 불꽃점화엔진, 준차원 모델, 속도형상조절, 경로최적화, 효율분석

학번: 2014-30343